國 立 清 華 大 學

材料科學工程研究所

博士論文

四氧化三鐵及鐵鉑-四氧化三鐵核殼結構磁性奈米微粒之合成、形狀控制、鑑定及其應用

Shape-controlled Synthesis, Characterization, and Applications of Fe_3O_4 and $FePt@Fe_3O_4$ Core-shell Magnetic Nanoparticles

指導教授：賴志煌 教授 (Prof. Chih-Huang Lai)

研 究 生：何建新 (Chien-Hsin Ho)

中 華 民 國 九 十 九 年 七 月

Abstract

This research focuses on the investigation of shaped Fe_3O_4 and FePt@Fe_3O_4 core-shell nanoparticles (NPs), especially on the shape control, core-shell structure and their potential applications. The dissertation contains three main issues, including the shape-controlled synthesis of Fe_3O_4 NPs, the shape-controlled synthesis of FePt@Fe_3O_4 core-shell NPs, and the special features and potential applications of the above two kinds of shaped NPs.

The first part describes the shape evolution, formation mechanism, and shape-induced assembly of Fe_3O_4 NPs. The hot-injection method was first used to synthesize the shaped Fe_3O_4 NPs. By injecting the Fe precursor into the hot reaction solution at 290 °C with controllable injecting rate, the monomer concentration can be easily adjusted. It was found that the final shape of Fe_3O_4 NPs was dominated by the surface energy of each plane and monomer concentration. At lower monomer concentration caused by the injecting rate of 10 mL/h, the limited monomers preferentially grow on the high energy planes. Therefore, the lowest energy {100} planes become the terminated planes resulting in cubic Fe_3O_4 NPs. Furthermore, when the injecting rate becomes 20 mL/h, the increased monomer concentration can alter the relative growth rates of {100}, {110} and {111} planes, and the rhombicuboctahedral Fe_3O_4 NPs with the main terminated planes of {100} and {110} were obtained. Both cubic and rhombicuboctahedral Fe_3O_4 NPs have similar size of 16 nm, and can be self-assembled into crystallographic orientation-ordered superlattice on TEM grids and textured-like assembly on Si substrates.

The second part of dissertation contains the shape-controlled synthesis of core-shell structured FePt@Fe_3O_4 NPs by using the hot-injecting method and seed-mediated growth. The final shape of FePt@Fe_3O_4 NPs was dominated by the growth condition of Fe_3O_4 shell. Noteworthily, our method has the advantage that the shaped cores are unnecessary to synthesize shaped core-shell NPs. Additionally, HRTEM images further verified that the epitaxial relationship between FePt core and Fe_3O_4 shell is not necessarily, which indicates the similar lattice constants between core and shell materials are not required. The above results indicated the hot-injecting method combined with seed-mediated growth has fewer requirements in synthesizing the metal core-Fe_3O_4 shell NPs. The various and desired core materials can be substituted to extend their applications.

The last part is the investigation of the special features and potential applications of shaped Fe_3O_4 and FePt@Fe_3O_4 NPs, including the cation site occupancies and MRI applications. The cation site occupancies of Fe_3O_4 NPs measured by XMCD are strongly affected by their shapes. For the cubic Fe_3O_4 NPs, more ferric ions, Fe^{3+}, occupied the octahedral sites. However, for the rhombicuboctahedral Fe_3O_4 NPs, the cation site occupancies are closer to the bulk Fe_3O_4. The cation site occupancies should be affected by the surface-to-volume ratio of NPs or by their terminated planes. These results may help to study the catalytic abilities of Fe_3O_4 NPs. Finally, we also demonstrate that superparamagnetic FePt@Fe_3O_4 nanocubes show a high r_2 relaxivity and significantly enhanced MRI contrast, which is attributable to the high magnetization of the FePt core. In addition, the self-assembly of FePt@Fe_3O_4 nanocubes may become the potential multispectral MRI agent.

摘要

本論文主要著重於四氧化三鐵和鐵鉑-四氧化三鐵核殼結構磁性奈米微粒之合成、形狀控制、鑑定、與其應用之研究。

首先，我們利用高溫注入前驅物的方法來製備四氧化三鐵的奈米微粒，注射時的反應溶液溫度為 290 °C。我們發現溶液中鐵單體的濃度會影響著四氧化三鐵奈米微粒的形狀。當前驅物注射速度只有 10 mL/h 時，所還原出的有限鐵單體將優先成長於具有較高能量的晶面，而造成具有最低能量的{100}晶面變成主要外露面，最終得到立方體形的奈米微粒。然而，當注射速度增加到 20 mL/h 時，增加的鐵單體濃度會改變各主要晶面的相對成長速率。因此原本具有第二低能量的{110}晶面，也和{100}晶面一樣變成了主要外露面之一，最後形成了削菱截角立方體(Rhombicuboctahedron)。在我們的實驗中，這兩種四氧化三鐵奈米微粒的粒徑大約都在 16 奈米左右，並且都可以在 TEM 銅網上和矽基板上自組裝成具有優選晶體方向的奈米微粒超晶格結構。

第二部分的研究主要是製備具由核殼結構的鐵鉑-四氧化三鐵奈米立方體。我們利用上述之高溫注入前驅物的方法搭配晶種成長法，來製備具有球形鐵鉑核和立方體形四氧化三鐵殼的複合式磁性奈米

微粒。此複合式奈米微粒的最終形狀主要取決於四氧化三鐵殼的成長條件。並且經由 HRTEM 的分析可得知，鐵鉑核和四氧化三鐵殼並不需具備磊晶成長關係，此結果表示內核的材料並不需要具備與外殼四氧化三鐵相近之晶體常數。因此，不同材料的核可被選用來製備具有核殼結構的四氧化三鐵奈米立方體，以增進其應用價值。

最後一部分則是探討四氧化三鐵和鐵鉑-四氧化三鐵奈米立方體的特性和前瞻應用。我們利用 XMCD 來量測鐵離子在四氧化三鐵內不同位置的分佈情形。在立方體形的四氧化三鐵奈米微粒內，我們發現三價鐵離子佔有八面體位置的比率比一般四氧化三鐵塊材還來的高。然而，在削菱截角立方體形的四氧化三鐵奈米微粒內，其鐵離子在不同位置上的分佈情形就比較接近於四氧化三鐵塊材。此鐵離子分佈位置的不同可能是由於這兩種形狀的奈米微粒具有不同的比表面積和外露面所致，此結果也將有助於進一步研究四氧化三鐵的催化特性。最後，我們也發現鐵鉑-四氧化三鐵奈米微粒能顯著地增強 MRI 影像對比，並且效果優於目前市售之影像顯影劑，此顯著效果應歸因於鐵鉑核的高單位磁化量。另外具有自組裝排列的鐵鉑-四氧化三鐵奈米立方體有機會成為前瞻性多頻譜的影像增強劑。

誌謝

能完成博士論文與學業，首先要感謝指導教授賴志煌老師的指導與督促，不論是在科學研究上的啟蒙與訓練，或是待人處事上的態度，都帶給我寶貴的經驗，讓我受益良多。此外也感謝金重勳教授、周立人教授、劉如熹教授和和陳三元教授撥冗出席參加我的學位口試，並且提出許多寶貴的意見與指導。

實驗室的點點滴滴一直是我的博士班生涯的重心，感激曾經出現在實驗室的所有人，給予我生活上的關懷和幫助。尤其是賴志煌老師，除了嚴謹地指導學生的研究之外，也同時悉心照顧學生的生活。另外，謝謝師母一直以來的關心。感謝泳泓、威全、郁仁、朝成、震麟、允中、若帆、柏翔、夢嫻和勝煌等學長姐所給我的指導與鼓勵。謝謝智斌和文傑兩位博後為實驗室所帶來的新活力。另外還有同窗肇謙，你總是在我忙碌疲憊時，適時提供我精神上的關懷以及實質上的休憩場所。另外鑫泓、彥鈞、皓程、家庠、致喨、良瑋、武璋、容蔚、姵禎、加琪、國峰、鼎碩、偉志、聖傑等學弟妹，謝謝你們在實驗上的幫忙，以及你們的研究成果也帶給我不少的啟發。比較年輕的伊芸、崧富、建瑋、奕璋、如正、志宇、家豪、鼎翔學弟妹們，你們總是帶給實驗室許多的歡笑。在實驗室裡，要特別感謝兩個人。謝謝智斌學長在論

文和 paper 上指導，使其能夠更加完善，也讓我的研究眼界更加開闊。也謝謝加琪學妹在實驗上和生活瑣碎上的幫忙，並且總是能在關鍵時刻為我帶來好運。

另外，感謝工科系陳福榮老師團隊在 TEM tomography 上所給的幫忙、中興大學物理系藍明德老師團隊在 SQUID 量測上的協助、中研院生醫所張程老師團隊所提供的 MRI 分析指導、同步輻射中心林宏基博士在 XMCD 上的指導和中興大學的趙佩琪小姐在 TEM 量測上所給予的幫忙與協助。

最重要的，感謝一路陪我走過的家人，尤其是我的母親，謝謝您無私地奉獻和諒解，也謝謝我的姊姊和弟弟，因為有你們的善解人意和體貼，得以讓我無後顧之憂地在外求學。最後，謝謝一路陪伴在我身旁的淑雅，謝謝妳所給我的體諒和包容，以及共享我們所有的憂傷與歡樂。

CONTENTS

LIST OF TABLES

LIST OF FIGURES

Chapter I

Introduction

The unique and novel properties of nanomaterials have initiated the development of nano-science and nano-technology. In the field of magnetism, the finite size effect and surface effect strongly dominate the magnetic properties of nanomaterials.[1] The finite size effect makes the magnetic domain structure of nanomaterials transfer from multi-domain to single-domain as the size reduces. The superparamagnetism (SPM), which means the thermal energy can easily flip the magnetization of magnetic nanomaterials, is also caused by the finite size effect.[2] On the other hand, the surface atoms become considerable due to the high surface-to-volume ratio of nanomaterials. Comparing to the inner atoms, surface atoms usually demonstrate particular behavior and properties due to the broken symmetry of crystal structure. The surface effects, such as canting spins and magnetically dead layers, play important roles in designing the magnetic nanomaterials.

Many efforts have been made not only to investigate the particular properties of magnetic nanomaterials in fundamental studies but to tailor these properties for practical applications, especially for biomedical and magnetic recording applications. Tailoring the properties of nanomaterials by adjusting their size and composition has been widely investigated.[3-8] Furthermore, controlling the shape and interface structure of

nanomaterials can also manipulate their properties. However, preparing nanomaterials with specific morphology and structure is still an important and challenging issue. Hence, the shape control, formation mechanism, and potential applications of magnetic nanomaterials are investigated in this dissertation.

1.1 Motivation

Fe_3O_4 (magnetite), which occurs abundantly in nature and is an important ore of iron, is the most prominent and well-known magnetic iron oxide. In addition to mining form mineral, single-crystalline Fe_3O_4 NPs have also been found from the magnetosome in magnetotactic bacteria and from the honeybees through biomineralization.[9-11] Due to the inherent biocompatibility and low toxicity,[12-14] the applications of Fe_3O_4 NPs in biomedicine, such as MRI contrast agent, hyperthermia, drug delivery, and magnetic separation, have been widely investigated.[12-14] Noteworthily, most of Fe_3O_4 NPs found in magnetotactic bacteria are cubic or cuboctahedral with a narrow size distribution.[10] The artificial Fe_3O_4 nanocubes are successfully synthesized until 2007 by tuning the surfactant system.[15-17] However, the formation mechanism, shape control, and even a new facile method for the synthesis of shaped Fe_3O_4 NPs still need to be further investigated.

The FePt NP is another attractive magnetic material. The ordered $L1_0$ FePt possesses high magneto-crystalline anisotropy and has been demonstrated as the most promising material for ultrahigh-density magnetic recording media.[18] On the other hand, in the recent biomedical

applications, disordered fcc-phase FePt NPs exhibit their superiority due to their high saturation magnetization (M_S) and good chemical stability.[19-20] It was also reported that the uncoated FePt NPs had no significant toxicity on bEnd3 cells during 24 hours incubation.[21] Integrating FePt cores into Fe_3O_4 nanocubes can combine good bio-compatibility with relatively high M_S. FePt-Fe_3O_4 heterogeneous dimers were investigated for the application of the permanent magnet with high energy product due to their large coercivity and high M_S after reductive annealing.[22-23] Recently, FePt-Fe_3O_4 dimers were also demonstrated for MRI applications.[24-25] However, the preparation and MRI application of shaped FePt-Fe_3O_4 dimers, e.g. FePt@Fe_3O_4 nanocubes, has not been reported.

The uniform and shaped NPs can potentially behave as good building blocks to be self-assembled into ordered superstructures, which can perform specific functionalities in biological systems or become an attractive candidate for ultrahigh-density magnetic pattern media.[18, 26] The synthesis and self-assembled long-range superstructures of spherical Fe_3O_4 NPs have been investigated.[27] However, the formation of crystallographic-oriented superlattices has still been a difficult task and has only been reported in the assembly of shaped NPs, such as MnO octahedrons, γ-Fe_2O_3 nanocubes, and Fe_3O_4 octahedrons.[28-30] Hence the shape-dependent textured assembly of shaped Fe_3O_4 and FePt@Fe_3O_4 NPs on TEM grid and on Si substrates is investigated. On the other hand, Fe_3O_4 has been employed as a catalyst for the removal of heavy metals in rinsing wastewater, such as As(III), As(V), Gd(II), Cr(VI), and Cu(II).[31-32] The catalytic ability of Fe_3O_4 is typically related to the presence of both

ferrous (Fe^{2+}) and ferric (Fe^{3+}) ions.[33] However, the shape-dependent cation site occupancies of shaped Fe_3O_4 NPs have not been reported.

The goals of this study are as follows: (1) Developing a facile method and investigating the formation mechanism for the synthesis of shaped Fe_3O_4 and FePt@Fe_3O_4 NPs. (2) Investigating the shape-induced self-assembly of shaped Fe_3O_4 NPs. (3) Characterizing the unique properties and exploring the potential applications of shaped Fe_3O_4 and FePt@Fe_3O_4 NPs.

1.2 Outline of the dissertation

The main part of this dissertation is the investigation of the formation mechanism, shape control, and potential application of shaped Fe_3O_4 and FePt@Fe_3O_4 NPs. Chapter 2 presents the background of the synthesis, properties, and applications of magnetic NPs. The synthesis method and analyzing techniques are presented in Chapter 3. The formation mechanism and shape control of shaped Fe_3O_4 NPs were discussed in Chapter 4. Furthermore, the synthesis of shaped FePt@Fe_3O_4 NPs is discussed in Chapter 5. The cation site occupanies, and the MRI application of shaped Fe_3O_4 and FePt@Fe_3O_4 NPs are discussed in Chapter 6. The dissertation is summarized in Chapter 7.

Chapter II

Background

2.1 Introduction

Magnetic nanoparticles (NPs) are of great interest for researchers from a wide range of disciplines, including magnetic fluids, catalysis, biomedicine, magnetic resonance imaging, and data storage.[12-13, 34-39] The reduced size of magnetic materials leads to special properties comparing with their counterpart bulk materials. For example, when the size of magnetic NPs was below a critical value, the magnetic domain changes from multi-domain to single-domain and even shows the superparamagnetic behavior at room temperature. In addition, the surface effect also becomes considerable and leads to particular phenomena, such as the magnetically dead layer on the particle's surface, the surface canted spins, or the spin-glass like behavior. These special features caused by the finite-size effect and the surface effect make magnetic NPs very attractive for fundamental studies and potential applications. Among these magnetic NPs, FePt and Fe_3O_4 are extensively highlighted. FePt is one of the promising candidates for future ultrahigh-density magnetic recording due to its large magnetocrystalline anisotropy ($K_u = 7 \times 10^6$ Jm^{-3})[40], while Fe_3O_4 NPs are widely investigated in biomedical applications due to their biocompatible properties and low toxicity. Hence the preparations of magnetic FePt and Fe_3O_4 NPs have been widely investigated. Various

chemical synthesis methods, such as co-precipitation, thermal decomposition, micelle synthesis, and hydrothermal synthesis, have been developed.[1] Although the size and composition effects on the properties of magnetic NPs were extensively studied, the shape effects and core/shell effects still attract much attention and investigation. However, limited reports on the shape control of magnetic NPs were reported. Therefore, the general strategies applied for controlling the NP shape are reviewed from the synthesis of metal and semiconductor NPs. Finally, the applications of magnetic NPs are reviewed.

2.2 The special features of magnetic nanoparticles

The properties of magnetic NPs are dominated by both finite-size effects and surface effects.[1] Generally, finite-size effects result from the quantum confinement of electrons, whereas the surface effects are related to the symmetry breaking of the crystal structure at surface. The special features of magnetic NPs resulting from these two effects include the transition from magnetic multi-domain to single-domain, superparamagnetic behavior,[1, 4] surface canting spins,[2] and surface magnetically dead layers.[1] The origins of these special features are reviewed and discussed in this section.

2.2.1 Finite size effects

The two most studied finite-size effects in magnetic NPs are the transition from multi-domains to single domain and superparamagnetic behavior. The formation of multi-domains or single domain was determined by the competition between the magnetostatic energy and the domain wall energy, shown in Fig. 2.1. The increase of magnetostatic energy is proportional to the volume of magnetic materials, while the increase of magnetic domain wall energy is proportional to the interfacial area between magnetic domains. Larger magnetic particles tend to form the magnetic multi-domains structure due to the significant reduction in magnetostatic energy even though to form domain wall in the crystal adds energy. However, if the size reduces below a critical value, the reduction in magnetostatic energy becomes smaller. Thus, the smaller particles prefer to remain in the single domain state. The critical diameter to reach

the single domain limit is determined by the exchange energy and saturated magnetization. For spherical NPs, the critical diameter (D_C) can be expressed as follows: [41]

$$D_C = \frac{17\gamma}{\pi^2 M_S^{\ 2}} \tag{2.1}$$

where the γ is the domain wall energy. Because $\gamma = 2\,K\,\delta$, γ is related to the crystal anisotropic constant K and domain wall thickness δ. M_S is the saturation magnetization. From Eq. (2.1), the large domain wall energy and low saturation magnetization leads to the increase of critical diameter of the single domain limit. Typical values of D_C for some important magnetic materials are listed in Table 2.1.[1]

In addition, the coercivity of magnetic particles also depends on the size and magnetic domain state, shown in Fig. 2.2.[42] In multi-domain magnetic materials, the magnetization reversal can be achieved by domain wall motion and by spin rotation. While in single-domain materials, the magnetization can be reversed only by spin rotation. Hence, the coercivity of magnetic NPs increases as the domain structure of magnetic particle is changed from multi-domain to single domain. However, if the particle size was further decreased, the thermal fluctuation disturbs the stability of magnetic moment, resulting in the decrease of coercivity. Finally, the coercivity disappears, and the magnetic particles show superparamagnetic behavior.

Material	D_c [nm]
hcp Co	15
fcc Co	7
Fe	15
Ni	55
$SmCo_5$	750
Fe_3O_4	128

Table 2.1 Estimated single-domain size for different spherical particles.[1]

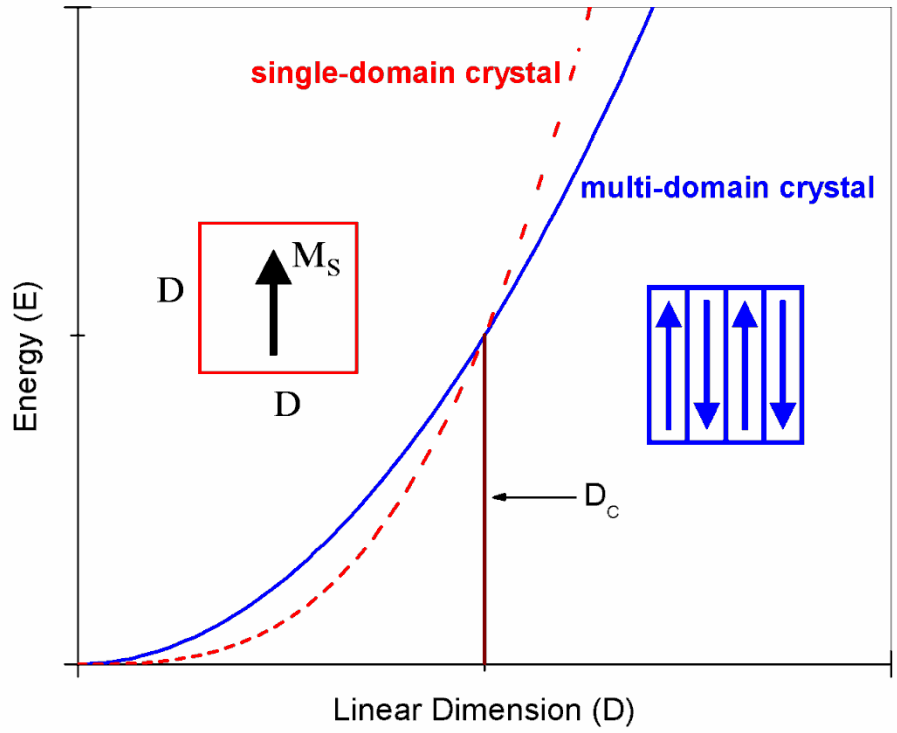

Fig. 2.1 Relationship between the energy E of a crystal and its linear dimension L for two kinds of magnetic state.[41]

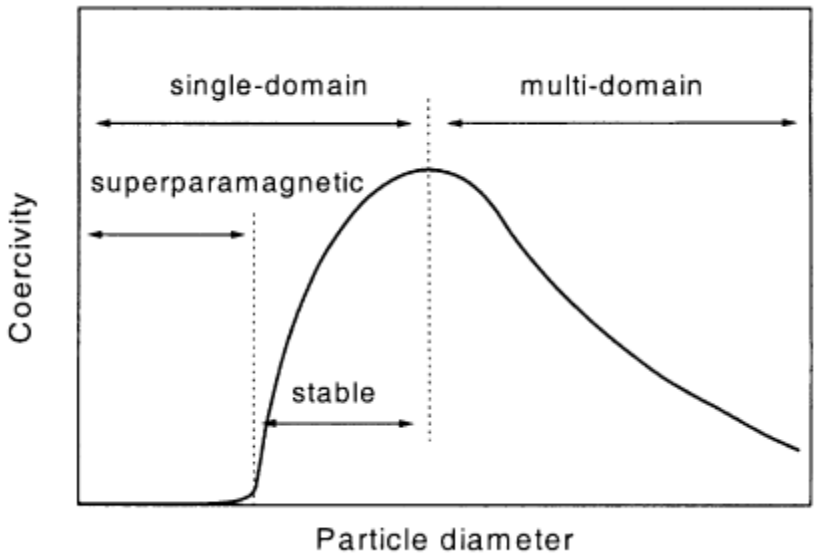

Fig. 2.2 Size dependence of coercivity.[42]

The superparamagnetism means the thermal energy can easily flip the magnetization of magnetic nanomaterials due to the reduced size.[2] The magnetic anisotropy energy responsible for holding the magnetic moments along a certain direction can be expressed as follows:

$$E_A = K_u V, \tag{2.2}$$

where the K_u is the anisotropy constant and V is the particle volume. When the size decreases, the anisotropy energy $K_u V$ reduces; therefore the magnetization becomes easily be flipped by thermal energy. The relaxation time of the moment of particle (τ) is given by the Neel-Brown expression as follows:[4]

$$\tau = \tau_0 \exp\left(\frac{K_u V}{k_B T}\right) \tag{2.3}$$

where k_B is the Boltzmann's constant and τ_0, the frequency factor, is about 10^{-9} s. The ratio of $K_u V/k_B T$ is so-called thermal stability factor. When the $K_u V/k_B T$ is equal to 25, the magnetic moment can be flipped within 100 s. Hence, $K_u V/k_B T = 25$ was generally considered as the criterion to define

the superparamagnetic limit.[41]

According to the definition of superparamagnetic limit, the blocking temperature (T_B), below which the magnetization of magnetic NPs becomes stable, can be expressed as $T_B = K_uV/25k_B$.[41] The blocking temperature depends on the anisotropy constant, the size of the particles, and the experimental measuring time.[1] A simple and rapid way to estimate the blocking temperature is measuring the zero-field-cooled (ZFC) and field-cooled (FC) magnetization-temperature (M-T) curves. Typically, the sample is cooled with or without a magnetic field, and then the magnetization of sample is measured on warming with a small external magnetic field of 100 Oe. As the temperature increases, the "frozen" moments acquire the thermal energy to be aligned with the external field. The aligned moments reaches a maximum at T_B. Above T_B, the excess thermal energy randomizes the aligned magnetic moment leading to the decrease in magnetization.

2.2.2 Surface effects

As the material size decreases, the ratio of surface atoms to bulk atoms increases. It implies that the surface and interface effects become more important. The origin of surface effects is due to the symmetry breaking of crystal structure. For magnetic metals, such as Fe, Co, Ni, the magnetism origins from the spin and orbital motion of the unpaired 3d electrons. For example, Fe atom has 4 unpaired electrons resulting in 4 Bohr magnetons (μ_B). Due to the hybrid of 3d orbital and 4s orbital, the real number of Bohr magneton of Fe is reduced to 2.2 μ_B. However, because there are less neighboring atoms at surface, the hybrid is reduced

leading to more Bohr magnetons. Therefore, when the size of metallic Fe, Co, and Ni reduces, the magnetic moments increase.[2] On the contrary, the ion compounds show the reduced magnetization as the size is reduced. This is because the incomplete coordinated ions at the surface lead to a disordered spin configuration near the surface. For example, spin canting in ball-milled $NiFe_2O_4$ and chemically precipitated γ-Fe_2O_3 particles has been demonstrated via Mössbauer spectroscopy, as a mechanism for moment reduction.[41] Canting spins, which may result from the broken balance between the competing antiferromagnetic interactions on the surface of ferrite NPs, are very difficult to be aligned even applying a large magnetic field. Furthermore, the broken symmetry on the surface makes the antiferromagnetic nanomaterials have net magnetic moments. For example, the NiO bulk materials have two groups of magnetic moments with identical magnitude but in antiparallel directions. No net magnetic moment is detected in bulk NiO materials due to it antiferromagnetism. However, the small NiO NPs are predicted to have a net magnetic moment.[2] The surface magnetic spins of antiferromagnetic NPs are not perfectly anti-parallel aligned with the inner magnetic spins due to the breaking symmetry. Hence the uncompensated surface spins result in small net magnetic moment.[2] It has been simulated that the spin configuration of small NiO NPs of 2.5 nm has 8 sublattices, shown in Fig. 2.3.[2]

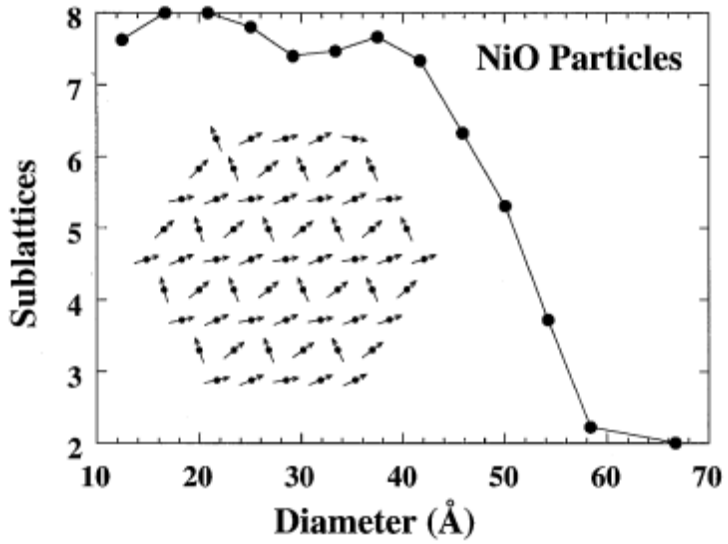

Fig. 2.3 Calculated average number of sublattices for 30 different NiO particles in zero applied field as a function of diameter. The inset shows a cross section of a representative 25 Å particle, having an 8-sublattice state.[2]

The surface anisotropy is the other important surface effect of magnetic NPs. In a very simple approximation, the total anisotropy energy of a spherical particle with diameter D, surface area S, and volume V can be described by one contribution from the bulk and another from the surface:

$$K_{eff} = K_V + \frac{6}{D} K_S ,^{1} \qquad (2.4)$$

where K_V and K_S are the bulk and surface anisotropy energy constants, respectively. The surface anisotropy, K_S, is assumed to be normal to the particle surface and independent to the particle size. When the particle size decreases, the effect anisotropy constant, K_{eff}, is enhanced. The surface anisotropy is of order of 1-10 mJ/m^2, several orders of magnitude greater than that of bulk magnetocrystalline anisotropy which is about 0.01-1 mJm^{-2} in cubic ferromagnets. Labaye *et al.* have used Monte Carlo to simulate the spin configuration of ferromagnetic NPs and found that

the K_S/K_V ratio and particle size dominated the spin configuration. When the bulk anisotropy, K_V, is significantly smaller than surface anisotropy, K_S, the spin configuration becomes radically orientated outward to the surface, shown in Fig. 2.4.[43]

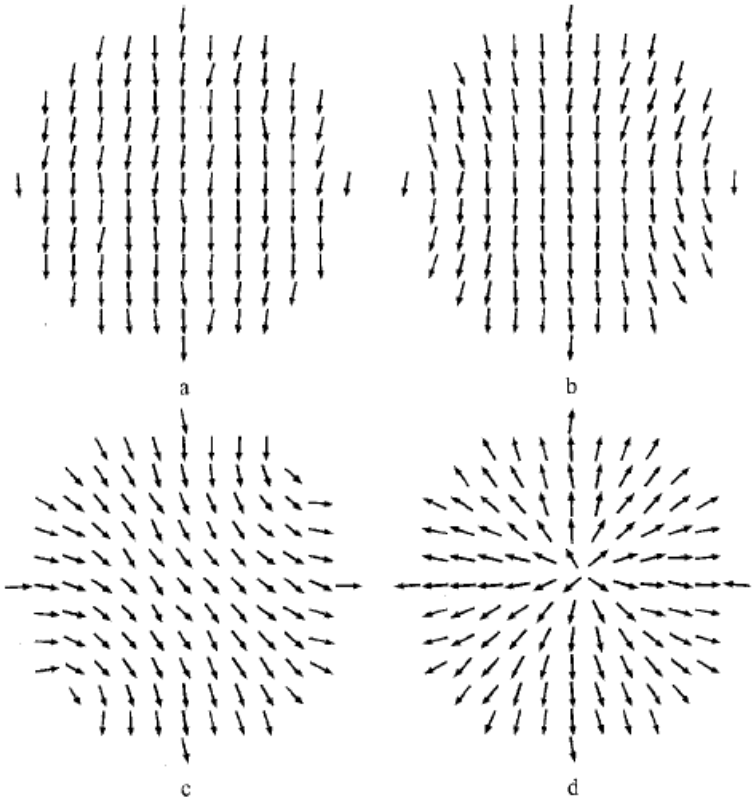

Fig. 2.4 The central plane of nanosphere for K_S/K_V =1 (a), 10 (b), 40(c), and 60 (d). The *Oz* axis is vertical.[43]

2.3 The synthesis and characteristics of magnetic nanoparticles

Because of the above interesting and special properties, magnetic NPs have been extensively synthesized and studied. Many magnetic NPs, including pure metals, alloys, and oxides have been synthesized in various size, composition, phases, and shapes. Especially during the past years, the shape control and heterogeneous structure have been specially focused. In this section, the synthesis and characteristic of magnetic NPs are reviewed.

Although various synthesis methods, such as co-precipitation, micelle, laser pyrolysis, and hydrothermal synthesis, have been used to prepare the magnetic NPs, the thermal decomposition techniques were most used due to the easy preparation of high crystalline NPs. The size and shape control can easily be achieved by using thermal decomposition techniques.[15, 17, 44] Among magnetic NPs, Fe_3O_4 and FePt were extensively highlighted due to their properties and applications. Hence the synthesis and characteristic of Fe_3O_4 and FePt NPs are discussed here.

2.3.1 The synthesis and characteristics of magnetite (Fe_3O_4) nanoparticles

The introduction of magnetite (Fe_3O_4)

Magnetite, which is also named **ferrous-ferric oxide**, is the most prominent and the best-known ferrimagnetic material with the chemical formula of **Fe_3O_4** and with the chemical IUPAC name of **iron(II, III) oxide**. Its chemical formula is also written as **$FeO{\cdot}Fe_2O_3$** indicating the

different oxidation sates of iron in one structure. The room temperature structure of magnetite is the cubic inverse spinel structure with the space group of ***Fd3m***, shown in Fig. 2.5. In spinels, the oxygen anions form a face-centered cubic (fcc) close-packed frame, in which the cations occupy either tetrahedral sites (A site) or octahedral sites (B site). Magnetite can be described by the formula $Fe^{3+}{}_A(Fe^{2+}Fe^{3+})_BO_4$ indicating that tetrahedral sites were occupied by Fe^{3+}, while octahedral sites were occupied by equal numbers of Fe^{2+} and Fe^{3+}. The lattice parameter of spinel structure and formula weight of magnetite at room temperature are 8.396 Å and 231.54 grams/mole, respectively, leading to the specific gravity of 5.18 g/cm.[3] Magnetite has been known and utilized for several centuries as the lodestone. For the recent decades, magnetite attracted even more attention and investigation due to its unique fundamental properties and extensive applications.

Fe_3O_4 is a ferrimagnetic material with a high Curie temperature of 850K. Ferrimagnetism means that there are two uncompensated magnetic sub-lattices resulting in net magnetic moment. The spin configuration of Fe_3O_4 can be written as $(Fe^{3+}\downarrow)_A(Fe^{2+}\uparrow Fe^{3+}\uparrow)_BO_4$. The anti-parallel Fe^{3+} spins on A and B sites cancel out, and the net magnetic moment is only contributed by Fe^{2+} spins. Therefore, the net moment per unit cell is 4 μ_B resulting in the saturation magnetization of 92 emu/g for bulk Fe_3O_4.

The electric properties of Fe_3O_4 have been of great interest in the field of spintronics. According to band theory, Fe_3O_4 is a half-metal material above the Verwey transition temperature (T_V ~ 120 K). Its minority-spin electrons are conducting, whereas the majority-spin electrons are

insulating. Rapid hoping of electron between Fe^{2+} and Fe^{3+} on the B site leads to a good conductivity of 250 $\Omega^{-1}cm^{-1}$ at room temperature. Because electrons with single spin orientation (spin up or spin down) are conducting, it leads to perfect spin polarization. Therefore, Fe_3O_4 becomes one of the potential materials applied for spintronic device, such as magnetic tunnel junction (MTJ).

Verwey transition is one of important phenomena of Fe_3O_4, including the changes of structure and electric properties. Around 124 K, Fe_3O_4 undergoes a first-order phase transition, which is related to the ordering of Fe^{2+} and Fe^{3+} ions on the octahedral sites. The ordering causes the inhibition of electron hopping between Fe^{2+} and Fe^{3+} ions on the octahedral sites resulting to the dramatic decrease of electric conductivity about two orders of magnitudes. In addition, the original cubic structure with the space group of ***Fd3m*** transforms into a monoclinic structure with the space group of ***Cc*** when the temperature is below the Verwey transition temperature (T_V). It was reported that the lattice parameters at 10 K are a = 11.868 Å, b = 11.851 Å, c = 16.752 Å, and β = 90.20°.[45] Verwey transition also causes the change in the magnetic anisotropy of Fe_3O_4.[46] Bulk Fe_3O_4 has cubic magnetic anisotropy with the <111> and <100> directions as the easy and hard axes of magnetization, respectively. The first-order magnetocrystalline anisotropy constant (K_1) at room temperature has a negative value of $-1.35*10^5$ erg/cm^3 which changes sign at low temperature.[47] The structure change also leads to a change of cubic anisotropy to uniaxial anisotropy with <001> easy axis.[48]

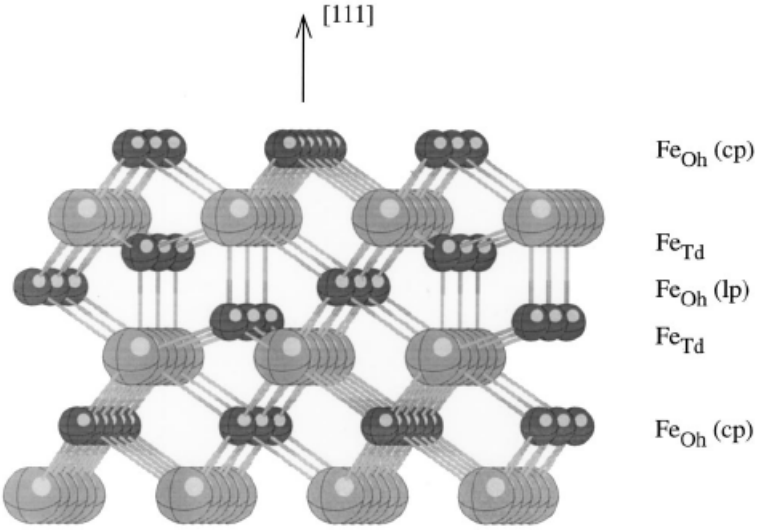

Fig. 2.5 Schematic diagram of the Fe_3O_4 lattice of spinel structure. The small black balls present the Fe ions, while the larger gray balls present the O ion. Successive Fe ion layers exist along the [111] direction. There are three basic types of Fe ion layers, including closed-packed octahedral (Fe_{Oh}, cp), tetrahedral (Fe_{Td}), and loose-packed octahedral (Fe_{Oh}, lp).[49]

The synthesis of Fe_3O_4 nanoparticles

Fe_3O_4 particles were early and commonly synthesized by using coprecipitation of ferrous (Fe^{2+}) and ferric (Fe^{3+}) ions in the basic aqueous solutions, such as NaOH or NH_4OH.[50] Even though the coprecipitation method is advantageous to have the mass production of Fe_3O_4 NPs, the size and shape are difficult to control. Smaller (<20 nm) and monodisperse Fe_3O_4 NPs has only limited success. On the other hand, the pH value of the reaction mixture needs be precisely adjusted during the synthesis and purification, which also increases difficulties in the coprecipitation method.

Organic solution-phase decomposition of the iron precursor at high temperature has been widely used to synthesize the iron oxide NPs. The approach to synthesize Fe_3O_4 NPs with the size below 20 nm was developed by Sun and Zeng.[51] They used thermal decomposition of iron

(III) acetylacetonate, $Fe(acac)_3$, in the presence of oleic acid and oleylamine to produce monodisperse Fe_3O_4 NPs. In their experiments, the size of Fe_3O_4 NPs can be adjusted from 4 to 20 nm by seed-mediated growth. The synthesis approach is shown in Scheme 2.1.[52] The TEM images are shown in Fig. 2.6. Fig. 2.7 shows the hysteresis loops of 16 nm Fe_3O_4 NPs synthesized by the thermal decomposition method.[52] The particles are ferromagnetic at 10 K with coercivity of 450 Oe, while those are superparamagnetic at 300 K. The thermal decomposition can be further extended to synthesize the monodisperse MFe_2O_4 (M = Fe, Co, Mn) NPs.[52] Particle diameter can be tuned from 3 to 20 nm by adjusting reaction conditions or by seed-mediated growth. Even the as-synthesized MFe_2O_4 NPs are hydrophobic; they can be transformed into hydrophilic by mixing with bipolar surfactants. On the other hand, there are still many efforts in controlling the shape of magnetic NPs. This part is discussed in section 2.4.

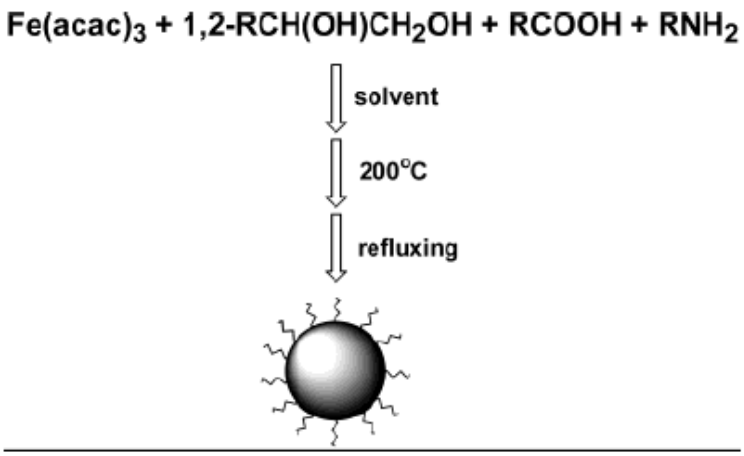

Scheme 2.1 The illustration of forming Fe_3O_4 NPs.[52]

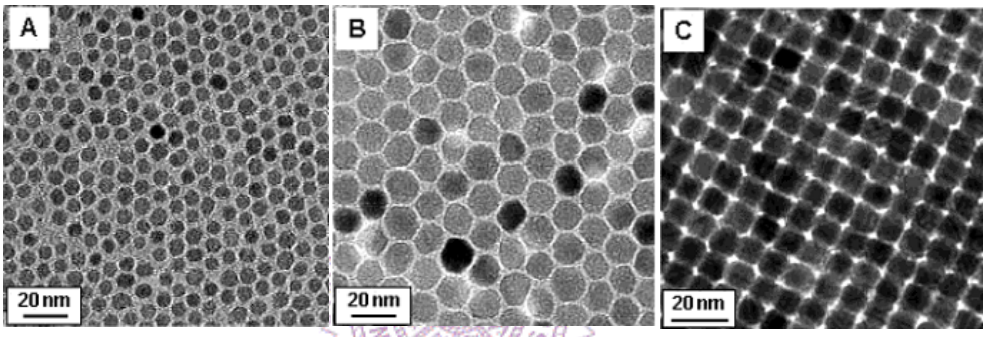

Fig. 2.6 TEM images of (A) 6 nm and (B) 12 nm Fe_3O_4 NPs. (C) 3D superlattice of 10 nm Fe_3O_4 NPs.[52]

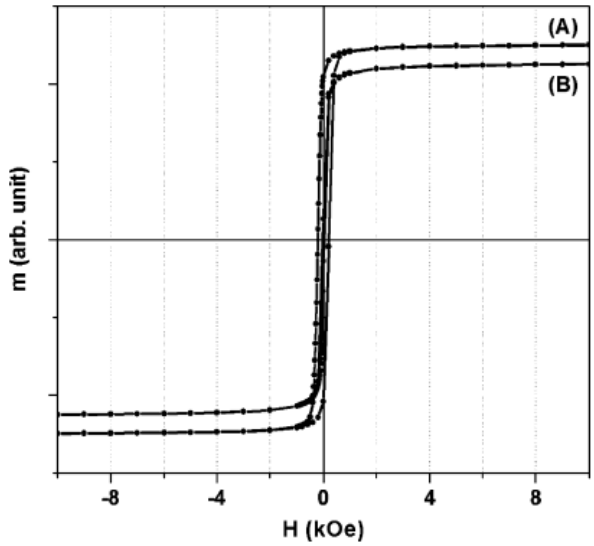

Fig. 2.7 Hystersis loops of the 16 nm Fe_3O_4 NPs assembly measured at (A) 10 K and (B) 300 K.[52]

2.3.2 The synthesis and characteristics of FePt nanoparticles

The introduction of FePt

FePt is the other important magnetic material due to its large magnetocrystal anisotropy to overcome the thermal fluctuation. From the phase diagram, shown in Fig. 2.8, the FePt has four main phases, including the disordered γ phase, ordered γ_1, γ_2, and γ_3 phases. The disordered γ phase is thermally unstable at room temperature. However, the transformation from disordered phase to ordered phase requires high temperature annealing. These three ordered phases are different in composition and in magnetic properties. In general, γ_1-Fe_3Pt phase ($L1_2$, ***Pm*** $\bar{3}$ ***m***, cubic, 15 at% < Pt < 30 at%) is paramagnetic, γ_2-FePt phase ($L1_0$, ***P4/mmm***, tetragonal, 30 at% < Pt < 55 at%) is ferromagnetic, and γ_3-$FePt_3$ phase ($L1_2$, ***Pm*** $\bar{3}$ ***m***, cubic, 60 at% < Pt < 80 at%) is antiferromagnetic. Because the equal-atomic γ_2-FePt phase has large magnetocrystal anisotropy which can overcome the superparamagnetism, many efforts were made in synthesizing equal-atomic ordered FePt NPs. Chemically disordered FePt contains equal-atomic percentage of Fe and Pt atoms randomly locating at the sites of the face-centered cubic (fcc) frame with the lattice constant of 3.816 Å, while the chemically ordered FePt is in $L1_0$ phase with alternating atomic layers of Fe and Pt stacked along the [001] direction, shown in Fig. 2.9. The FePt $L1_0$ phase has a face-centered tetragonal ***(P4/mmm***, fct) structure with a reduced c-axis of 3.713 Å and an expanded a- and b- axis of 3.582 Å.

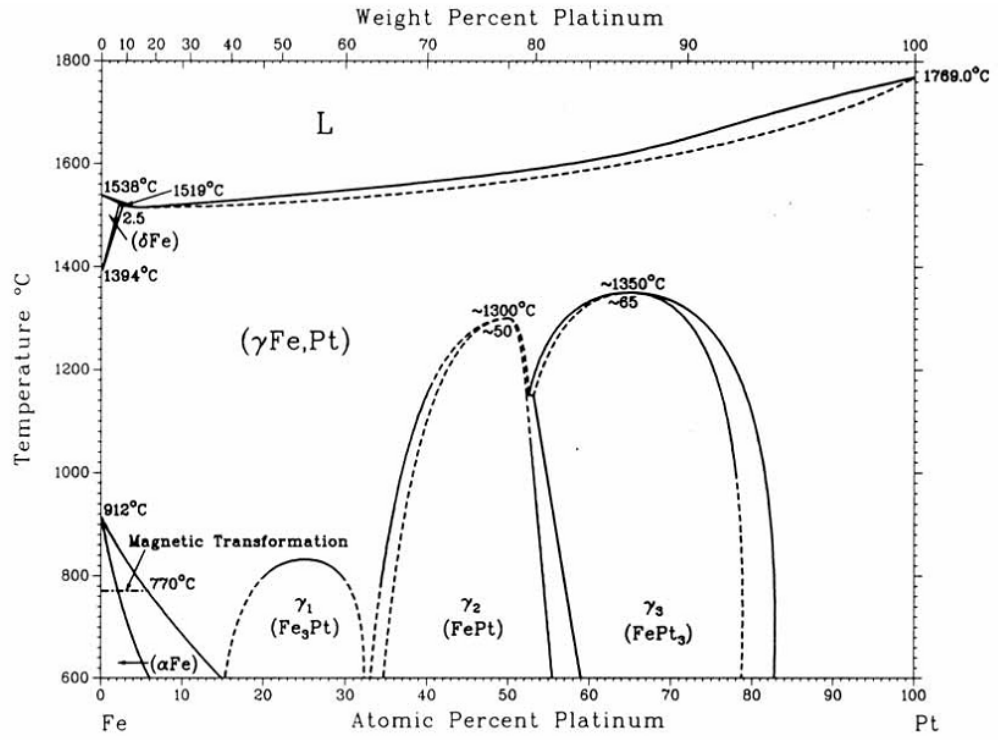

Fig. 2.8 The phase diagram of Fe-Pt (Data are from Thaddeus B. Massalski *et al.*, Binary alloy phase diagram, Materials Park, Ohio/ASM International, 1990)

As mentioned above, the disordered fcc FePt is magnetically soft and has a small coercivity. After annealing at high temperature, the disordered phase is transferred to ordered $L1_0$ phase. The large magnetocrystal anisotropy makes ordered FePt possess a giant coercivity and a uniaxial hard axis along the [001] direction. The saturation magnetization of bulk ordered FePt alloy is 1140 emu/cc, which is lower than that of bulk Fe of 1700 emu/cc and higher than that of Fe_3O_4 of 471 emu/cc. The anisotropy constant, K, is about 10^7 Jm^{-3}.[40] The large anisotropy constant is due to the Fe and Pt interactions resulting from spin-orbit coupling and the hybridization between Fe 3d and Pt 5d states.[40] The Fe-Pt interactions also render FePt become chemically more stable. Hence, the high magnetic moments, larger coercivity, and chemical stability make FePt become potential candidate for the high density magnetic recording

media.

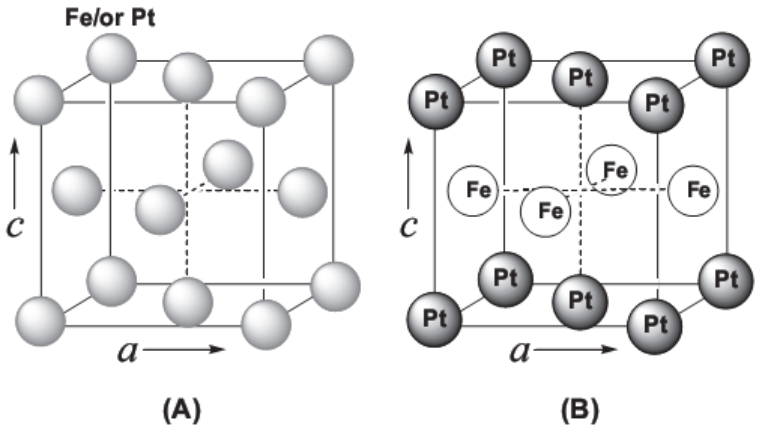

Fig. 2.9 Schematic illustration of the unit cell of (A) chemically disordered fcc and (B) chemically ordered fct FePt.[37]

The synthesis of FePt nanoparticles

The synthesis of FePt NPs was first achieved by Sun *et al.* in 2000.[18] Simultaneous thermal decomposition of iron pentacarbonyl, $Fe(CO)_5$, and reduction of platinum acetylacetonate, $Pt(acac)_2$, were used to synthesize monodisperse FePt NPs, shown in Fig. 2.10. The as-synthesized FePt NPs are disordered and have the size smaller than 10 nm, show in Fig. 2.11. The composition of FePt can be varied by adjusting the precursor ratio of $Fe(CO)_5/Pt(acac)_2$. The more Fe precursor leads to high percentage of Fe in FePt NPs. The size can be adjusted by controlling the surfactant to precursor ratio and by seed-mediated method. The ratio of surfactant to precursor requires at least 8:1 to make the size of FePt NPs larger than 6 nm. After annealing at high temperature, the disordered fcc FePt NPs are transferred to ordered $L1_0$ FePt NPs. The coercivity of annealed FePt NPs depends on the annealing temperature and their composition, shown in Fig. 2.12.

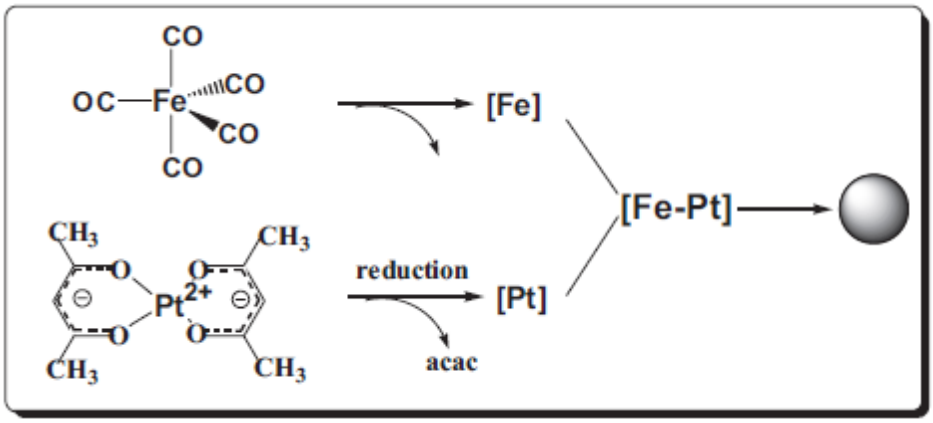

Fig. 2.10 Schematic illustration of FePt NP formation from the decomposition of $Fe(CO)_5$ and reduction of $Pt(acac)_2$.[37]

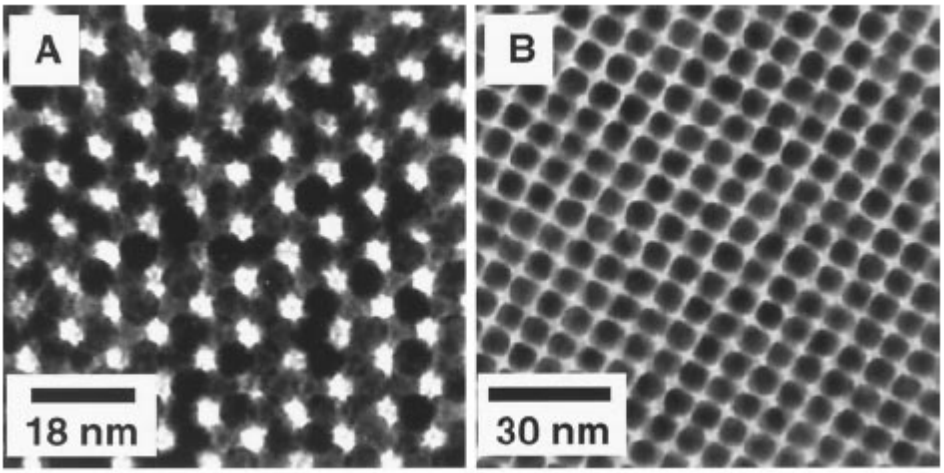

Fig. 2.11 The image of 6 nm FePt NPs self-assemble into (a) hexagonal superlattice and (b) square superlattice.[18]

Although composition of FePt NPs can be adjusted by changing the precursor ratio, there are still two disadvantages in Sun's method. First, the final composition is nonlinear to the original precursor ratio, shown in Fig. 2.13. This is because the decomposition of $Fe(CO)_5$ in gas phase is complicated and difficult to control. On the other hand, the high toxicity and flammability of $Fe(CO)_5$ also cause danger during the synthesis of FePt NPs. Further modifications are discussed in the following section.

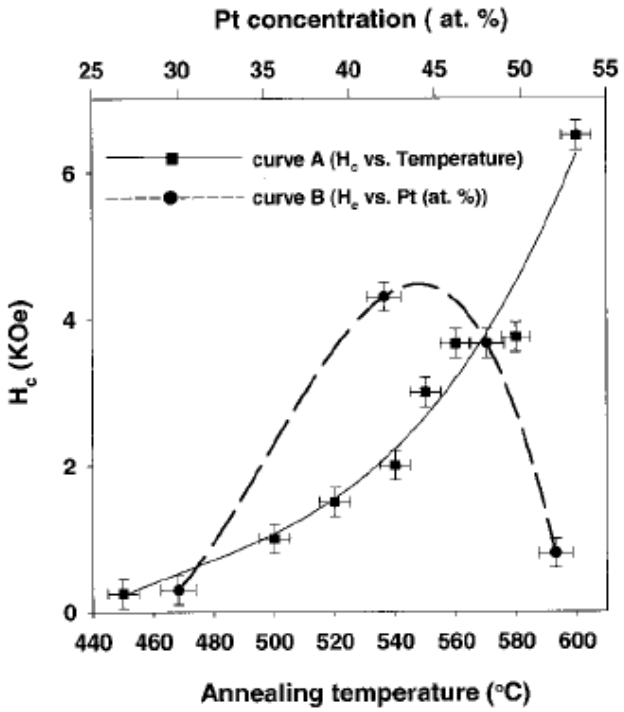

Fig. 2.12 Curve A shows the in-plane coercivity of FePt assemblies as a function of annealing temperature. Curve B indicates the composition-dependent coercivity.[18]

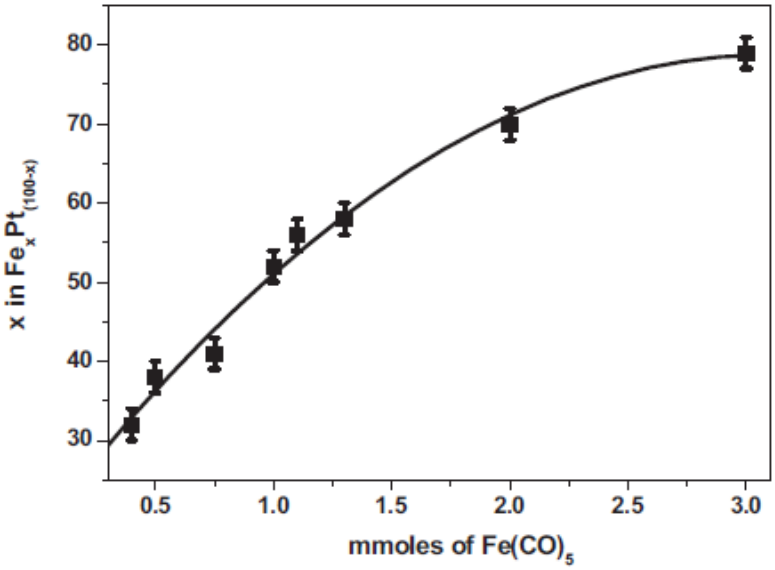

Fig. 2.13 Compositional relation between $Fe(CO)_5$ and *x* in Fe*x*Pt(100–*x*) based on the reaction of $Fe(CO)_5$ with 0.5 mmol of $Pt(acac)_2$.[53]

Further modification on the synthesis of FePt nanoparticles

Since the synthesis of FePt NPs was successfully achieved in 2000, many efforts were triggered to further modify it. In order to solve the

problem caused by $Fe(CO)_5$, different approaches were proposed. The co-reduction of metal salts by replacing $Fe(CO)_5$ with $Fe(acac)_3$ or $Fe(acac)_2$ was proposed and demonstrated.[54] The co-reduction of $Fe(acac)_3$ and $Pt(acac)_2$ generally leads to smaller FePt NPs with the size of 2 ~ 3 nm. Replacing the $Fe(CO)_5$ with $Fe(acac)_3$ or $Fe(acac)_2$ has the advantages of nontoxicity, nonvolatility, and storage stability of chemical reagents. The aqueous co-reduction process was demonstrated to synthesize FePt NPs.[55] The strong reducing agent, hydrazine (N_2H_4) was used to reduce the $H_2PtCl_6 \cdot H_2O$ and $FeCl_2 \cdot H_2O$ in the presence of sodium dodecyl surfate (SDS) or cetyltrimethylammonium bromide (CTAB) at the temperature of 70 °C. Finally, the fcc-structured FePt NPs were synthesized by the aqueous co-reduction process.

On the other hand, because the ordering of FePt NPs needs high temperature annealing, the addition of the third element into FePt NPs was investigated to reduce the ordering temperature and enhance the magnetic properties. To improve the magnetic properties and reduce the ordering temperature, the third elements, including Cu [56], Au [57], Ag [58], Co [59], Pd [60], Mn [61], and Sb [62], were added into the FePt NPs. The addition of Au, Ag, and Sb can significantly reduce the ordering temperature. It is because the high surface energy and low solubility of Au, Ag, and Sb make these dopants diffuse out of FePt lattice and leave behind excess vacancies which facilitate the rearrangement of Fe and Pt atoms. The addition of Cu into FePt forms FePtCu ternary alloy, which has lower energy of the disordered-ordered transformation. FeCoPt and FePdPt NPs annealed at high temperature did not possess higher coercivity than pure FePt NPs due to the lower magnetocrystalline anisotropy of CoPt and

FePd. We also have used Mn addition to enhance the magnetic properties of FePt NPs. A maximum coercivity of 19 kOe was obtained for $(Fe_{32}Pt_{68})_{87}Mn_{13}$ NPs annealed at 700^{o}C for 1h.

Finally, the agglomeration and sintering of FePt NPs during the high temperature annealing are also serious problems. The salt matrix was utilized to avoid these problems.[63-64] Fig. 2.14 shows the TEM images of 15 nm FePt NPs annealed with NaCl matrix. No serious agglomeration and sintering were found after annealing at 700°C with NaCl-to-FePt ratio of 100:1. It was found that increased annealing temperature and time should be accompanied by a higher NaCl-to-FePt ratio. A large coerciviey (up to 20 kOe) was obtained in the 15 nm FePt NPs annealed at 700°C with NaCl-to-FePt ratio of 100:1.

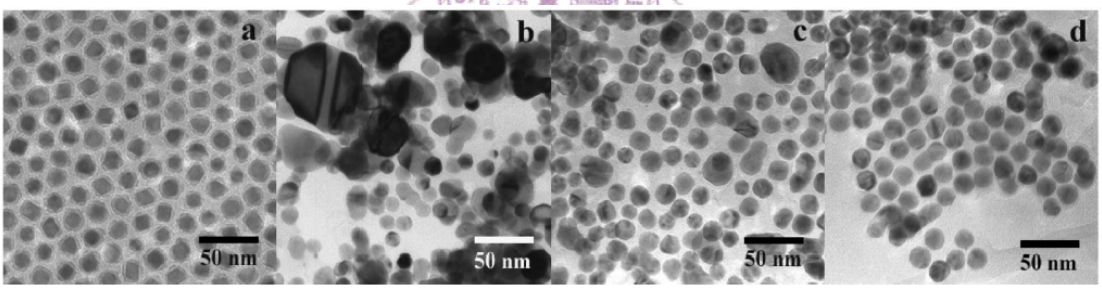

Fig. 2.14 TEM images of 15 nm FePt NPs (a) as synthesized and annealed in NaCl matrix at 700 °C for 2h with NaCl-to-FePt ratios of (b) 4:1, (c) 40:1, and (d) 100:1.[64]

2.3.3 The bimagnetic nanoparticles

Recently, the bimagnetic NPs have been received much attention due to the ability in tailoring their magnetic properties. The exchange-coupled nanocompoisite magnet has been developed through a bottom-up approach. One of the interesting systems is the FePt/Fe_3O_4 nanocomposite, which can be further transferred into an exchange-coupled FePt/Fe_3Pt hard magnetic nanocomposite.

The first experiment was carried out in the mixing of FePt and Fe_3O_4 NPs.[65] By control the relative size between FePt and Fe_3O_4 NPs, the binary NPs assemblies shows different packing configuration, shown in Fig. 2.15. The binary assemblies were converted into FePt-Fe_3Pt nanocomposite by annealing under a flow of Ar + 5 % H_2 at 650 °C for 1h. The disordered FePt was transferred to ordered FePt, simultaneously. The HRTEM image of FePt-Fe_3Pt nanocomposite was shown in Fig. 2.16. The magnetic properties were also influenced by the packing configuration of the binary assemblies. For the well mixed assembly of 4 nm FePt and 4 nm Fe_3O_4, the hysteresis loop shows single-phase-like behavior. However, for the separated assembly of 4 nm FePt and 12 nm Fe_3O_4, its hysteresis loop shows a two-phase behavior, shown in Fig. 2.17.

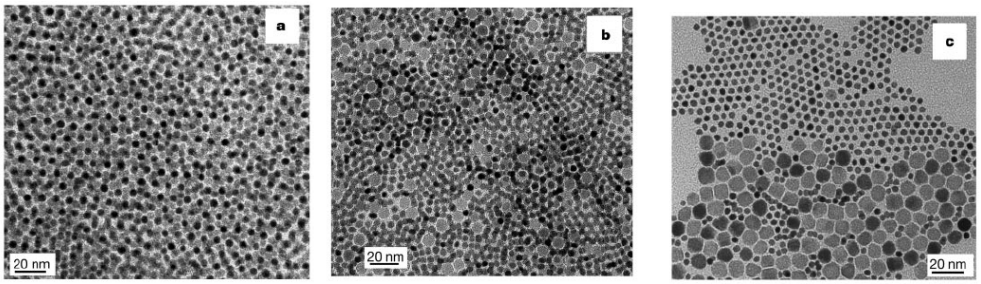

Fig. 2.15 TEM images show binary NP assemblies. a. FePt (4 nm): Fe_3O_4 (4 nm), b. FePt (4 nm): Fe_3O_4 (8 nm), c. FePt (4 nm): Fe_3O_4 (12 nm).[65]

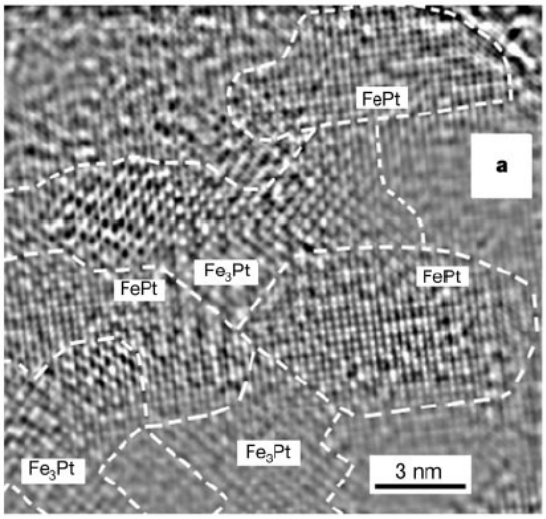

Fig. 2.16 HRTEM image of FePt-Fe_3Pt nanocomposite.[65]

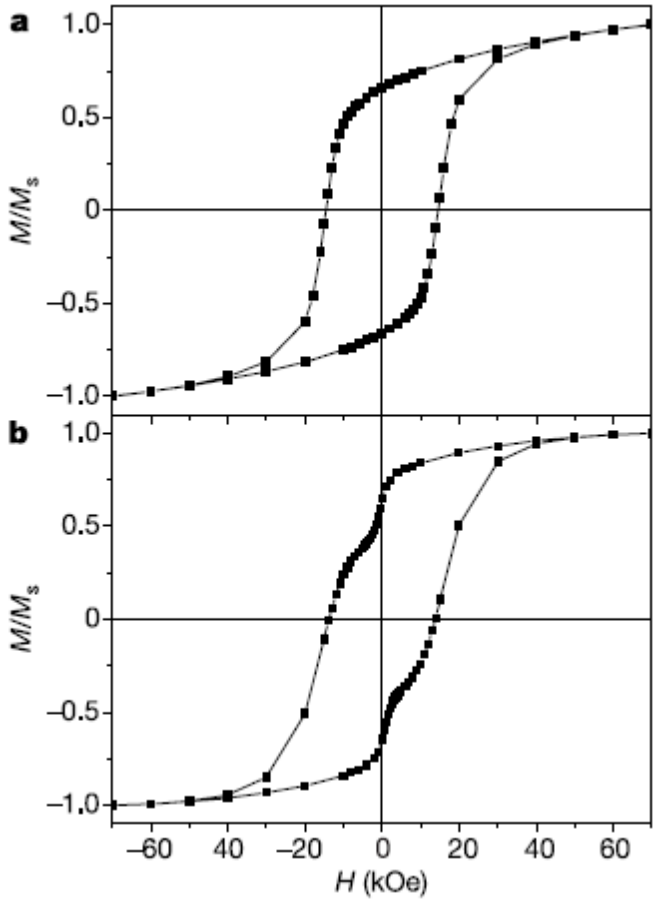

Fig. 2.17 Hysteresis loops of two FePt-based nanocomposites made from the mixture of (a) 4 nm FePt and 4 nm Fe_3O_4, and (b) 4 nm FePt and 12 nm Fe_3O_4.[65]

Because the FePt is magnetically hard phase and Fe_3Pt is soft phase, the exchange coupling between these two phases can result in optimum

energy product by tuning the size and composition of the individual NPs. In their experiment, they found that the exchange-coupled FePt-Fe_3Pt nanocomposites have a giant energy product of 20.1 MG Oe, which exceeds the theoretical limit of 13 MG Oe for non-exchange-coupled FePt.

The other approach to prepare the FePt and Fe_3O_4 nanocomposites is synthesizing the core/shell-structured FePt@Fe_3O_4 NPs, which can provide the perfect interface between the hard and soft phase.[30] On the other hand, the composition of hard phase and soft phase can be adjusted by tuning the shell thickness of Fe_3O_4. Fig. 2.18 (a) and (b) show TEM images of FePt@Fe_3O_4 core/shell NPs with the shell thickness of 0.5 nm and 2 nm, respectively. Interestingly, the magnetic properties of as-synthesized FePt@Fe_3O_4 NPs were also affected by the shell thickness of Fe_3O_4, shown in Fig. 2.19.

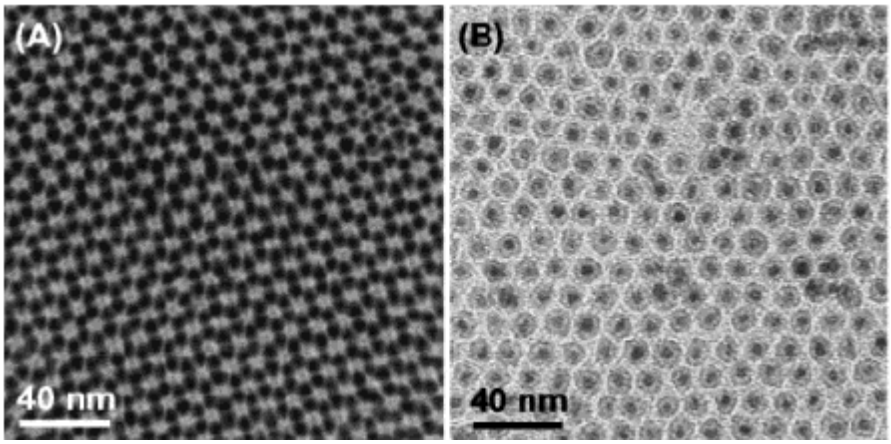

Fig. 2.18 TEM images of T FePt@Fe_3O_4 core/shell NPs with the shell thickness of (a) 0.5 nm and (b) 2 nm. The diameter of FePt core is 4 nm.[30]

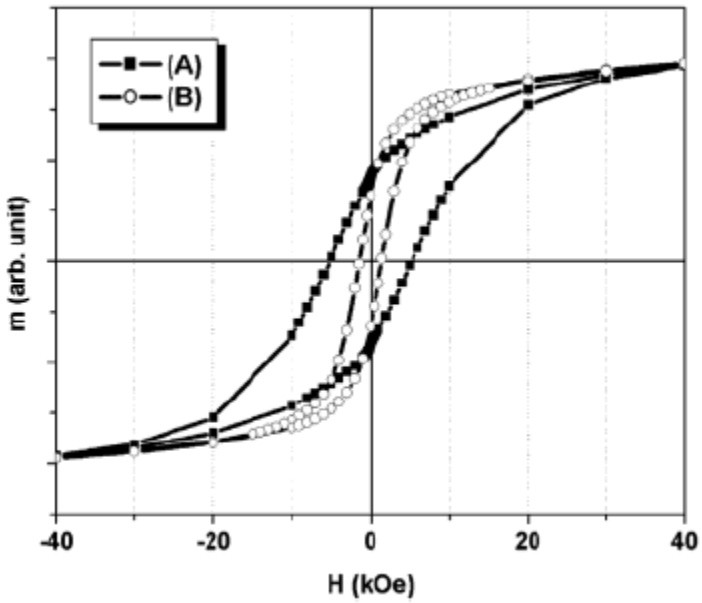

Fig. 2.19 Hysteresis loops measured at 10 K for FePt@Fe_3O_4 NPs with the shell thickness of (a) 0.5 nm and (b) 2 nm.[30]

2.4 The shape control of magnetic nanoparticles

Controlling the shape of nanomaterials can tailor and manipulate the physical and chemical properties of materials. The non-spherical nanocrystals can have anisotropically optical, magnetic, catalytic and transporting properties. The bound facets of nanocrystals and the surface to volume ratio provide unique surface properties. For instance, the catalytic reactivity and selectivity of Pt NPs can be adjusted by controlling their shape which determines the exposed crystallographic facets.[66] The CdSe NPs also show shape dependent properties.[67] Spherical CdSe NPs have circularly polarized emission properties, while linearly polarized emission is observed from CdSe nanorods. The shape of magnetic NPs dominates magnetic shape anisotropy and surface anisotropy,[68] and it makes NPs become good building blocks to construct controlled assembly which is a prerequisite for the generation of magnetic nanodevice, such as magnetic NP media.

2.4.1 The general concepts and strategies for the shape control of nanoparticles

The surface energy and crystallinity are important factors related to the morphology of NPs. For materials with an isotropic surface energy such as an amorphous solid, the perfectly symmetric sphere is the most stable shape to decrease the total surface energy. However, for the noble metals which possess different surface energies for different crystal planes, the nanocrystals are usually bound by the low-index crystal planes that exhibit close atomic packing. Hence the surface energy of the crystalline

nanocrystals determines the terminated facets and shape. Furthermore, the single-crystalline or multiply twinned structures of nanocrystals also show different morphologies of nanocrystals. For single-crystalline nanocrystals, their terminated facets are usually bound by the low-index {111}, {100}, and {110} planes resulting in thermodynamic equilibrium shapes of cube, truncated cube, octahedron, and truncated octahedron…*etc.*, shown in Fig. 2.20. The multiply twinned particles (MTPs) are typically found in the completely (111)-bound particles, in which the (111) planes have the lowest surface energy. The minimization of surface energy due to the presence of (111) facets can allow the presence of twinned structure. The most commonly observed multiply twinned polyhedrons are the decahedron with 10 faces and the icosahedron with 20 faces.

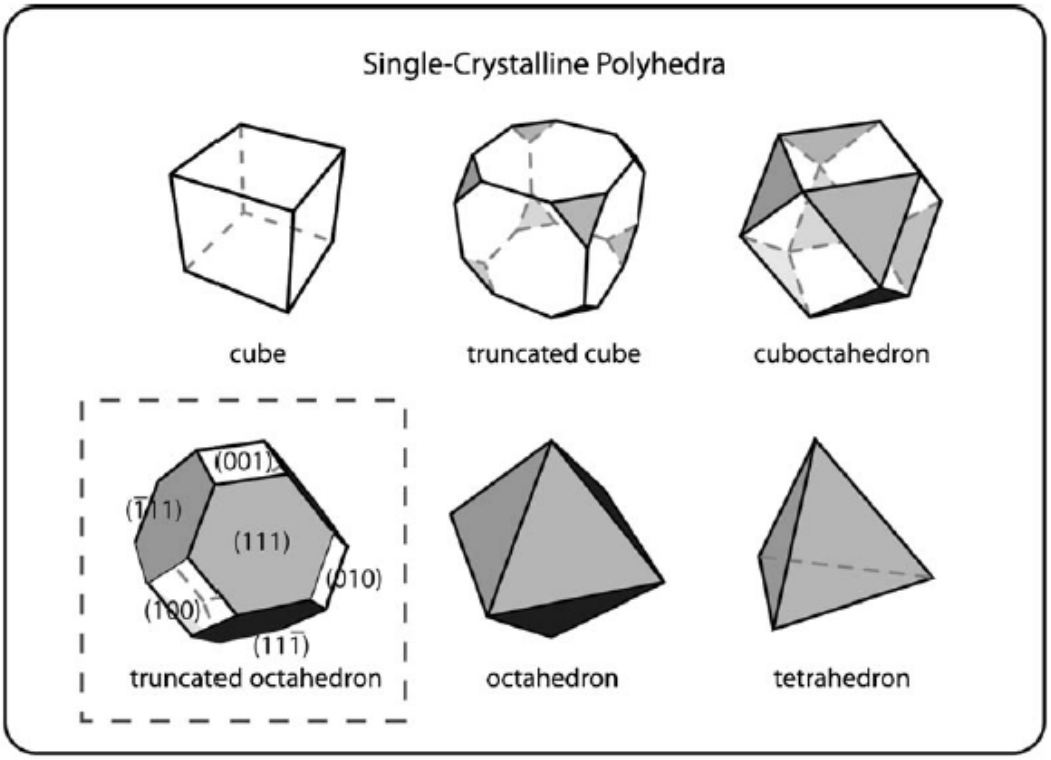

Fig. 2.20 Common morphologies of single-crystalline metal NPs.[69]

The shape control of nanocrystals is strongly dependent on the nucleation and growth condition. In general, the highly crystalline nuclei and anisotropic growth are important for shape control of nanocrystals. There are two common types of nucleation, including homogeneous nucleation and heterogeneous nucleation. For the homogeneous nucleation, the La Mer model depicts that the nucleation occurs when the concentration of atomic species in solution is higher than a critical value, shown in Fig. 2.21. After the occurrence of nucleation, the atomic species are rapid depleted. Then their concentration is below the critical value again. So the further nucleation is discouraged, and the subsequent growth occurs on the pre-existing nuclei. It is believed that the rapid nucleation rate is crucial for preparing the non-spherical nanocrystals.[69] When the reduction of precursor is extremely fast, most seeds become single-crystal due to their rapidly increased size. For the heterogeneous nucleation, the activation energy for atomic species nucleating on the pre-existing seeds is lower than that for homogeneous nucleation. Hence, the heterogeneous nucleation can be considered as an overgrowth process. The growth condition becomes crucial for the shape control of nanomaterials.

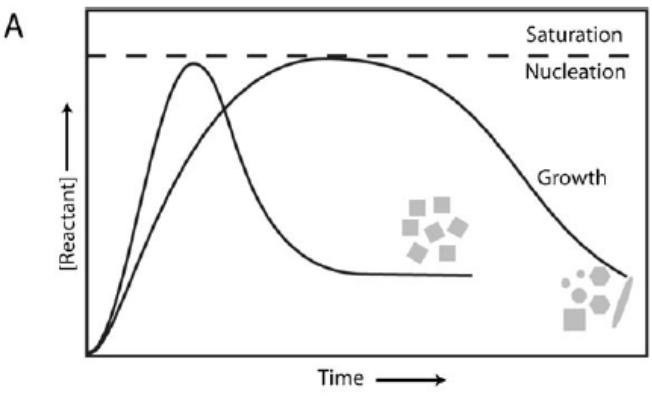

Fig. 2.21 The La Mer model of nucleation.[69]

The selective growth also plays an essential role in controlling the shape of NPs. Xiong *et al.* has proposed that the ratio (R) of growth rate along [100] and [111] direction affects the final shape of Pd NPs, shown in Fig. 2.22.[70] The planes with fast growth rate finally disappear, while the planes with slow growth rate become the terminated planes of shaped NPs. When the growth rates of each planes become competitive, the shaped NPs may possess more than one terminated planes.

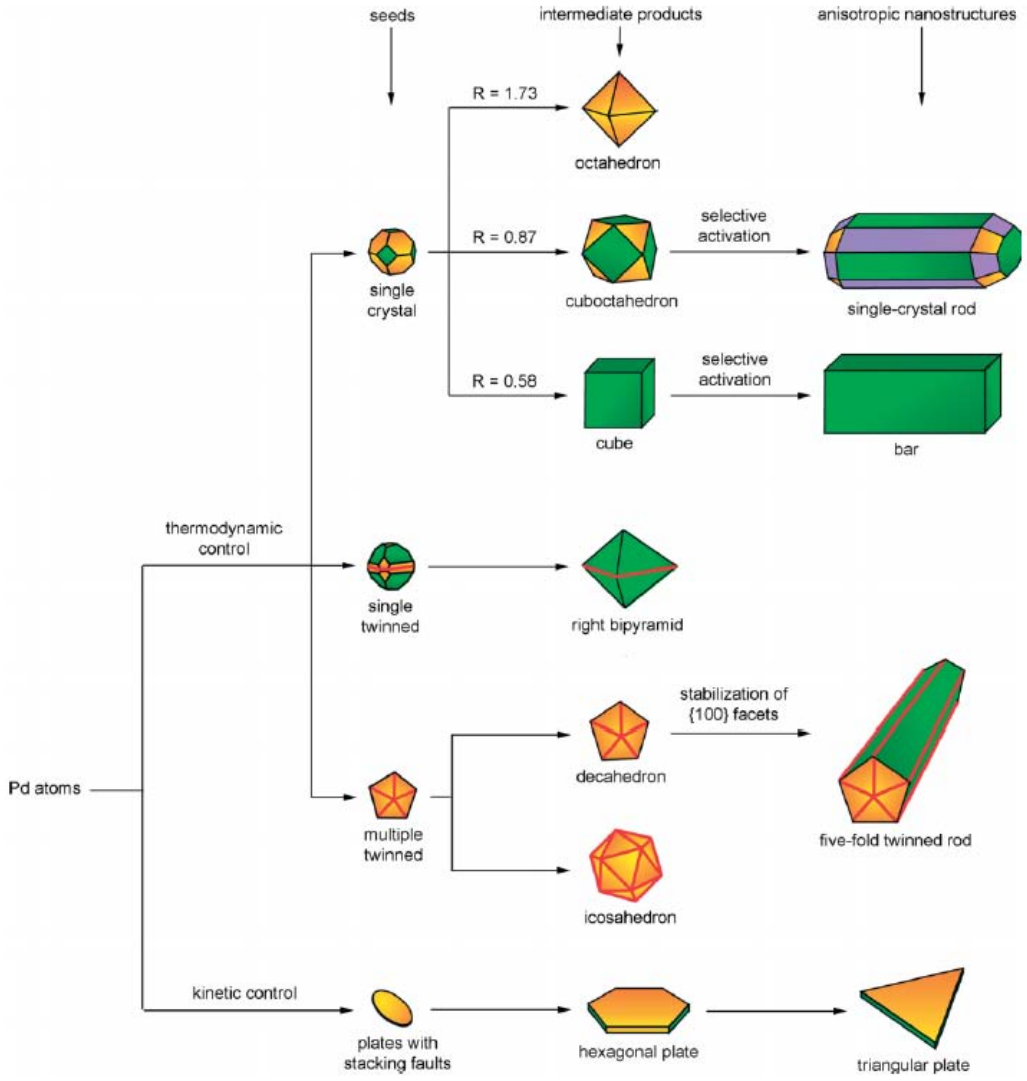

Fig. 2.22 A schematic illustration of the reaction pathways that lead to Pd nanostructures with different shapes.[70]

Capping surfactant effect and kinetically controlled growth are two practicable approaches to control the shape of NPs.[71] Various surfactants can be bound to specific planes of NPs and reduce the growth rate of the bound planes, leading to anisotropic growth. Hence, the terminated planes of NPs can be changed by adjusting specific surfactants. Kinetically controlled growth is the other common approach to synthesize shaped NPs. The supply of sufficient thermal energy during synthesis is the main factor to create the kinetically controlled growth condition. When the thermal energy is sufficient in the system, the removal of high-energy planes becomes thermodynamically favorable.[72]

2.4.2 The shape control of magnetic nanoparticles

The shaped $MnFe_2O_4$ nanoparticles

In 2004, Hao Zeng *et al.* found that the size of $MnFe_2O_4$ particles can be tuned by varying the concentration of the precursors.[73] The higher precursor concentration leads to larger particle size. On the other hand, the shape can be controlled by the amount of surfactants. When the ratio of surfactants to Fe precursor is equal to 3, the cubic $MnFe_2O_4$ NPs formed. Interestingly, if the $MnFe_2O_4$ NPs were synthesized by two-step seed-mediated method with the same surfactants to Fe precursor ratio, the shape becomes polyhedral. Fig. 2.23 shows the TEM images of shaped $MnFe_2O_4$ NPs. The authors also demonstrated that the shape of nanocrystals can induce specific superlattice. From the XRD measurement, shown in Fig. 2.24, the cubic NPs show the strongest (400) peak which is corresponding to the terminated planes of $MnFe_2O_4$ nanocubes. However, the polyhedral NPs show the strongest (220) peak.

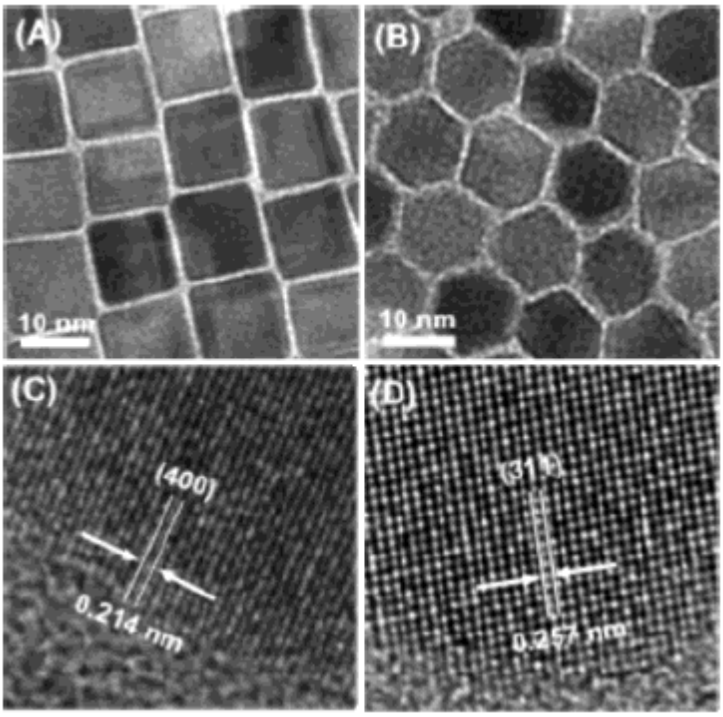

Fig. 2.23 TEM images of the cubic $MnFe_2O_4$ NPs (a)(c), and polyhedral NPs (b)(d).[73]

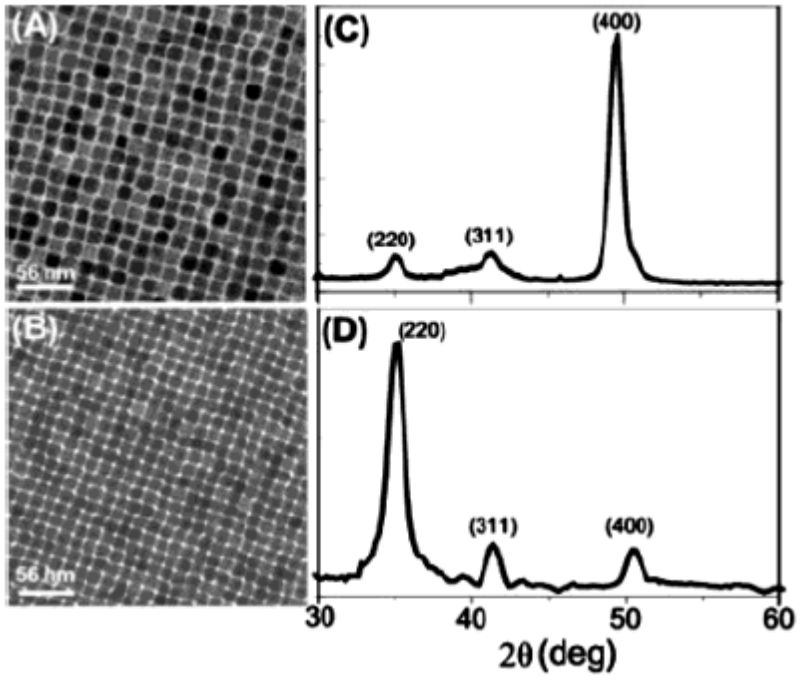

Fig. 2.24 TEM images of 12 nm $MnFe_2O_4$ NP superlattices of (A) cubelike and (B) polyhedron-shaped NPs. XRD of (C) cubelike and (D) polyhedron-shaped NP superlattice on Si(100) substrates.

The shaped Fe_3O_4 nanoparticles

Even the shape control of $MnFe_2O_4$ NPs has been developed in 2004, the shape control of Fe_3O_4 NPs was achieved till 2007. Kovalenko *et al.* have prepared the cubic Fe_3O_4 nanocubes by using fatty acid salts as stabilizers.[15] Unlike the commonly used approach to tailor the ligand performance by modifying the length and structure of nonpolar group, they changed the cations of the oleate stabilizer. In their experiments, Sodium oleate (NaOL), potassium oleate (KOL), dibutylammonium oleate (DBAOL), and oleic acid were utilized as the surfactants. Cubic NCs with size of 9-23 nm were obtained in the presence of NaOL and KOL, while the DBAOL and OA induced spherical NPs. This is because replacing OA by its oleate salts can vary the concentration of "free" oleate ions in solution. The higher oleate concentration is advantageous to the formation of cubic Fe_3O_4 NPs. The TEM images were shown in Fig. 2.25.

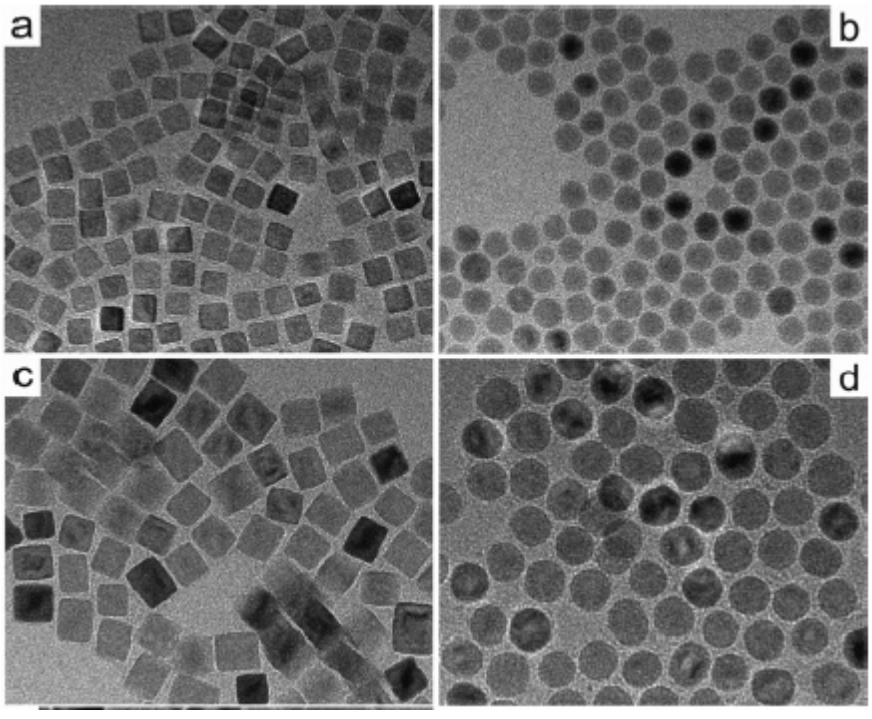

Fig. 2.25 TEM images of cubic (a, c) and spherical (b, d) Fe_3O_4 NPs.[15]

Yang *et al.* also developed another approach to synthesize the cubic Fe_3O_4 NPs by adjusting the relative amounts of oleic acid (OA) and oleylamine.[44] Because the carboxylic group, -COOH, of OA can selectively bind onto differing crystal facets and the nonpolar tail group in OA can provide steric hindrance. However, the $-NH_2$ group in oleylamine has a weak and isotropic binding onto the surface of particles. Hence, in Yang's experiments, they increased the amount of OA while reduced the amount of oleylamine to synthesize the Fe_3O_4 nanocubes. The size of nanocubes can be varied from 6.5 to 30 nm by the heating rate and the reflux time. The TEM images were shown in Fig. 2.26.

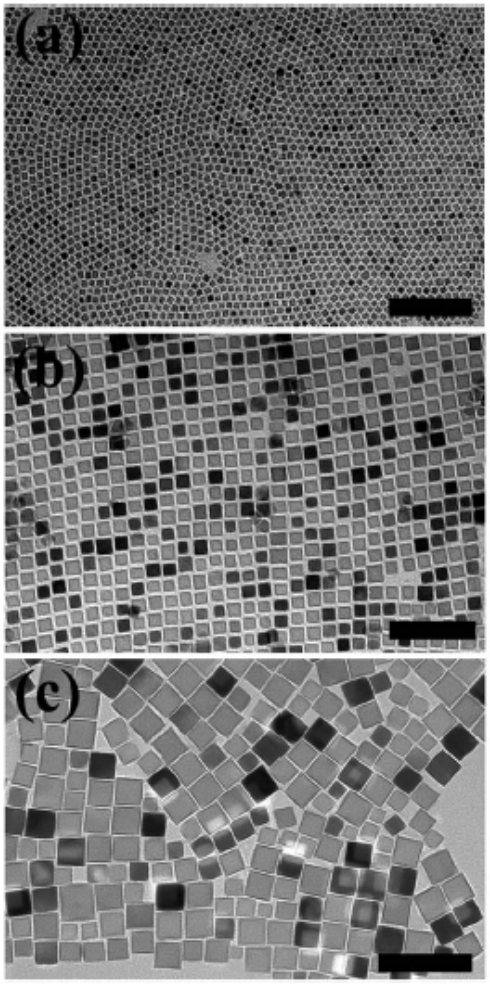

Fig. 2.26 TEM images of Fe_3O_4 nanocubes with different sizes (a) 6.5 nm, (b)15.0 nm and (c) 30.0 nm.[44]

Recently, the larger Fe_3O_4 nanocubes were synthesized by Kim *et al*. The features of their approach are increasing the precursor concentration and reaction time. No reductant was used in their approach. The largest size of 110 nm was synthesized by mixing 5.2 g benzyl ether, 1.13 g oleic acid and 0.71 g iron (III) acetylacetonate and reacted at 290^{o}C for 1h. By increasing the reaction time to 1.5 and 2 h, the particles grew into a larger and more perfect cubic shape with the size of 150 and 160 nm, respectively. The TEM images were shown in Fig. 2.27.

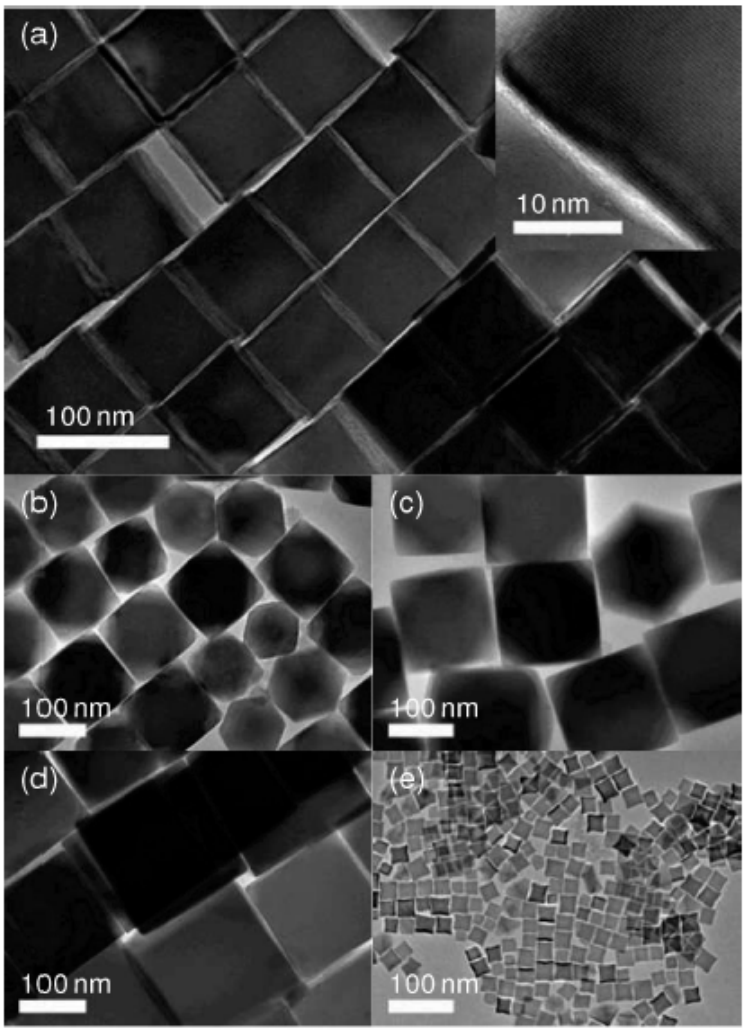

Fig. 2.27 TEM images of (a) 79-nm-sized Fe_3O_4 nanocubes (inset: HRTEM image); (b) mixture of truncated cubic and truncated octahedral NPs with an average dimension of 110 nm; (c) 150-nm-sized truncated nanocubes; (d) 160-nm-sized nanocubes; (e) 22-nm-sized nanocubes.[17]

2.4.3 The shape-induced superlattice

The self-assembly of NPs is always of great interest because the regular superlattice of NPs were critical for the development of nanodevice. In general, the spherical NPs are favor to self-assembly into hexagonal array due to the close package. It was found that the capping surfactants also affect the packing array of NPs. Sun *et al.* has found that 6 nm FePt NPs self-assembly into hexagonal close-packed 3D array when the capping surfactants are oleic acid and oleylamine.[18] However, if the capping surfactants are exchanged to hexanoic acid and hexylamine, the FePt NPs assembly into cubic packed multilayer.

Because of the achievement in synthesizing techniques, various shaped NPs have been successfully synthesized. Hence, how the anisotropic shaped NPs arrange themselves becomes an interesting issue. Song *et al.* have found that the Fe_3O_4 NPs with the shapes of truncated tetrahedral platelets (TTP), truncated octahedrons (TO), and octahedraons (OT) self-assembled into hexagonal, primitive cubic, and distorted body-centered cubic (bcc) superlattice structure, respectively.[74] Their TEM images were shown in Fig. 2.28, 2.29, and 2.30, respectively. All three types of superlattice structure follow the facet-to-facet mode. On the other hand, even though the spherical NPs can self-assembly into different packed arrays, the crystallographic orientation ordering was less observed. However, the crystallographic orientation-ordered superlattices can be achieved by the self-assembly of shaped and single crystalline nanocrystals. The electron diffraction patterns recorded from the crystallographic orientation-ordered superlattices show the arced-spot pattern instead of ring pattern. Such results clearly demonstrated that the

shape of nanocrystals plays a crucial role in both the superlattice structure and the crystallographic orientation of three-dimensional superlattices.

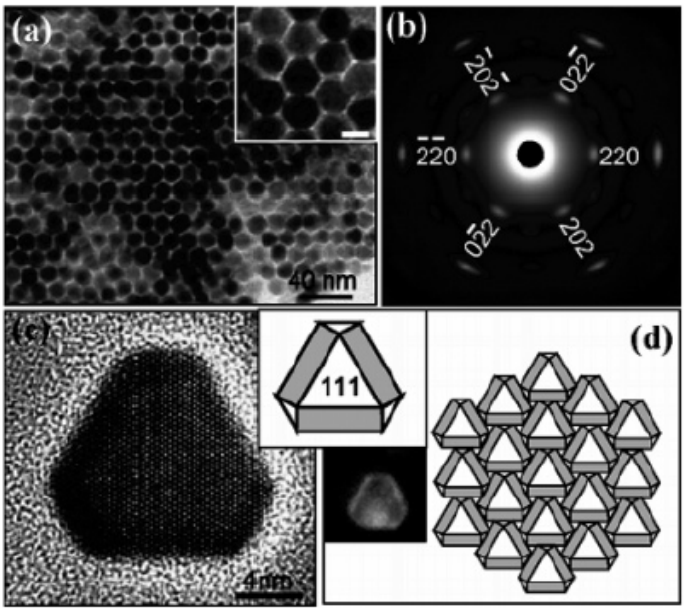

Fig. 2.28 (a) TEM image of the self assembly of TTP Fe_3O_4 NPs, (b) The corresponding SAED patterns, (c) HRTEM image, (d) Top-view model of the superlattices.[74]

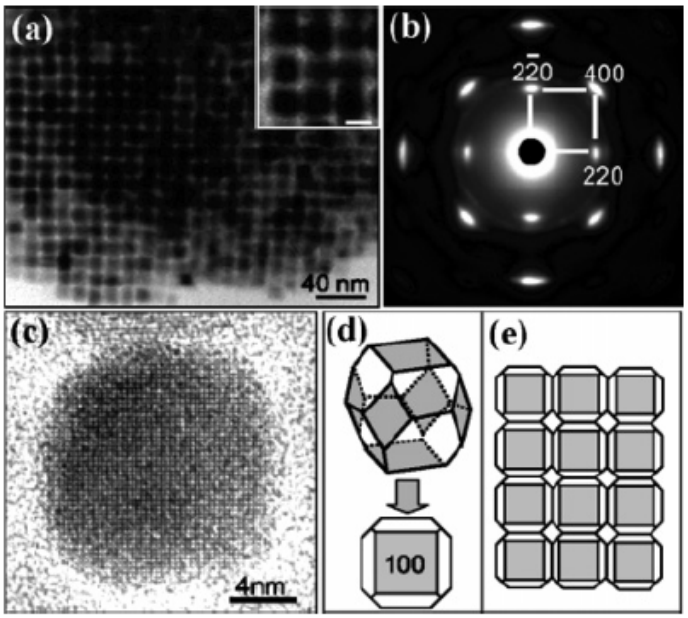

Fig. 2.29 (a) TEM image of the self assembly of TO Fe_3O_4 NPs, (b) The corresponding SAED patterns, (c) HRTEM image, (d) Top-view model of the superlattices.[74]

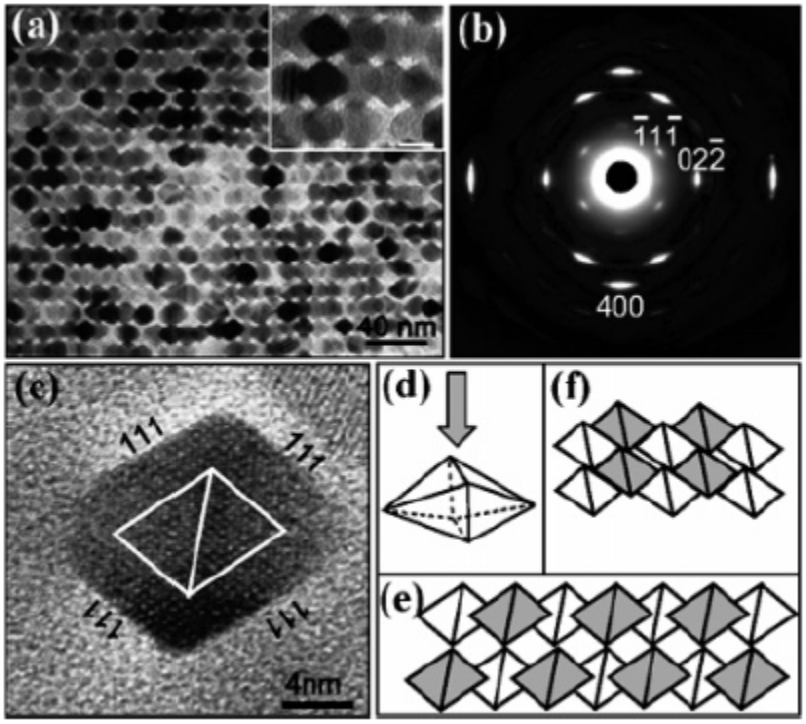

Fig. 2.30 (a) TEM image of the self assembly of octahedral Fe_3O_4 NPs, (b) The corresponding SAED patterns, (c) HRTEM image, (d) Top-view model of the superlattices.[74]

It is intriguing that why the shape of nanicrystals determine its structure of superlattices. Yammamuro *et al.* have calculated the potential energies of cubic nanocrystals with a square array and a quasi-hexagonal array.[75] From the potential energy caused by van der Waals interactions, the reduced potential energy of square array is larger than that of quasi-hexagonal array. Their calculation also indicates that the nearest neighbors play a decisive role to determine the lattice symmetry of the array. Therefore, when the two cubic particles meet, the facet-to-facet attachment is the most effective way to shorten the center-to-center distance.

2.5 The application of magnetic nanoparticles

2.5.1 FePt nanoparticle arrays for recording media application

FePt is the most promising material for the future high density recording media due to its high magnetocrystal anisotropy. Self-assembled FePt NPs arrays are considered as the prospective magnetic –media candidate. If each FePt NP can perform as one bit in recording media, the recording density can be improved to several Tbits/in^2. Sun *et al.* has demonstrated the recording signal in the self assembly of FePt NPs. Fig. 2.31(a) is the HRSEM image of the self-assembled FePt NPs. Fig. 2.31(b) shows it corresponding magneto-resistive (MR) signals that are read back from the transitions by the MR sensor. The digitized read-back signals have linear densities of 500, 1000, 2000, and 5000 flux changes per millimeter, indicating that the ferromagnetic FePt NP assembly can indeed support magnetization reversal transitions.

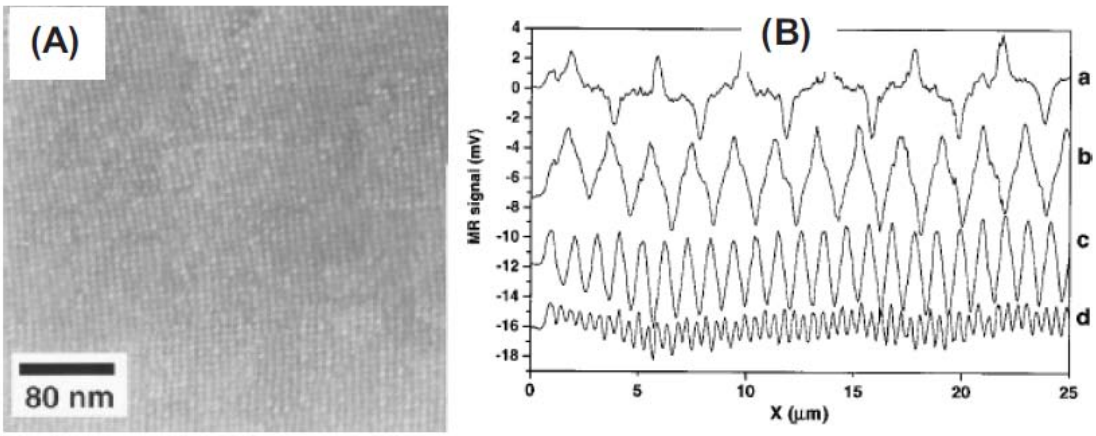

Fig. 2.31 (A) HRSEM image of a 120 nm thick 4 nm FePt ferromagnetic NP assembly used for a writing experiment. B) Magneto-resistive read-back signals from the written bit transitions. The individual line scans reveal magnetization reversal transitions at linear densities of a) 500, b) 1040, c) 2140, and d) 5000 flux charges/mm.[18]

2.5.2 The catalytic ability of Fe_3O_4

In addition to the application in magnetic recording, magnetic particles, such as Fe_3O_4, have been employed as a catalyst for the removal of heavy metals in rinsing wastewater, such as As(III), As(V), Gd(II), Cr(VI), and Cu(II).[31-32] Fe_3O_4 was also used as the catalyst for the high-temperature water gas shift reaction which is an essential process to adjust the CO/H_2 ratio in the industrial production of hydrogen.[76] On the Fe_3O_4{001} planes, water tends to dissociate in oxygen vacancies on the defective site and partially dissociate on the nondefective surface.[77] However, on the Fe_3O_4{111} planes, water tends to fully dissociate. It was reported that the catalytic ability of Fe_3O_4 is related to the presence of both ferrous (Fe^{2+}) and ferric (Fe^{3+}) ions in its inverse spinel structure.[77] Interestingly, the surface reconstruction has been observed on Fe_3O_4(001) surface. In the [100] direction of Fe_3O_4, two types of layers alternate: A layers contain the tetrahedral iron (Fe_A^{3+}) and B layers contain the octahedral iron ($Fe_B^{2+,\ 3+}$) and oxygen, shown in Fig. 2.32. The $(\sqrt{2}\times\sqrt{2})R45°$ reconstruction on Fe_3O_4(001) surface with the terminated B layers has been observed, shown in Fig. 2.33.[78] Finally, it was found that the Fe_3O_4(001) surface has a higher Fe^{3+}/Fe^{2+} ratio than the bulk from the X-ray photoelectron spectrum (XPS).

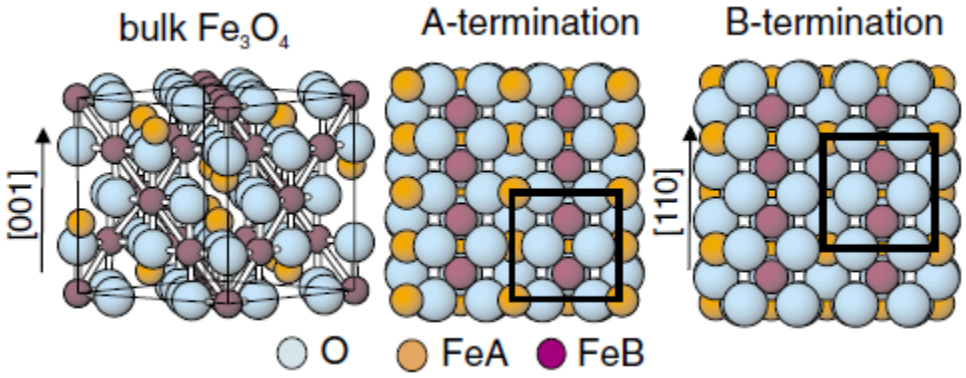

Fig. 2.32 The inverse spinel structure of magnetite is together with a top view of the two bulk truncations of Fe_3O_4 (001) with an A and a B layer, respectively. Oxygen atoms, FeA, and FeB are marked by white (light blue), gray (orange), and black (purple) circle.[78]

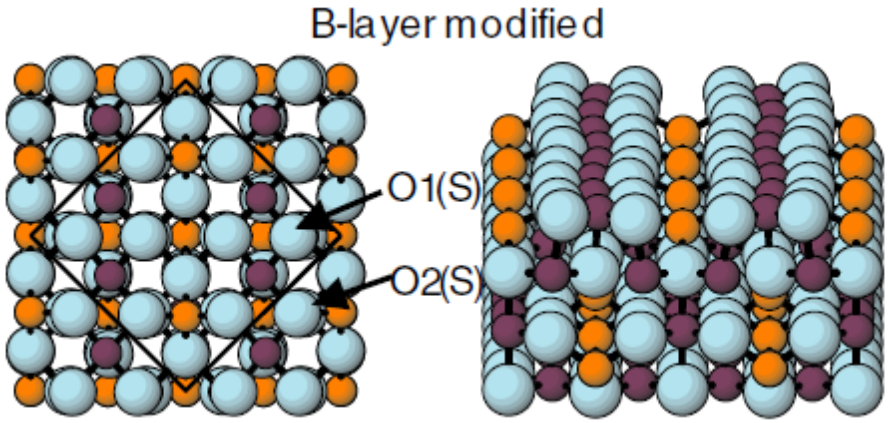

Fig. 2.33 Surface structure model of Fe_3O_4(001)-($\sqrt{2}\times\sqrt{2}$)R45 reconstruction.[78]

2.5.3 Magnetic nanoparticles for biomedical application

Magnetic NPs have been largely studied and utilized in biomedicine. Because the magnetic NPs can be manipulated by an external magnetic field, the transport of the magnetic NPs and the attached biological entities can be performed. In addition, the size of magnetic NPs is comparable to those of a biological entity, such as a cell (10-100 μm), a virus (20-450 nm), and a protein (5-50 nm).[79] Among all biomedical applications, magnetic NPs as the MRI contrast agents are widely studied. The magnetic gradient produced by the magnetic NPs can locally affect the magnetization states of the surrounding water, which enhances the contrast of magnetic resonance image (MRI). The details of magnetic NPs designed for MRI applications were discussed.

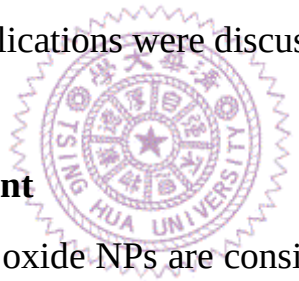

MRI contrast enhancement

Superparamagnetic iron oxide NPs are considered as the potential MRI contrast agents as early as the mid 1980s. The iron oxide NPs are biocompatible and have a predominant T_2-effect. T_2 means the **spin-spin relaxation time**, which is the time when the signal amplitude of magnetic resonance has been reduced to 36.8% of its original value after excitation. Commonly used iron oxide materials are magnetite (Fe_3O_4) and maghemite (γ-Fe_2O_3). According to their size, the iron oxide agents can by sub-divided into three groups. NPs with the size less than 20 nm are referred to MION (monocrystalline iron oxide NPs). USPIO (ultra small superparamagnetic iron oxide particles) refers to the NPs the size approximately 50 nm. SPIO (superparamagnetic iron oxide particle)

refers to particles with aggregated iron oxide cores and a mean particle diameter greater than 50 nm.

The efficiency by which a contrast agent can accelerate the proton relaxation rate in a homogeneous medium is called relaxivity of the agent and is defined by:

$$R_2 = R_2^0 + r_2 C \tag{2.5}$$

Where R_2 ($R_2 = 1/T_2$, unit s^{-1}) is the proton relaxation rate in the presence of the contrast agent, R_2^0 is the relaxation rate in the absence of contrast, and C is the contrast agent concentration (unit mM). The constant of proportionality, r_2 (unit $s^{-1}mM^{-1}$), is called relaxivity and is a measure of how much the proton relaxation rate is increased per unit of concentration of contrast medium. The contrast agents with larger r_2 are preferable because it means less contrast agent is required to obtain significant contrast enhancement. The r_2 is strongly related to the magnetic moment (μ) and the relaxation process of the magnetic spin (τ). The magnetic moment of NPs is influenced by the size, composition, and, magneto-crystalline phase of the NPs, shown in Fig. 2.34. Therefore, how to increase the saturation magnetization of magnetic NPs is a key study to design the synthesis of magnetic NP for MRI application.

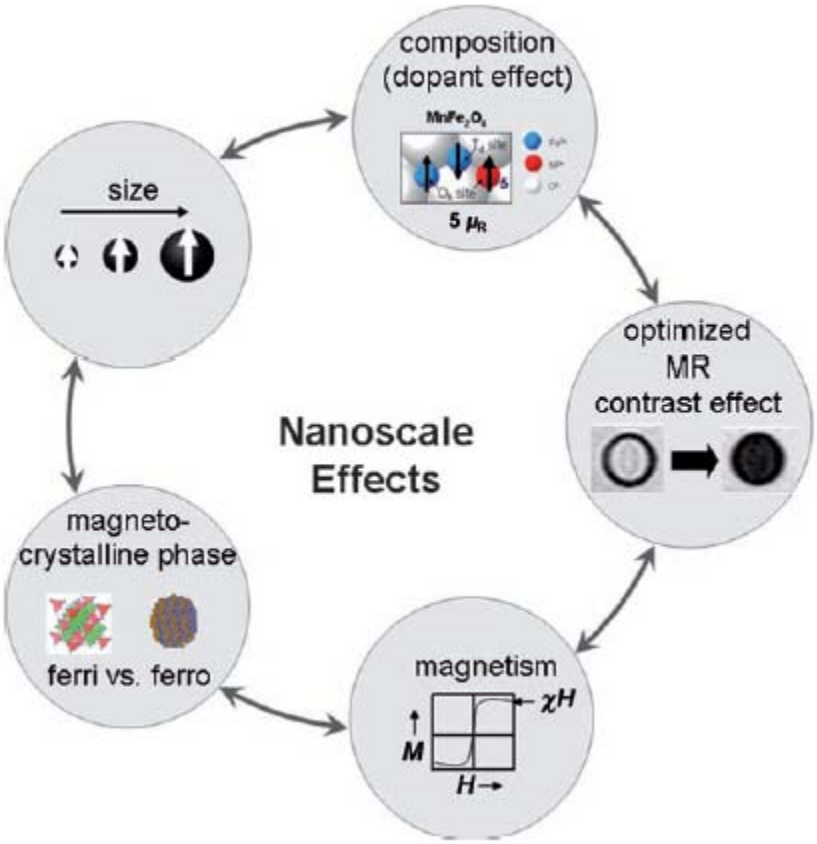

Fig. 2.34 Important parameters of MNPs for MRI contrast-enhancement effects.[80]

The size of magnetic NPs is one important parameter for the MRI contrast enhancement effect. In general, the smaller NPs contributed lower saturated magnetization due to the formation of magnetically dead layer on the surface. Therefore, for the identical magnetic material, the smaller NPs have worse r_2. The size effect of MRI contrast has been demonstrated in the case of Fe_3O_4 NPs, shown in Fig. 2.35. The size varied from 4 nm to 6, 9, and 12 nm results in mass-magnetization values of 25, 43, 80 and 101 emu per gram Fe, respectively. The r_2 relaxivity also increased with the increased particle size.

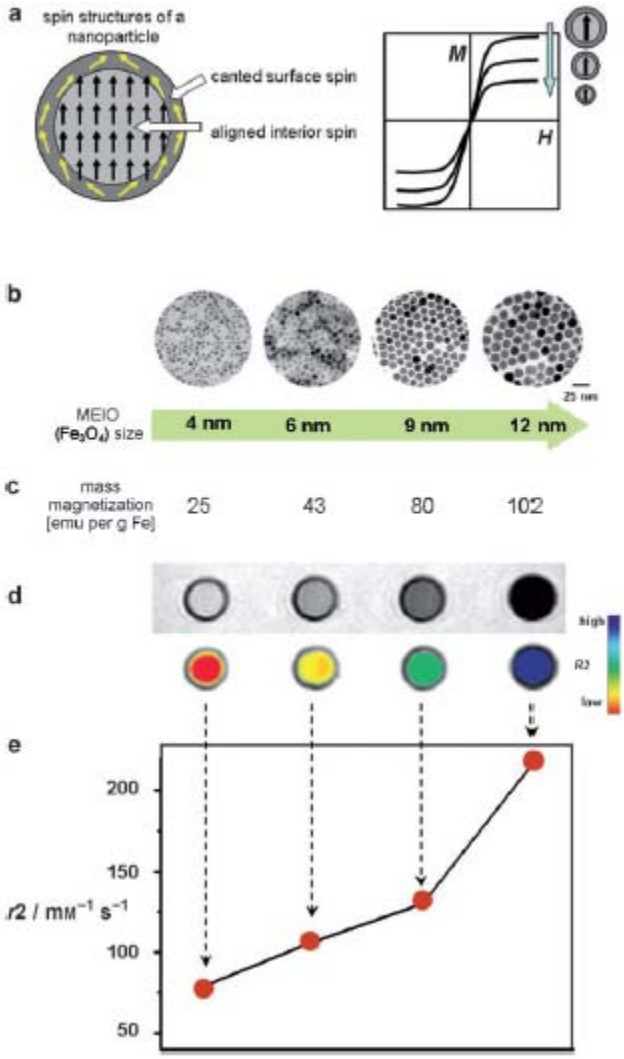

Fig. 2.35 (a) surface spin canting effect of NPs on magnetization. (b) TEM images of Fe_3O_4 NPs with different sizes. (c) mass magnetization, (d) T_2-weighted MR images, (e) the r_2 relaxivity of NPs.[80]

Adjusting the composition and doping other elements into magnetic materials were used to improve the saturation magnetization of magnetic NPs. For example, the spin configuration of Fe_3O_4 is $(Fe^{3+}\downarrow)_A(Fe^{2+}\uparrow Fe^{3+}\uparrow)_BO_4$, in which **A** means the tetrahedral sites and **B** means the octahedral sites. The magnetic moments contributed by the anti-parallel Fe^{3+} ions on **A** and **B** sites are canceled out, and the net magnetic moment is only contributed and dominated by Fe^{2+} ions on the **B** site which have 4

μ_B. Therefore, substituting Fe^{2+} on the **B** site by other transition-metal dopants M^{2+}, such as Mn, Ni, and Co, is the other way to adjust the saturated magnetization of magnetic NPs, shown in Fig. 2.36. According to their spin configuration, the theoretical magnetic moments of per unit $MnFe_2O_4$, $CoFe_2O_4$, and $NiFe_2O_4$ are 5 μ_B, 3 μ_B, and 2 μ_B, reapectively. The r_2 values of $MnFe_2O_4$, Fe_3O_4, $CoFe_2O_4$, and $NiFe_2O_4$ are 358, 218, 172, and 152 $mM^{-1}s^{-1}$, respectively. Recently, large r_2 of 860 $mM^{-1}s^{-1}$ was reported in the $(Zn_{0.4}Mn_{0.6})Fe_2O_4$ NPs.[81] Noteworthily, the Zn^{2+} ions, which have 0 μ_B, occupied the **A** sites. Therefore the cancellation between **A** and **B** site was significant reduced. The saturation magnetization of Zn-doped NPs was increased.

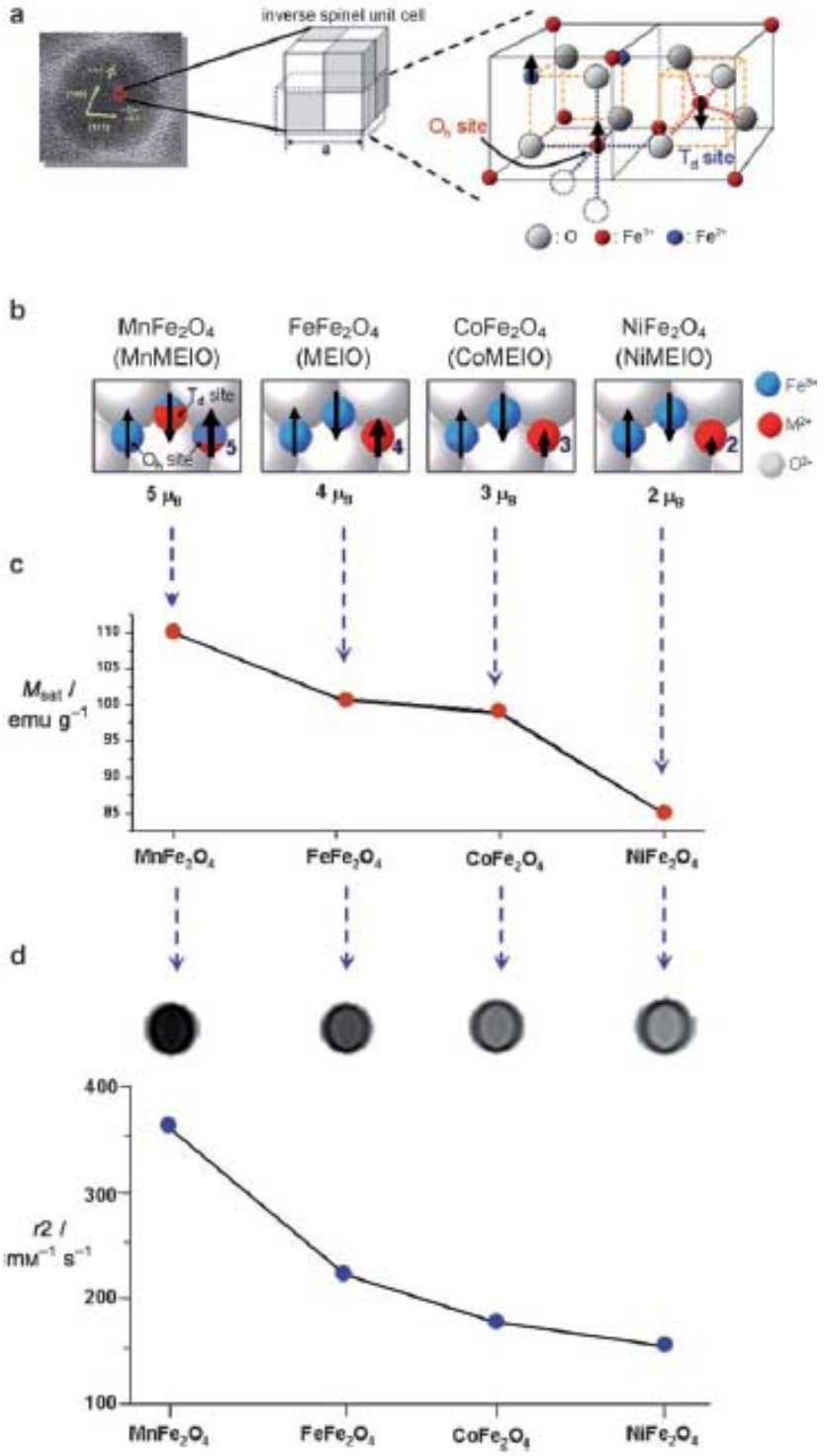

Fig. 2.36 (a) the structure of inverse spinel, (b) magnetic spin structure, (c) the mass magnetization, (d) the r_2 relaxivity.[80]

Chapter III

Experimental Techniques and Instrumentation

3.1 Experimental techniques

3.1.1 Chemical reagents

Iron(III) acetylacetonate ($Fe(acac)_3$, 99.9+%), Platinum(II) acetylacetonate ($Pt(acac)_2$, 97%), and Manganese(III) acetylacetonate ($Mn(acac)_2$, 99%) are as the precursors. 1,2-hexadecanediol (90%) and 1,2-tetradecanediol (90%) are as the reductant. Oleic acid ($C_{17}H_{33}COOH$, 90%) and oleylamine ($C_{18}H_{35}NH_2$, 99%) are as the surfactant. Benzyl ether ($C_{14}H_{12}O$, 99%) which has the boiling point of 290°C is as the solvent. All chemical reagents are purchased from Aldrich and used as received without further purification.

3.1.2 Typical synthesis of magnetic nanoparticles

Typical synthesis of magnetic NPs was carried out by using standard Schlenk line techniques under Ar atmosphere. In a typical synthesis process, precursors, such as $Pt(acac)_2$, $Fe(acac)_3$ and $Mn(acac)_3$, 1,2-hexadecanediol (2 mmol), oleic acid (1.2 mmol), and oleylamine (1.2 mmol) were mixed and dissolved in 20 ml benzyl ether. The mixed solution was heated to 290 °C with the heating rate of 5 °C/min. The temperature was kept at 290 °C for 30 min. Then the solution was naturally cooled to room temperature. The NPs were washed by ethanol

and redispersed in hexane for several times. The final product was stored in hexane.

3.2 Analyzing instruments

3.2.1 Vibrating sample magnetometer (VSM)

Vibrating sample magnetometer (VSM), first developed in 1956 by Simon Foner,[82] has become a widely used instrument for determining the magnetic properties of materials. The VSM setup is illustrated in Fig. 3.1. In this setup, the sample is attached to the end of a rod, centered in a pair of pick-up coils between the poles of electromagnets. The other end of rod is fixed to a mechanical vibrator, vibrates the rod and the sample simultaneously. A magnetic flux change is thus induced in the pick-up coils, and the coils pick up a voltage corresponding to the flux change according to Faraday Laws of magnetic induction. The pick-up voltage is proportional to the magnetization of the sample. The greater the magnetization, the greater the induced pick-up voltage is.

The pick-up voltage is detected using lock-in amplification. The applied magnetic field produced by the electromagnets is directly measured by using a Gauss probe. The various components are hooked to a computer interface, and the system can thus be controlled and monitored by a visual basic program. With calibration using a specimen of known saturation magnetization M_S, the value of the magnetization of the sample is extracted as a function of the applied magnetic field, called as a hysteresis loop. By measuring the hysteresis loops along both easy and hard axes of the sample using VSM, we can obtain a great deal of

information about the magnetic properties of the sample, including the coercivity field H_C and the saturation magnetization M_S.

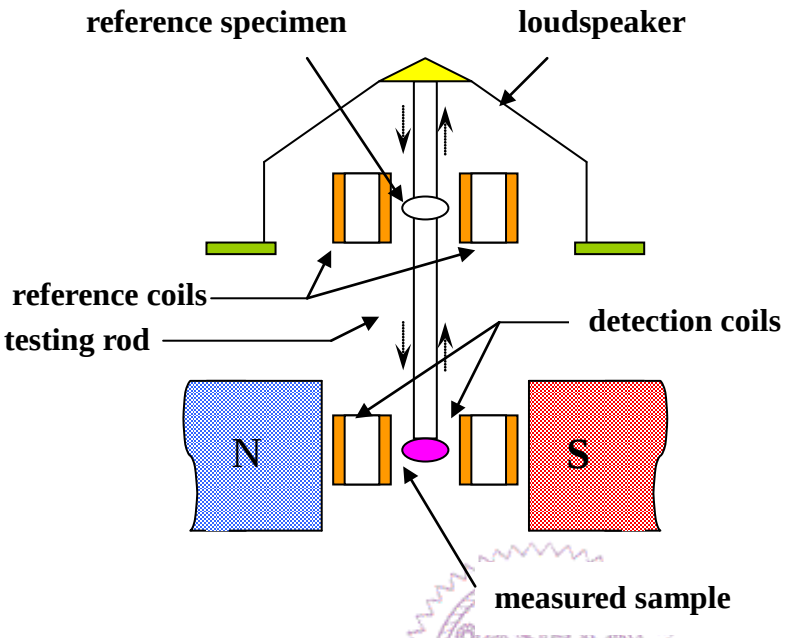

Fig. 3.1 A block diagram of the VSM setup. Vibration of a magnetic sample will induce a magnetic flux change in the pick-up coils, which will generate a voltage in the coils. The induced voltage is proportional to the magnetic moment of the sample.

3.2.2 X-ray diffraction (XRD)

The essential features of XRD instrument is shown in Figure 3.2. The rotating axis of specimen and detector are defined as θ and 2θ axis respectively. The detector can be rotated about sample and set at any desired angular position. The crystal is usually cut or cleaved so that a particular set of reflecting planes of known spacing is parallel to its surface, as suggested by the drawing. In use, the specimen is positioned so that its reflecting planes make some angle θ with the incident beam, and the detector is set at the corresponding angle 2θ. The intensity of the diffracted beam is then measured and its wavelength calculated from the Bragg law "$2d\sin\theta=n\lambda$", this procedure being repeated for various angles θ.

The directions in which a beam of given wavelength is diffracted by a given set of lattice planes are determined by the crystal system to which the crystal belongs and its lattice parameters. This is an important point and so is its converse: all we can possibly determine about an unknown crystal by measurements of the directions of diffracted beams are the shape and size of the unit cell. In addition, the intensities of diffracted beams are determined by the positions of atoms within the unit cell.

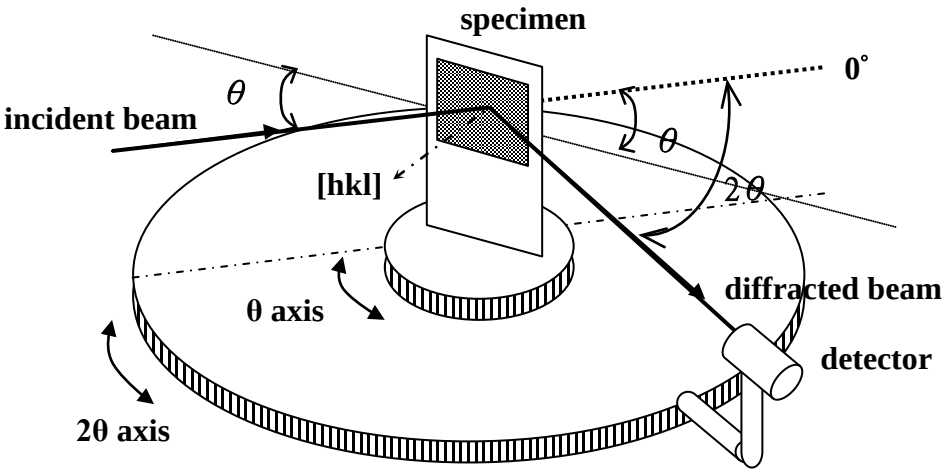

Fig. 3.2 Basic illustration of XRD spectrometer

3.3.3 Transmission electron microscope (TEM) and energy dispersive X-ray spectroscopy (EDS)

TEM has become an important tool in exploring nanomaterials. The complementary image, diffraction patterns, and high-resolution technique in TEM can provide the information of size, shape, and crystal structure of nanomaterials. The various interactions between electron beams and specimens can further provide the information of composition, electronic and/or magnetic state.

In our experiments, the TEM images are obtained by JEOL JEM-1400 operating at 120 kV, while the HRTEM images were obtained by JEOL JEM-2010F operating at 200 kV. The equipment can be divided into four parts: (1) the source of the electron beam, (2) the electromagnetic lens system. Several lens are indicated and driven by Lorentz force to focus electron beam, (3) specimen room, and (4) signal process system. On the bottom of TEM column is comprised of screen and some detector for energy analyzer. The layout of the basic TEM is shown in Fig. 3.3.

The energy dispersive X-ray spectroscopy (EDS) is an analytical technique used for the elemental analysis or chemical characterization of a sample. The incident electron beam excites an electron in the inner-shell and ejects it from the shell while creating an electron hole. An electron from an outer and higher-energy shell then relaxes into the inner-shell electron hole and releases a characteristic X-ray. As the energy of the X-rays is characteristic of the difference in energy between the two shells, and of the atomic structure of the element from which they were emitted, this allows the elemental composition of the specimen to be measured.

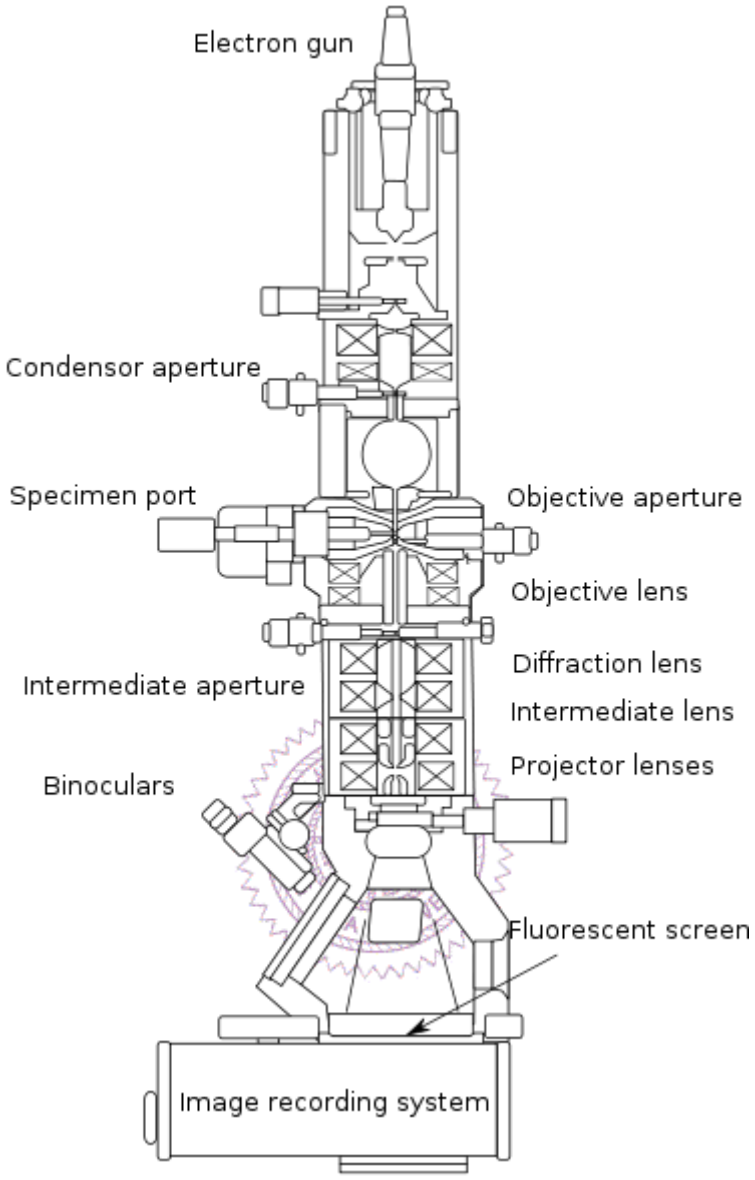

Fig. 3.3 Layout of optical components of a basic TEM. The figure is copied from http://en.wikipedia.org/wiki/Transmission_electron_microscopy.

3.3.4 X-ray photoemission spectroscopy (XPS)

X-ray photoemission spectroscopy (XPS) was developed by Kai Siegbahn starting in 1957[83-84] and is used to study the elemental composition, empirical formula, chemical state, and electronic state of the elements, primarily in solids. XPS spectra are obtained by irradiating a material with a beam of X-ray while simultaneously measuring the kinetic energy and number of electrons that escape from the top several nm of the material being analyzed (see in Fig. 3.4). Siegbahn referred to the technique as Electron Spectroscopy for Chemical Analysis (ESCA), since the core levels have small chemical shifts depending on the chemical environment of the atom which is ionized, allowing chemical structure to be determined.

Because the energy of a particular X-ray wavelength equals a known value, we can determine the electron binding energy of each of the emitted electrons by using an equation that is based on the work of Ernest Rutherford:

$$E_{binding} = E_{photon} - E_{kinetic} - \Phi \qquad \text{(equation 3.1)}$$

where $E_{binding}$ is the energy of the electron emitted from one electron configuration within the atom, E_{photon} is the energy of the X-ray photons being used, $E_{kinetic}$ is the kinetic energy of the emitted electron as measured by the instrument and Φ is the work function of the spectrometer (not the material).

In this investigation, the XPS measurements is performed by using synchrotron-based light source in NSRRC, Taiwan, since the synchrotron

radiation provides high-intensity light of well-defined characteristics with a continuous spectrum ranging from infrared to X-ray, which can benefit any research and development efforts using electromagnetic radiation. The samples are introduced in an UHV analysis chamber with the background pressure of 1-3 × 10^{-9} Torr to avoid the degradation (contamination) during analysis.

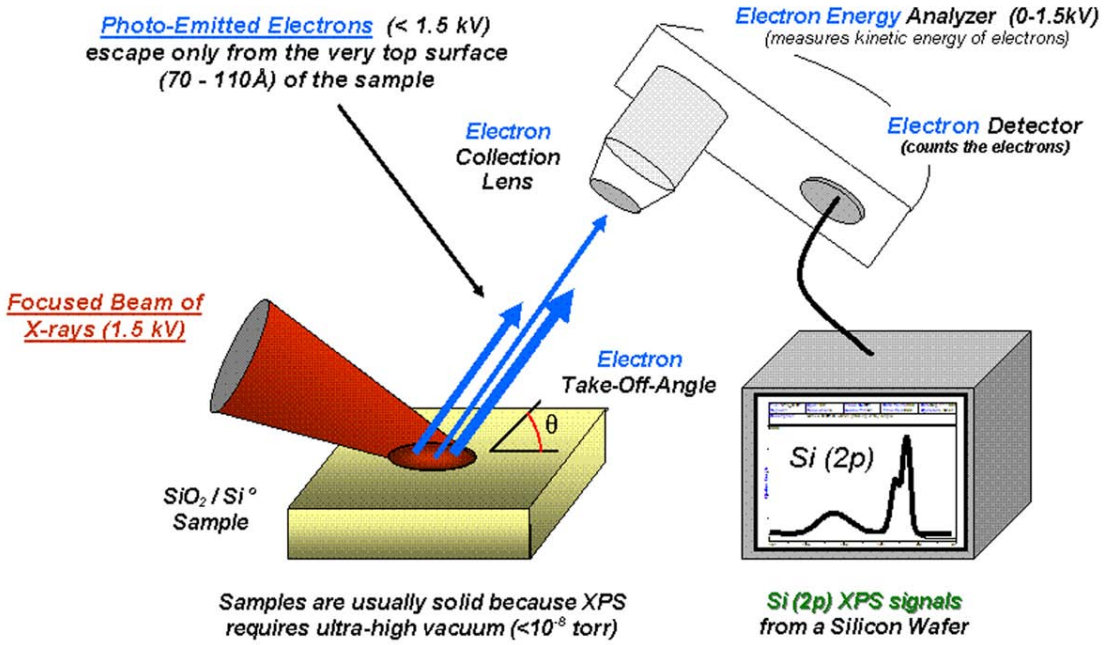

Fig. 3.4 Basic illustration of a monochromatic X-ray photoemission spectroscopy (XPS) system.

3.3.5 Inductively coupled plasma mass spectrometry (ICP-MS)

Inductively coupled plasma mass spectrometry (ICP-MS) is a type of mass spectrometry with high sensitivity to determine the elemental composition of a sample. It is composed of two parts including a inductively coupled plasma to ionize the sample and a mass spectrometry to separate and detect the ions.

A typical ICP-MS is able to detect in the rage of nanograms per liter to 10 or 100 micrograms per liter and allows determination of elements with atomic mass range from 7 to 250. However some masses are prohibited such as 40 due to the carrier gas of Ar. Other regions may include mass 80 due to the Ar dimer, and mass 56 due to the ArO. The mass 56 hinders the determination of Fe. Therefore, generally, the isotope of Fe 57 is used to detect the concentration of Fe.

3.3.6 X-ray Magnetic Circular Dichroism (XMCD)

X-ray Magnetic Circular Dichroism (XMCD) is considered to be one of the most important discoveries in the field of magnetism in the last two decades. It was first suggested by Erskine and Stern in 1975.[85] The first experiments with circularly polarized x-rays are performed in the high energy range by Schütz *et al*. in 1987.[86] The XMCD measurement has several capabilities that are not afforded by traditional magnetic analysis techniques. Its foremost strengths are the element-specific, quantitative determination of spin and orbital magnetic moments and their anisotropies.[87] Other strengths are the chemical sensitivity, the element-specific imaging capability, and its high sensitivity.[88-90]

In the XMCD measurement of transition metals, typically, *L-edge* X-ray spectrum was detected, which can best probe the properties of 3d electrons. As shown in Fig. 3.3,[90] the *L*-edge spectrum contains two main absorption peaks of L_3- and L_2-edges which are respectively associated with excitation of $2p_{3/2}$ and $2p_{1/2}$ core electrons to unfilled 3d states. The *L*-edge absorption spectra are characterized by strong absorption resonances, so-called white lines, near the L_3 and L_2 thresholds.[90] The sum of the L_3 and L_2 absorption intensities, denoted I_{L3} and I_{L2}, is proportional to the number of d holes related with the spin moments, as shown in Fig. 3.5. In addition, the spectrum detection affords the capability of element-specific measurement because the *L*-edge position depends strongly on atomic number.

The use of circularly polarized X-rays opens the door for X-ray-based spectroscopy studies of magnetic materials and structure. The basic concept of XMCD spectroscopy is easily understood if we assumed that the d shell has only a spin moment. To measure the difference in the number of d holes with up and down spins, we need to make the X-ray absorption process spin-dependent. Since spin flips are forbidden in electric dipole transitions, spin-up (spin-down) photoelectrons from the p core shell can only be excited into spin-up (spin-down) d hole states. Hence, if one could preferentially generate spin-up photoelectrons in one measurement and the spin-down in another, the difference of the transition intensity in the spectra would simply reflect the difference between up and down holes in the d shell. i.e. the spin moment. This is done by use of right or left circularly polarized photons which transfer their angular momentum to the excited photoelectrons and the difference between the spectra of right- and left-circularly-polarized X-ray is the XMCD spectrum.[91-92]

The XMCD effect is quantitatively related to the amounts of magnetic moments and to the anisotropies of the spin density and orbital moments.[90, 92-93] The maximum dichroism effect is observed if the photon spin direction and the magnetization directions are parallel or anti-parallel. When the photon spin and the magnetization directions are perpendicular, the resonance intensities at the L_3 and L_2-edges lie between those obtained for parallel and anti-parallel alignments. Thus, the size of the dichroism effect can be considered as a function of $\cos\theta$, where θ is the angle between the photon spin and the magnetization direction. The L_3 and L_2

resonance intensities and their differences for parallel and anti-parallel orientation of photon spin and magnetization directions are quantitatively related by sum rules to the number of d holes and the size of the spin and orbital magnetic moments.[90-91] Angular-dependence measurements in external magnetic fields give the anisotropies of the spin density and orbital moment.

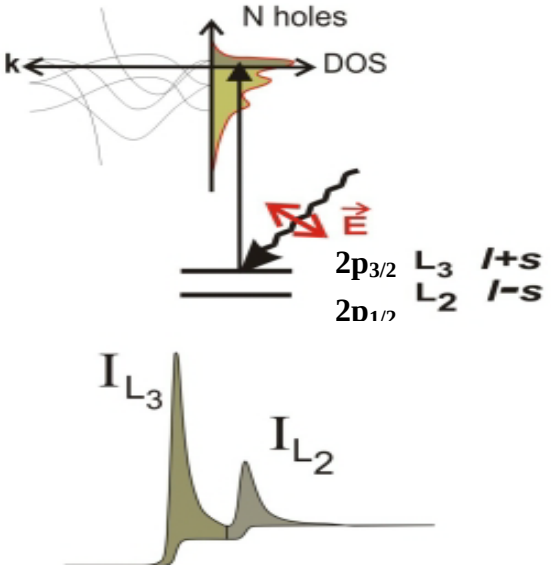

Fig. 3.5 Electronic transitions in conventional L-edge x-ray absorption.[90]

Chapter IV

Synthesis and Structure Characteristics of Shaped Fe_3O_4 Nanoparticles: From Cube to Rhombicuboctahedron

4.1 Introduction

Over the past years, uniform magnetic NPs with various sizes and compositions have been extensively synthesized and investigated.[18, 37-38, 52-53, 94] However, the investigations on shape control of magnetic NPs are relatively limited.[15-17, 44, 73, 95] The shape of magnetic NPs not only dominates magnetic shape anisotropy and surface anisotropy,[68] but makes NPs become good building blocks to self-assemble themselves into ordered superstructures, which can perform specific functionalities in biological systems or become an attractive candidate for ultrahigh-density magnetic pattern media.[18, 26, 95]

Fe_3O_4 NPs are widely investigated in biomedical applications due to their biocompatible properties and low toxicity. Interestingly, Fe_3O_4 nanocubes and cuboctahedrons have been largely found in nature from the magnetosomes in magnetotactic bacteria.[9-10] However, only recently the artificial Fe_3O_4 nanocubes were successfully synthesized by complicatedly tuning the capping surfactants.[15, 17, 44] Kovalenko *et al.* used the oleate salts as the surfactants to synthesize the Fe_3O_4 nanocubes

with a size range from 9 to 23 nm. Replacing oleic acid (OA) by its oleate salts can increase the concentration of “free” oleate ions in solution. Yang *et al.* synthesized the Fe_3O_4 nanocubes with a size range from 6 to 30 nm by increasing the amount of OA and reducing the amount of oleylamine. The carboxylic group, -COOH, of OA can selectively bind onto different crystal facets, and the nonpolar tail group in OA can provide steric hindrance. However, the $-NH_2$ group in oleylamine has a weak and isotropic binding onto the surface of particles. Kim *et al.* first reported the synthesis of larger Fe_3O_4 nanocubes with the size of 160 nm. In their experiments, no reductants and large amount of oleic acid were used. Although the above reports have successfully synthesized the Fe_3O_4 nanocubes, the formation mechanism, shape control, and even a new facile method for the synthesis of shaped Fe_3O_4 NPs still need to be further investigated.

In this chapter, we demonstrate a modified hot-injecting polyol process to control the shape of Fe_3O_4 NPs, in which the precursor is injected into the hot reaction solution with a slow injecting rate instead of instantaneous injection. The conventional heating-up polyol process is also performed for comparison. The modified hot-injecting method results in cubic Fe_3O_4 NPs, while the conventional heating-up method leads to spherical NPs. The early stages of Fe_3O_4 nanocube formation show that the formation of cubic Fe_3O_4 NPs has been triggered during the injection process, which indicates that injecting the precursor into the hot reaction slowly provides a proper growth condition for synthesizing cubic Fe_3O_4 NPs.

Several experimental parameters, including the precursor injecting

temperature, surfactant concentration, precursor concentration, and injecting rate, are varied to further investigate the formation mechanism of Fe_3O_4 nanocubes. The formation of Fe_3O_4 nanocubes strongly depends on the precursor injecting temperature. Cubic Fe_3O_4 NPs are obtained when the injecting temperature is 290 °C. However, if the injecting temperature is below 260 °C, the shape of Fe_3O_4 NPs becomes irregular or spherical. Unlike the reported synthesis of Fe_3O_4 nanocubes, high surfactant concentration seems not to play an assistant role in our method. When both oleic acid and oleylamine are 40 μL, Fe_3O_4 nanocubes can be synthesized. However, when the surfactants are both increased to 160 and 400 μL, the Fe_3O_4 NPs become smaller and spherical. It implies that the formation of cubic shape is not attributed to the surfactant effect. Interestingly, the rhombicuboctahedral Fe_3O_4 NPs are obtained after increasing the monomer concentration by adjusting the precursor concentration and injecting rate. The lower monomer concentration leads to cubic shape, while the higher monomer concentration results in rhombicuboctahedral shape. The shape formation mechanisms of cubic and rhombicuboctahedral Fe_3O_4 NPs are presented and discussed in this chapter. Furthermore, the shape-dependent oriented assembly is also observed and discussed.

4.2 Experimental section

4.2.1 Fe_3O_4 nanoparticles synthesized by the modified hot-injection and the conventional heating-up polyol processes

All NPs were synthesized by using polyol processes with standard Schlenk line techniques. The polyol reaction was shown in Fig. 4.1. In this study, a modified hot-injecting polyol process was used to synthesize the shaped NPs. The Fe precursor was injected into the benzyl ether solution at 290 °C, the boiling point of benzyl ether. Unlike the original hot-injecting method proposed by Murray *et al.*,[96] in which the precursor was injected into the hot solution instantaneously, we injected the precursor at a slow injecting rate. The similar method has also been used to synthesis the ZnSe nanocrystals of various morphologies, such as ZnSe nanorods and branched ZnSe nanocrystals.[97] The slow injection not only can avoid the temperature drop caused by the instantaneous injection, but can control the monomer concentration by regulating the injecting rate. On the other hand, the conventional heating-up polyol process was also carried out to compare with our modified hot-injecting method. In the heating-up process, the Fe precursor was mixed with the reaction solution at room temperature in advance. The mixed solution was then heated to the designed reaction temperature.

In the modified hot-injecting polyol process, oleic acid (40 μL), oleylamine (40 μL), and 1, 2-tetradecanediol (5 mmol) were dissolved in benzyl ether (15 mL) as the reaction solution, while $Fe(acac)_3$ (1 mmol) was dissolved in benzyl ether (5 mL) as the precursor solution with the concentration of 0.2 M. The reaction solution was dewatered at 120 °C

for 1h, followed by being heated to the reflux temperature of 290 °C at the heating rate of 10 °C/min. Then, the precursor solution was injected into the hot reaction solution at 290 °C with the injecting rate of 10 mL/h. The fluctuation of reaction temperature was less than 5 °C during the injecting process. After the injection was finished, the reaction solution was kept at 290 °C for 2 h. Finally, the NPs were washed by ethanol and redispersed in hexane for several times. The final product was stored in hexane.

In the conventional heating-up polyol process, $Fe(acac)_3$ (1 mmol), oleic acid (40 μL), oleylamine (40 μL), and 1,2-tetradecanediol (5 mmol) were dissolved in benzyl ether (20 mL) as the reaction solution at room temperature. The reaction solution was heated to the reflux temperature of 290 °C at the heating rate of 5 °C/min. The solution was also kept at 290 °C for 2h. After the reaction was finished, the NPs were washed by ethanol and redispersed in hexane for several times. The final product was stored in hexane.

In addition, the early stages of NP formation in the modified hot-injecting method were performed by taking 0.1 mL reaction solution from the reaction bottle at 5 min, 10 min, 15 min, 20 min, 30 min, 1h, 1.5 h, and 2 h after the precursor injection was triggered. Noteworthily, within the first 30 min, the precursor was still continuously injected into the reaction solution.

4.2.2 Fe_3O_4 nanoparticles synthesized by the modified hot-injecting method with varied experimental parameters

In order to investigate the formation mechanism of Fe_3O_4 NPs

synthesized by the modified hot-injecting method, several experimental parameters were varied, including **(A)** the precursor injecting temperature, **(B)** surfactant concentration, **(C)** precursor concentration, and **(D)** injecting rate. The precursor injecting temperature affects the thermal energy in solution which influences the nucleation and growth condition. In general, the sufficient thermal energy leads to fast reduction and nucleation which let most seeds become single-crystal.[69] The sufficient thermal energy also make the removal of high-energy planes become thermodynamically favorable.[72] The high surfactant concentration was used to synthesize the Fe_3O_4 nanocubes because some surfactants can bind to specific planes leading anisotropic growth.[15-17] However, in our modified method, only 40 μL of oleic acid and oleylamine were used, which are relatively small comparing to the reported synthesis. Therefore higher surfactant concentrations were carried out to investigate the role of surfactant in our method. In addition, both precursor concentrations and injecting rates can slightly adjust the monomer concentration in solution. Both higher precursor concentration and faster injecting rates reasonably cause the higher monomer concentration in solution. According to the La Mer theory, the monomer concentrations dominate the nucleation and growth process during the NP formation.[98]

Table 4.1 shows the adjusted experimental parameters and their conditions. Other experimental parameters are unchanged. Noteworthily, in experiment **(A)**, even the precursor is injected into the reaction solutions at 200, 230, and 260 °C, all reaction solutions are heated to 290 °C and kept for 2 h after the injection. The experimental setup of experiment **(A)** is shown in Scheme 4.1. Both **(A)** the precursor injecting

temperature and **(B)** surfactant concentration are presented and discussed in section 4.3.2, while **(C)** precursor concentration, and **(D)** injecting rate are shown in section 4.3.3.

4.2.4 Characterizations

Transmission electron microscope (TEM) images were obtained by JEOL JEM-1400 operating at 120 kV. The NPs were dispersed on the amorphous carbon-coated copper grids for TEM studies. X-ray diffraction (XRD) patterns were detected by Shimadzu XRD6000 using Cu Kα radiation. The XRD samples were prepared by dropping the NP dispersion on Si substrates with a controlled solvent evaporating rate. After the solvent was evaporated, the dried NPs on Si substrate were used for XRD measurement.

Table 4.1 The adjusted experimental parameters and their conditions of each experiment

	Experimental parameters	**Original condition**	**Adjusted Conditions**
(A)	Precursor injecting temperatures	290 °C	200, 230, and 260 °C
(B)	Surfactant concentrations (both oleic acid and oleylamine)	40 μL	80, 160, and 400 μL
(C)	Precursor concentrations	0.2 M	0.05, 0.1, and 0.3 M
(D)	Injecting rates	10 mL/h	2.5 and 20 mL/h

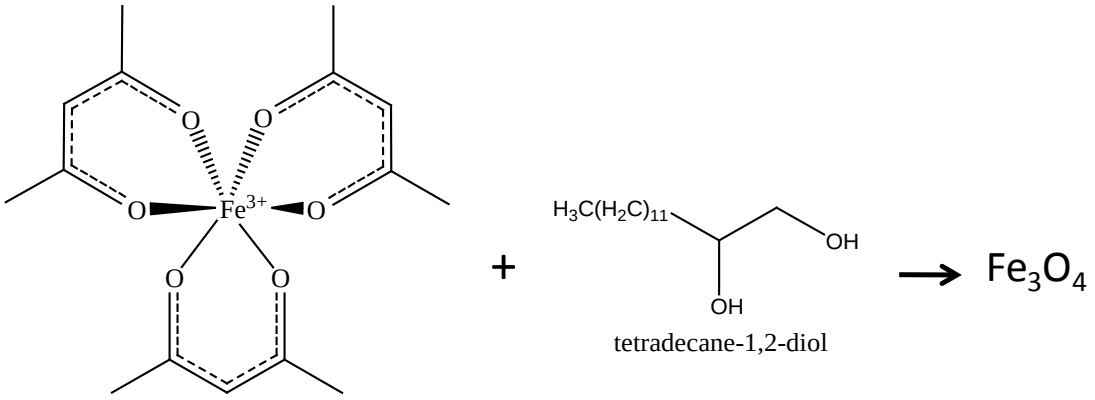

Iron(III) acetylacetonate, $Fe(acac)_3$

tetradecane-1,2-diol

Fig. 4.1 Polyol reaction of the synthesis of Fe_3O_4 NPs

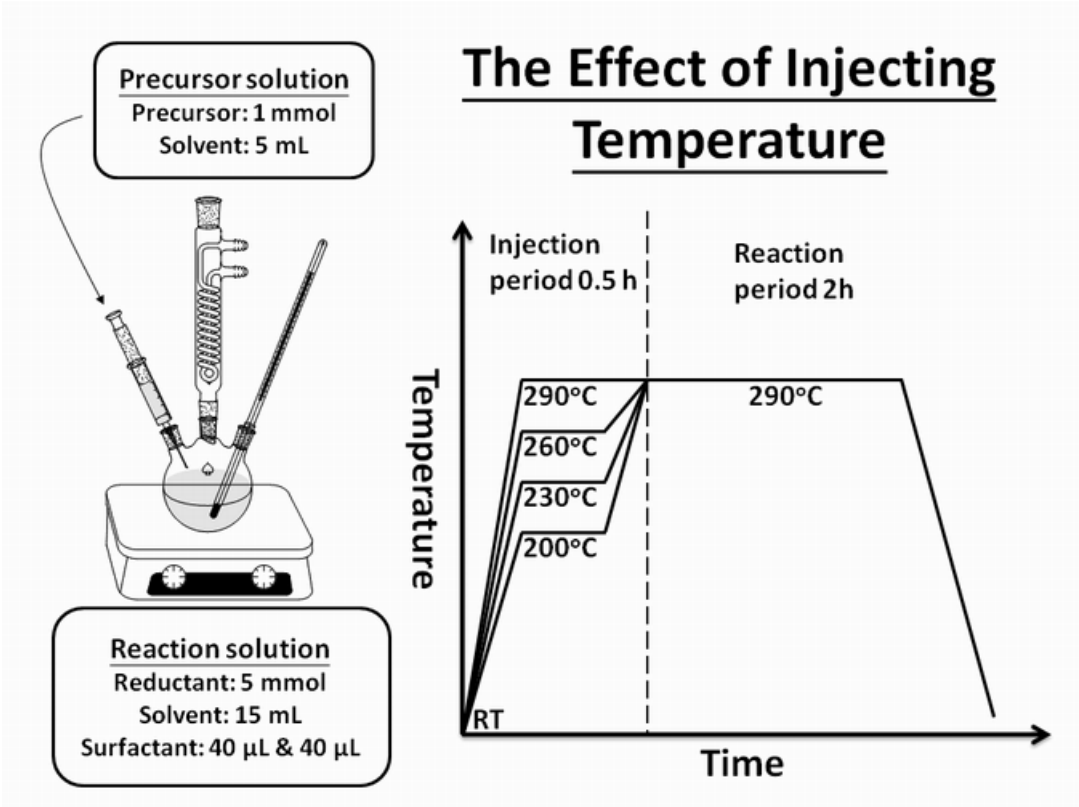

Scheme 4.1 The schematic diagram for the synthesis of Fe_3O_4 nanocrystals with various precursor injecting temperature.

4.3 Results and discussion

4.3.1 Fe_3O_4 nanoparticles synthesized by modified hot-injecting and conventional heating-up polyol processes

Fig. 4.2(a) and (b) show the TEM images of Fe_3O_4 NPs synthesized by modified hot-injecting and conventional heating-up polyol processes, respectively. The cubic NPs self-assembled into square packing array were synthesized by the modified hot-injecting polyol process. On the other hand, in the conventional heating-up polyol process, the spherical NPs assembled into hexagonal packing array were obtained. Noteworthily, the corresponding SAED pattern of cubic NPs with square array displays clear arced-spots instead of rings which indicate the formation of crystallographic orientation-ordered superlattices,[74] shown in Fig 4.2(c). The arced-spots with 4-fold symmetry are indexed as {220}, {400}, and {440} indicating that the electron beam is along the [001] crystallographic orientation of Fe_3O_4. The crystalline structure and facets of Fe_3O_4 nanocubes were verified by HRTEM image, shown in Fig. 4.3. It revealed that the nanocubes are high-quality single-crystalline, and the lattice fringes correspond to {220} lattice planes of Fe_3O_4 while the facet is {100}. The SAED pattern of spherical NPs displays diffraction rings which can be indexed as the {220}, {311}, {400}, {422}, {511}, and {440} planes of cubic spinel-structured Fe_3O_4, shown in Fig. 4.2(d). The ring pattern indicates that even the spherical NPs can be assembled into a hexagonal array, their crystallographic orientation is still random. The average edge length of Fe_3O_4 nanocubes is 16.1 $\pm$ 0.9 nm, while the spherical Fe_3O_4 NPs have smaller diameter of 6.5 $\pm$ 0.7 nm, shown in Fig.

4.2 (e) and (f), respectively. The size distributions indicate that the modified hot-injecting method results in narrower size distribution than the conventional heating-up method.

To investigate the shape evolution of Fe_3O_4 nanocube, the NPs were taking from the reaction solution at different duration time. Fig. 4.4 (a)-(g) show TEM images of the early stages of nanocubes formation through taking the NPs from the reaction solution at the duration time of (a) 5 min, (b) 10 min, (c) 20 min, (d) 30 min, (e) 1h, (f) 1.5 h, and (g) 2 h after the injection was triggered. And Fig. 4.4(h) is the size evolution of the different durations. The size evolution can be separated into two parts. First, the particle size was rapidly increased due to the continuous replenishment of monomers during the injection (within the first 30 min). After the injection (after 30 min), the slight particle growth should be attributed to the Ostwald ripening. Noteworthily, the cubic Fe_3O_4 NPs can be found before the injection was finished, which indicates injecting the precursor into the hot reaction solution slowly can trigger the formation of nanocubes. After the injection was finished, the residual and limited monomers still show selective growth leading to better nanocubes.

The formation processes of NPs through colloidal methods were proposed by La Mer and could be understood by the following three steps: (1) monomer formation, (2) nucleation, and (3) growth, shown in Fig. 4.5.[98-99] When the thermal energy or triggers, such as catalysts or reductants, are introduced into to the system, the monomer concentration steadily increases with time due to the reduction or decomposition of precursors. Once the monomer concentration is higher than the minimum threshold of nucleation, C^N_{min}, the monomers start to aggregate into small

cluster via homogeneous nucleation, and then the monomer concentration is reduced simultaneously. If the monomer concentration drops below the nucleation threshold, no additional nucleation events occur. Afterwards, the monomers tend to heterogeneously grow on the existing nuclei instead of homogeneous self-nucleation. On the other hand, if the monomer concentration is still higher than the nucleation threshold after nucleation occurs, the self-nucleation and growth will occur simultaneously. The competition between nucleation and growth causes the large variation in particle size. Hence, separating nucleation and growth in two distinct steps is an important factor to prepare monodisperse NPs.

The hot-injecting method was porposed by Murray *et al.* in the synthesis of CdX (X = S, Se, Te) NPs,[96] and was also employed to synthesize the CdSe nanorods.[67, 100] The cold Cd and Se precursors were rapidly injected into the hot solution at 300 °C. The monomer concentration reached the supersaturation limit, C^{N}_{max}, instaneously resulting in burst nucleation. During the nucleation, the solution temperature and monomer concentration were both quickly dropped, which prevented the new nulceation. Finally, when the thermal energy was added again, the monomers just grow on the existing nuclei without new nucleation. Even though the hot-injecting method can effectively separate the stages of nucleation and growth, the large drop in temperature may cause the reaction unstable. The modified hot-injecting method with slow injecting rate can not only solve the decrease in reaction temperature, but regulate the monomer concentration below the nucleation threshold after nucleation. Injecting precursor at high

temperature with controlled injecting rate has been used in the synthesis of ZnSe nanocrystals.[97] ZnSe nanorods were synthesized at the precursor injecting rate of 0.2 to 0.05 mL/min, while the branched ZnSe nanocrystals were obtained at the injecting rate of 0.4 to 0.3 mL/min. The energetic monomers of iron oxide decomposed from iron precursor at high temperature carried out a fast nucleation after the monomer concentration reached to the homogeneous nucleation threshold. After that, due to the continuous consumption on particle growth and the slow injecting rate of precursor, the monomer concentration was steadily below the nucleation threshold. Hence, the replenished monomers just implemented heterogeneous growth instead of homogeneous nucleation. For the conventional heating-up method, because Fe precuror was mixed with the reaction solution in advance at room temperature, lots of monomers formed when the solution temperature was higher than the precurosr decomposition temperature. The high monomer concnetration made the nucleation and grwoth occur simultaneously leading to larger variation in particle size. On the other hand, the high monomer concentration also led to more nuclei. The high nucleus concentration resulted in smaller particle size. Therefore, that is why the Fe_3O_4 NPs synthesized by the heating-up method are smaller than those syntheized by the modified hot-injecting method.

The mechanisms of controlling nanocrystals into different shapes and various terminated planes have been discussed.[69, 72, 99] In general, the highly crystalline nuclei and selective growth are two important requirements in shape control. Scheme 4.2 shows the schematic illustration of the proposed formation mechanisms of cubic Fe_3O_4 NPs

synthesized by the modified hot-injecting method. The modified hot-injecting method can provide more sufficient thermal energy than the conventional heating-up method during the nucleation and growth stages. When the thermal energy is sufficient during the synthesis, the removal of high-energy planes becomes thermodynamically favorable.[72] On the other hand, the limited monomers caused by a slow injecting rate preferentially grew on the planes with higher surface energy leading to selective growth. Consequently, the planes with the lowest surface energy became the terminated planes. Fe_3O_4 nanocubes terminated at {100} planes, which were predicted to possess the lowest surface energy in spinel oxides with cubic crystallographic symmetry, shown in Table 4.2.[101] After the cubic shape was formed, each {100} facet of Fe_3O_4 nanocubes had the same growth rate due to their equal surface energy. Thus, further growth mainly increased the nanocube size without changing their shapes.

The XRD patterns were detected to further investigate cubic spinel structure and preferential orientation of Fe_3O_4 nanocube assembly on Si substrate. It was reported that non-spherical shape of NPs can induce the texture of NP assembly.[73] Zeng *et al.* has found that the assembly of $MnFe_2O_4$ nanocubes showed (100) texture, while the (110) texture was obtained from the assembly of $MnFe_2O_4$ polyhedrons.[73] Because Fe_3O_4 has the same cubic spinel structure as $MnFe_2O_4$, the (100) texture of Fe_3O_4 nanocube assembly is expectably obtained. In addition, the formation of textured assembly is strongly affected by the procedure of sample preparation on Si substrates. The controlled slow solvent evaporating rate is crucial to form the textured arrays. Thus, in our experiments, the textured and non-textured NP assemblies were prepared

through controlling the solvent evaporating rate of NP dispersion on Si substrates. We define that the slow evaporating rate means the solvent is totally evaporated beyond 30 minutes, while the fast evaporating means the solvent is evaporated within 5 minutes. Fig. 4.6(a) and (b) show the XRD patterns of cubic Fe_3O_4 NP assemblies prepared with the fast and slow evaporating rates, respectively. The pattern detected from the sample prepared with the fast evaporating rate reveals the typical pattern of randomly orientated Fe_3O_4 powders, in which the strongest peak is Fe_3O_4(311). However, when the evaporating rate of solvent is slow, the nanocube assembly only shows Fe_3O_4(400) peak, which indicates the Fe_3O_4 nanocube assembly on Si substrate has (100) texture. The XRD results indicate that if the solvent evaporating rate is slow, the faceted planes of nanocubes are preferentially parallel to the Si substrate. Therefore, the XRD pattern can be used as an indicator to verify the formation of Fe_3O_4 nanocubes.

In summary, the Fe_3O_4 NPs synthesized by modified hot-injecting and conventional heating-up polyol process were investigated. The cubic Fe_3O_4 NPs with the terminated planes of Fe_3O_4{100} can be synthesized by the modified hot-injecting polyol process. The shape formation of Fe_3O_4 nanocubes should be attributed to the limited and energetic monomer concentration. Fe_3O_4 nanocubes can be self-assembled into square packing array with oriented crystallographic orientation on TEM grid. The formation of textured assembly on Si substrate was also demonstrated, in which the faceted planes were preferentially parallel to the Si substrate. On the other hand, the Fe_3O_4 NPs synthesized by conventional heating-up polyol process just show spherical shape. No

crystallographic oriented and textured assemblies were found on TEM grid and on Si substrate.

Minimum surface energies for the {100}, {110} and {111} surface of spinel

Surface	**Unrelaxed surface energy/ J m^{-2}**	**Relaxed surface energy/ J m^{-2}**
{100}	3.81	2.28
{110}	5.25	2.50
{111}	7.08	2.60

Table 4.2 the surface energy of {100}, {110}, and {111} planes of spinel structured materials.[102]

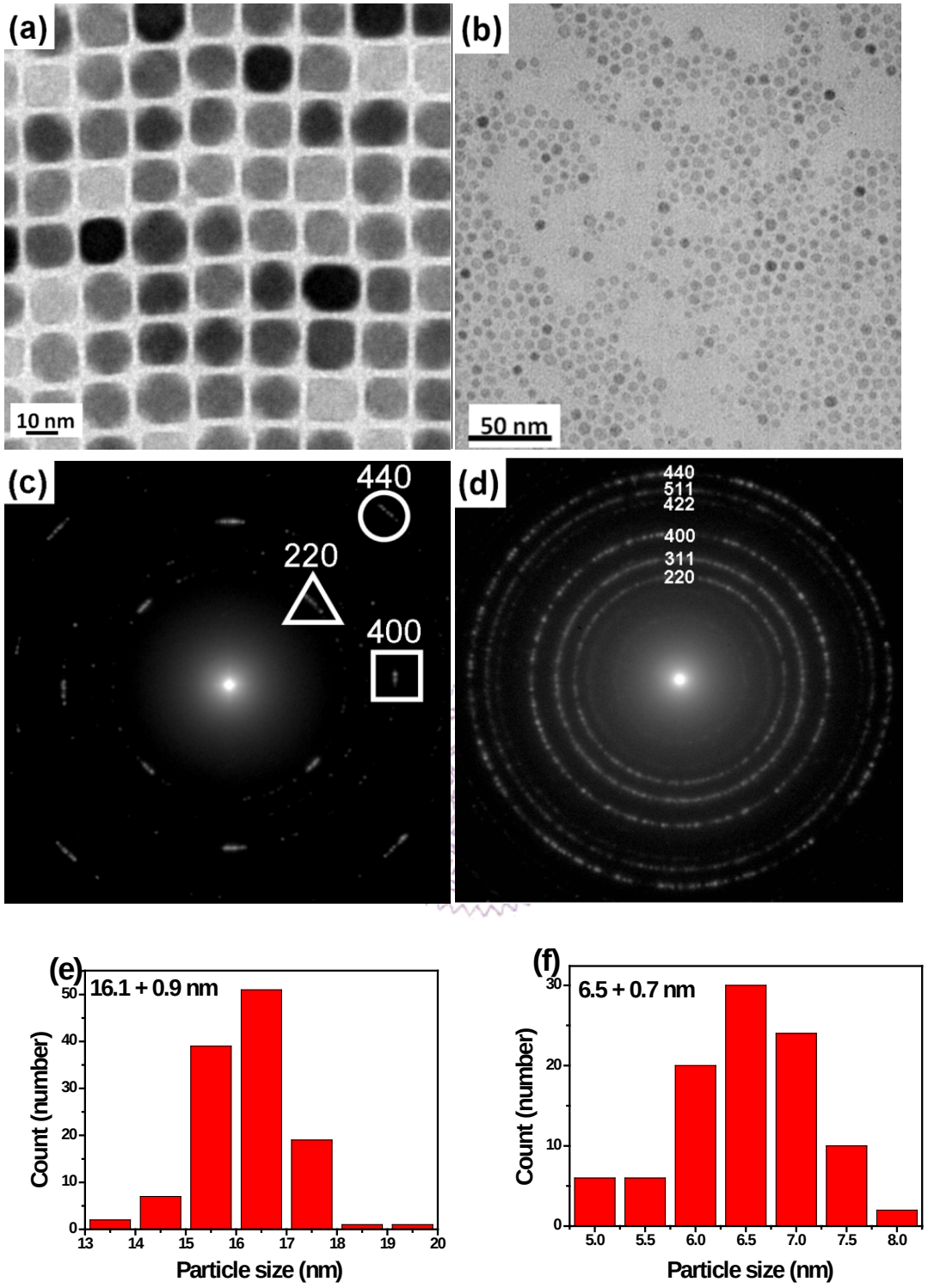

Fig. 4.2 TEM images of (a) cubic and (b) spherical Fe_3O_4 NPs. (c) and (d) are the corresponding SAED patterns of (a) and (b), respectively. (e) and (f) are the size distributions of (a) cubic and (b) spherical Fe_3O_4 NPs, respectively.

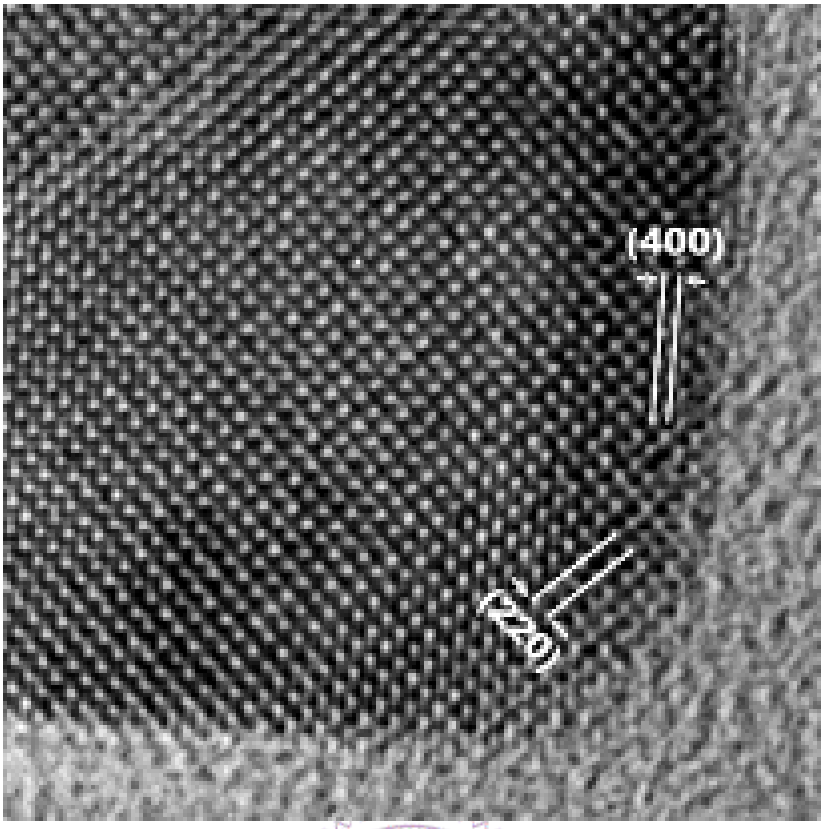

Fig. 4.3 HRTEM image of Fe_3O_4 nanocube

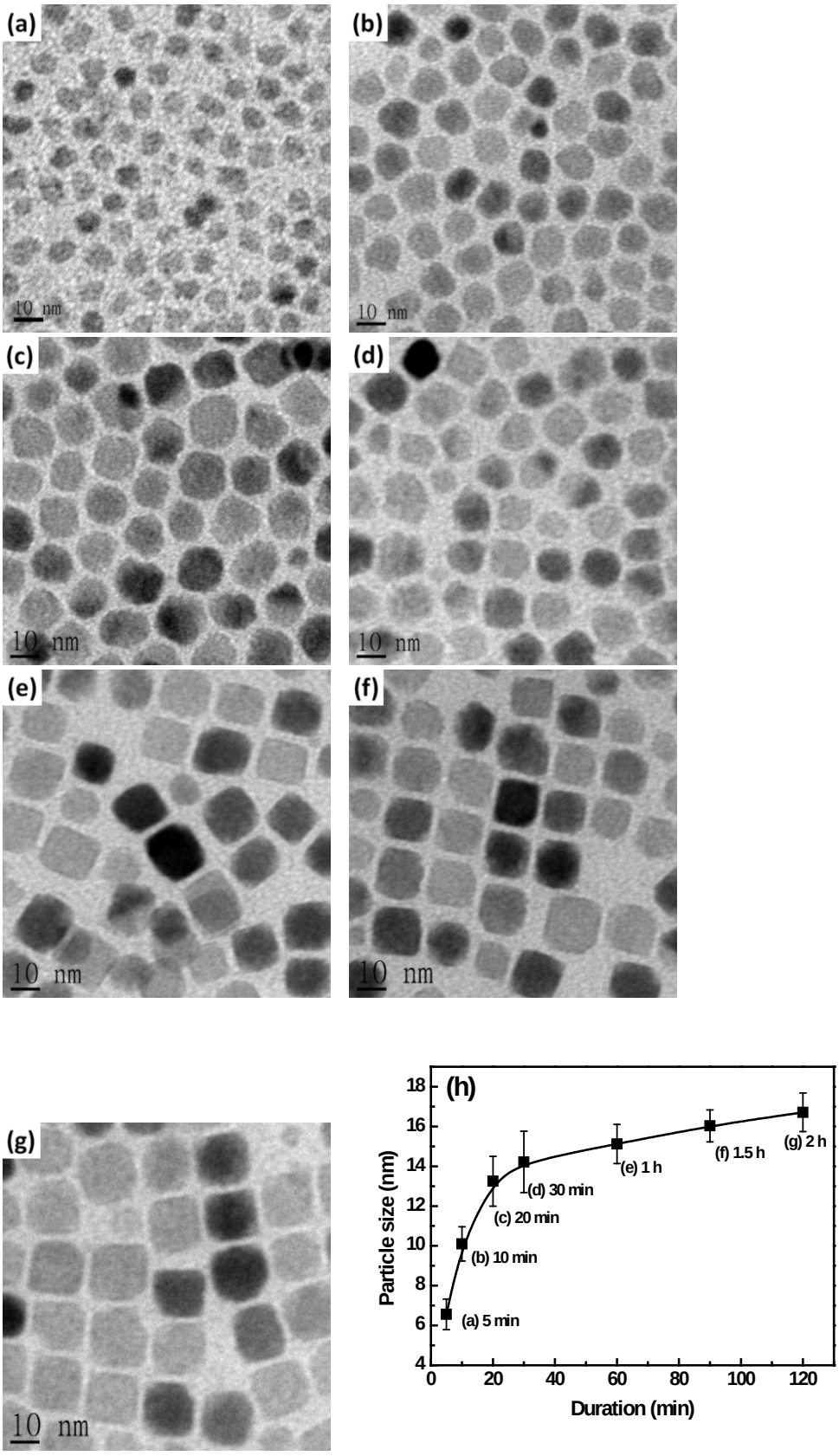

Fig. 4.4 The TEM images of Fe_3O_4 NPs in early stages. The NPs were taking from the reaction solution at (a) 5min, (b) 10 min, (c) 15 min, (d) 20 min, (e) 30 min, (f) 1h, (g) 1.5 h, and (h) 2 h after the injection was triggered.

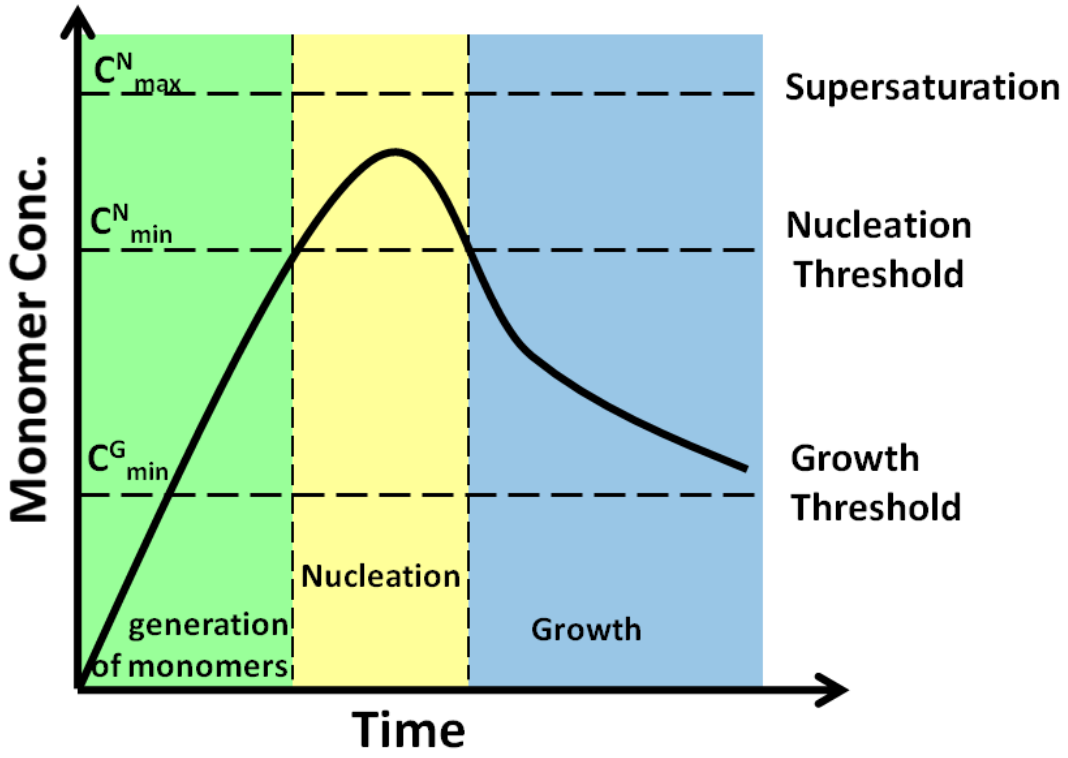

Fig. 4.5 Plot of monomer concentration against time, illustrating the generation of monomers, nucleation, and growth.

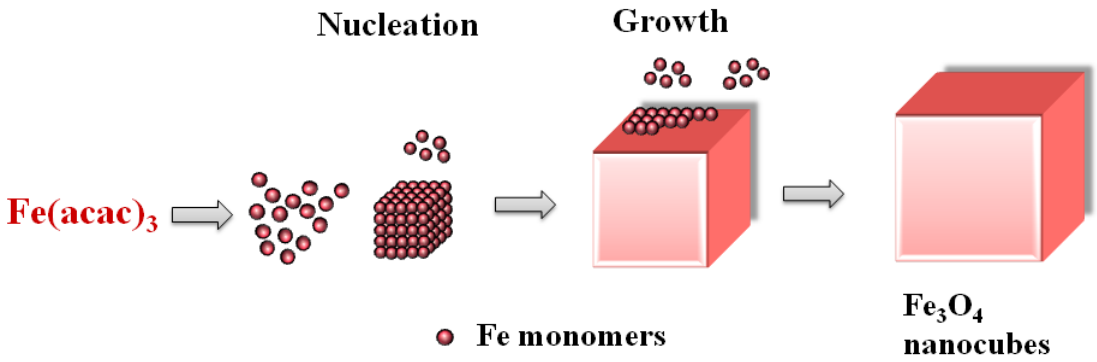

Scheme 4.2 Schematic representation of proposed growth mechanisms of Fe_3O nanocubes

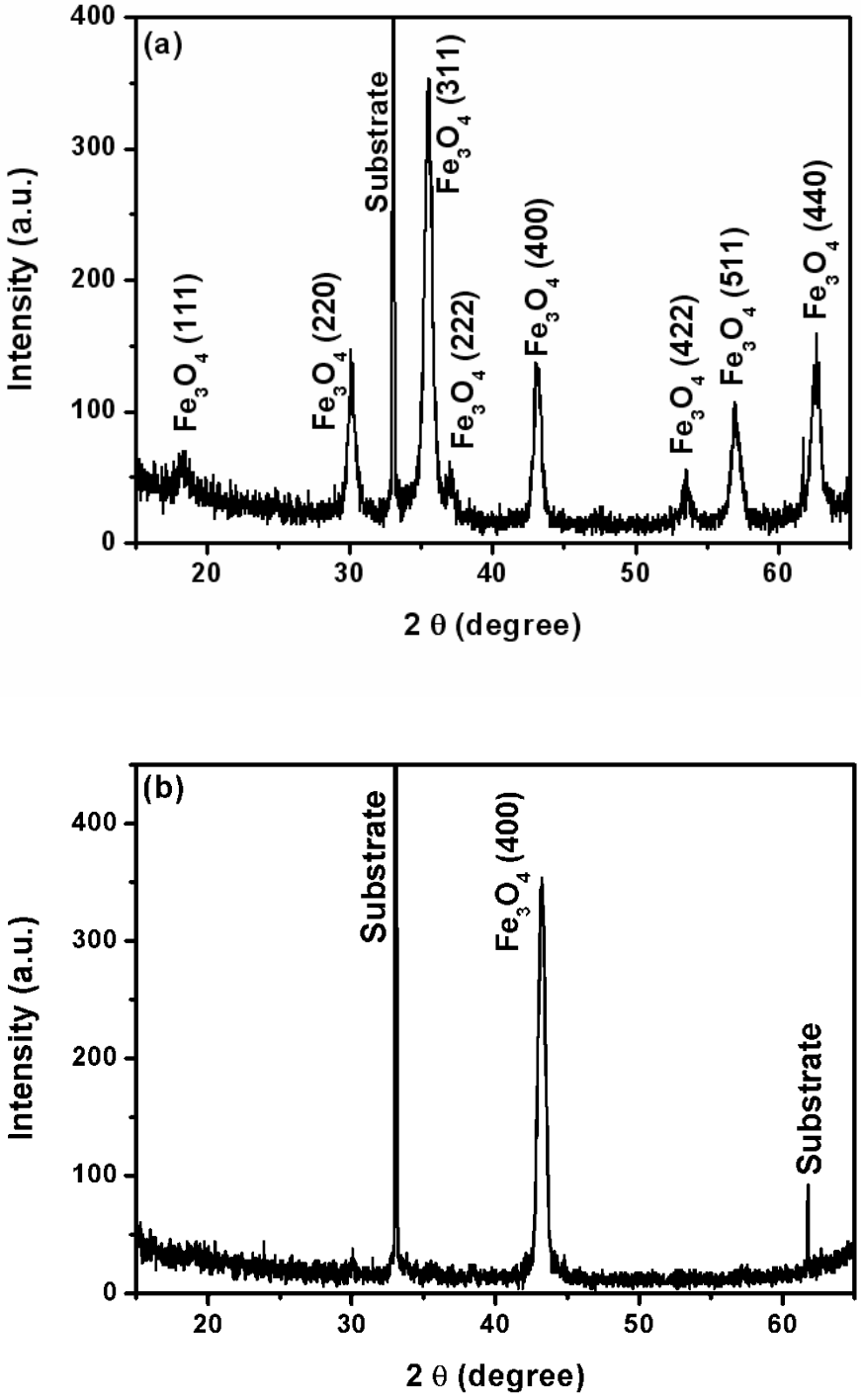

Fig. 4.6 The XRD patterns of Fe_3O_4 nanocubes prepared on Si substrate with (a) fast solvent evaporating rate and (b) slow solvent evaporating rate.

4.3.2 The effects of precursor injecting temperatures and surfactant concentrations on the synthesis of Fe_3O_4 nanocubes

In the previous section, Fe_3O_4 nanocubes were successfully synthesized by the modified hot-injecting method, in which the Fe precursor was injected into reaction solution at 290 °C with a slow injecting rate of 10mL/h. To investigate the effect of injecting temperatures, various lower injecting temperatures, including 260 °C, 230 °C, and 200 °C, were performed. Fig. 4.7 (a), (b), and (c) show the TEM images of Fe_3O_4 NPs synthesized with the lower injecting temperatures of 260 °C, 230 °C, and 200 °C, respectively. As the injecting temperature was decreased, the shape of Fe_3O_4 NPs changed from cubic to irregular and finally to almost spherical. The irregular and almost spherical shape may because the lower injecting temperature can not provide sufficient thermal energy, the removal of the high energy planes becomes unobvious. On the other hand, the average size was reduced simultaneously. The decrease in the particle size with the lower injecting temperature can be attributed to the slower growth rate and decreased chances for the particle coalescence at lower temperature. The corresponding XRD patterns of Fe_3O_4 NPs synthesized with lower injecting temperatures were shown in Fig. 4.7 (d). XRD samples were prepared by depositing the NP dispersions on Si substrate with a slow solvent evaporating rate. All patterns show the typical pattern of randomly oriented Fe_3O_4 powders indicating the NP assemblies should be un-textured. The un-textured NP assemblies were attributed to the irregular and spherical shapes of Fe_3O_4 NPs. Hence it is clear that the high precursor injecting temperature of 290 °C is crucial for the synthesis of cubic Fe_3O_4 nanocubes.

On the other hand, the synthesis of Fe_3O_4 nanocubes by adjusting the surfactant system has also been reported.[15-17, 103] The surfactant effect in the modified hot-injecting method was also investigated. Oleic acid and oleylamine are commonly used surfactants in synthesizing the NPs of Fe metals, Fe oxides, and Fe alloys.[18] The carboxyl functional group of oleic acid can chelate with Fe ion and form a chelate complex, while the amine functional group of oleylamine can coordinate with Fe ion, shown in Fig. 4.8. In the modified hot-injecting method, only 40 μL oleic acid and 40 μL oleylamine were used. The surfactant concentrations are significantly lower than the reported Fe_3O_4 nanocubes by using surfactant effects.[15-17, 103] Therefore, both the concentrations of oleic acid and oleylamine were increased to investigate the surfactant effect. Fig. 4.9 (a), (b), and (c) show the TEM images of Fe_3O_4 NPs synthesized with surfactant concentrations of (a) 80 μL, (b) 160 μL, and (c) 400 μL, respectively. The further increase of the surfactant concentration leads to the size reduction. The decreased size may result from the restricted growth conditions due to the high surfactant concentration. The shape was changed from cubic to almost spherical as the surfactant concentration was increased. When the surfactant concentration was 80 μL, cubic Fe_3O_4 nanocrystals could still be obtained. However, when the surfactant concentrations became 160 and 400 μL, the cubic nanocrystals were rarely found. The XRD patterns also revealed the shape change of Fe_3O_4 nanocrystals, shown in Fig. 4.9(d). The XRD patterns of cubic Fe_3O_4 NPs synthesized with low surfactant concentration of 80 μL show the strongest Fe_3O_4 (400) peak, while the smaller and almost spherical NPs

synthesized with high surfactant concentration show the typical pattern of randomly oriented Fe_3O_4 powders. From the above results, it seems that the surfactant effect does not play an important role in the synthesis of Fe_3O_4 nanocubes in the modified hot-injecting method.

In the general concept of shape control, various surfactants can bind to specific planes of NPs to reduce the growth rate and surface energy of the bound planes, leading to anisotropic growth. Hence, the terminated planes of NPs could be changed by adjusting specific surfactants. However, because the amounts of surfactants used in our experiments are limited. Therefore, the surface energy of distinct planes should be referred to their intrinsic surface energies. In the spinel oxide, the {100} planes have the lowest surface energy. So, the nanocubes with the terminated {100} planes formed. Even though the amounts of surfactants were increased to 400 μL, they were still limited comparing to the reported synthesis. In addition, the high injecting temperature also weakens the binding between surfactant and NP. The increased surfactants are not sufficient to dominate the selective growth, but just disturb the intrinsic surface energy of distinct planes due to the binding between them. Therefore, the surfactant effect is not the main reason for the formation of cubic Fe_3O_4 NPs. We can conclude that the formation of Fe_3O_4 nanocubes was attributed to the selective growth caused by the limited and energetic monomer concentration due to the modified hot-injecting method, not by the surfactant effect.

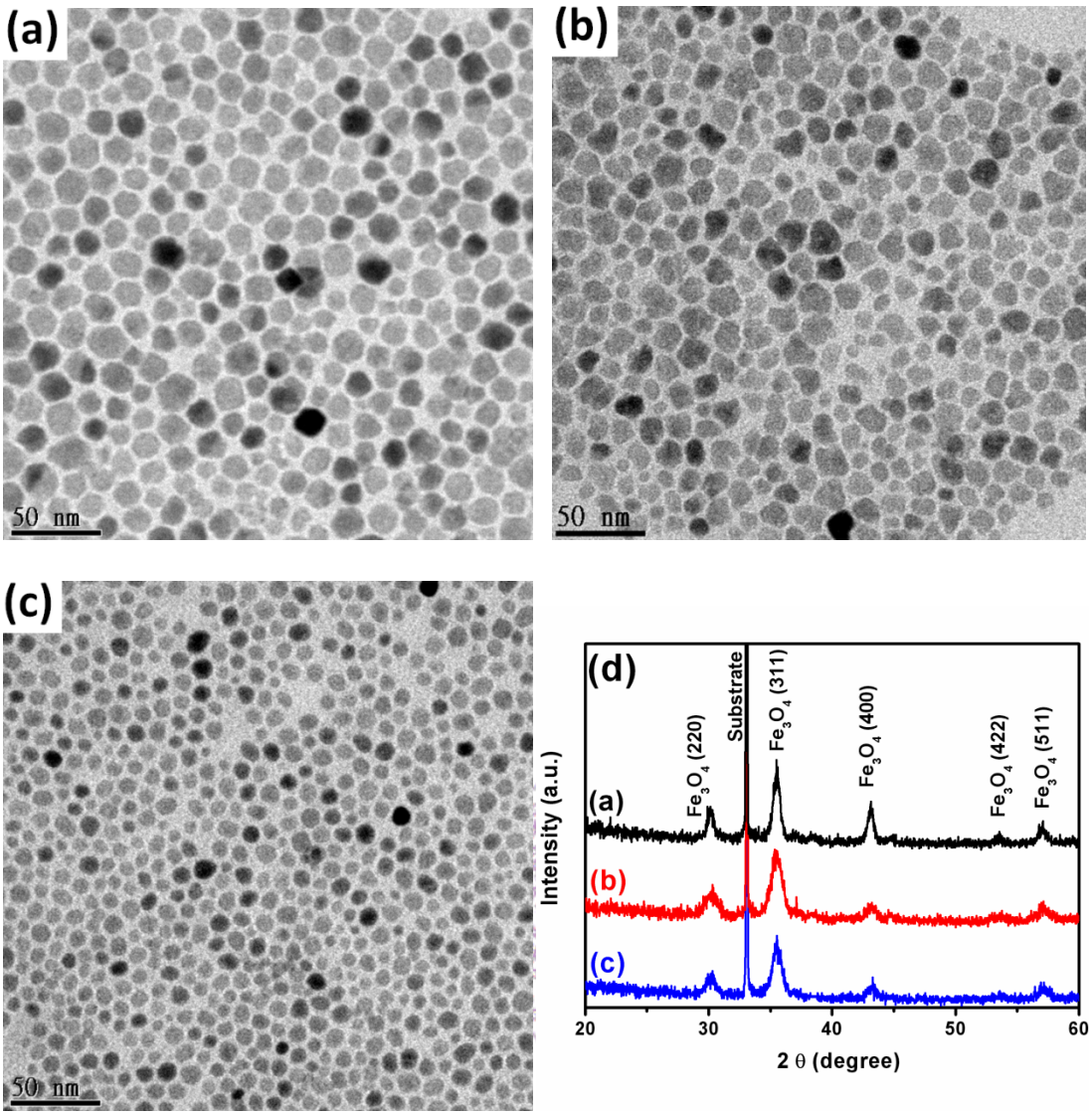

Fig. 4.7 TEM images of Fe_3O_4 NPs synthesized with the injecting temperatures of (a) 260°C, (b) 230°C, and (c) 200°C. The XRD patterns of each sample were shown in (d).

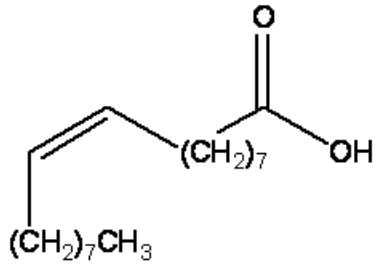

oleic acid

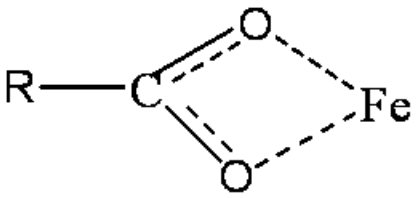

Chelation

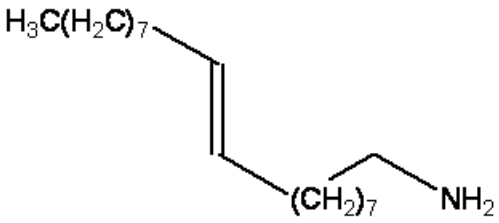

Oleyl amine

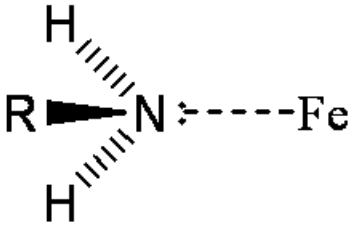

Coordination

Fig.4.8 The molecular formulas of oleic acid and oleylamine, chelation of carboxyl functional group, and coordination of amine functional group.

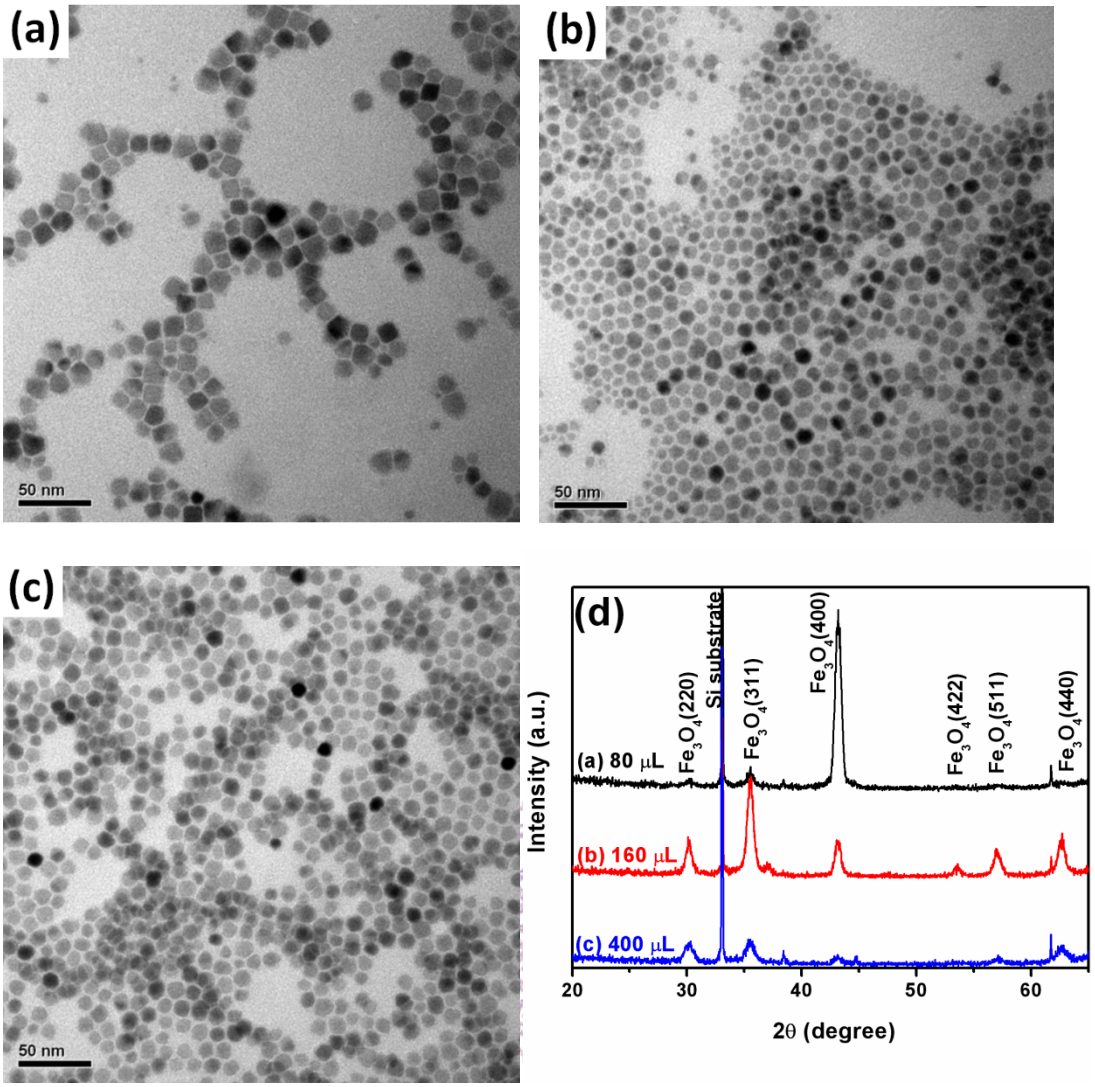

Fig. 4.9 TEM images of F_3O_4 NPs synthesized with the surfactant concentration of (a) 80 μL, (b) 160 μL and (c) 400 μL.

4.3.3 The monomer concentration effect: shape changed from cubic to rhombicuboctahedral

According to the above shape formation mechanism, the limited and energetic monomers preferentially grew on the planes with higher surface energy leading to selective growth. Presumably, if the monomer concentration become higher but still below the nucleation threshold, the excess monomers may grow on the other planes with the lower surface energy. Thus, the monomer concentration can reasonably influence the selective growth. The slow injecting rate is the unique feature of the modified hot-injecting method, which can result in slow replenishment of the monomers in solution. Therefore, when the monomer concentration was first higher than the threshold leading to the nucleation, the slow injecting rate can make the subsequent monomer concentration constantly below the nucleation threshold after the nucleation occurs. In this section, various monomer concentration changed by adjusting the precursor concentration and the injecting rate of precursor were investigated. The relationship between monomer concentration and selective growth was discussed.

Fig. 4.10(a), (b) and (d) show the TEM images of Fe_3O_4 NPs synthesized with precursor concentrations of 0.05 M, 0.1 M and 0.3 M, respectively, while in the original synthesis, the concentration of 0.2 M was used. Interestingly, from the TEM images, these samples can be classified into two groups according to their precursor concentrations. Noteworthily, cubic NPs can be observed in the samples prepared with lower precursor concentrations of 0.05 and 0.1 M, even the size was decreased to 9 nm. However, for the NPs prepared with higher precursor

concentration of 0.3 M, the shape changed from cubic to polyhedral, while the size was only slightly enlarged. The polyhedral Fe_3O_4 nanocrystals were self-assembled in quasi-hexagonal packing array, which was similar to what observed in the spherical Fe_3O_4 NPs. But, the corresponding SAED pattern of the quasi-hexagonal packing array displays arced-spots instead of continuous rings, shown in Fig. 4.10 (d). These arced-spots with 2-fold symmetry are indexed as {111}, {220}, {311}, {400}, and {440}. This arced-spot pattern is consistent with the simulated pattern with the zone axis of Fe_3O_4 [110] created by CaRIne Crystallography, shown in Fig. 4.10 (e). Thus, it can be deduced that the arced-spot pattern corresponds to the zone axis of Fe_3O_4 [110]. In addition, both cubic and polyhedral NPs display the texture-like assemblies in XRD pattern, shown in Fig. 4.10 (f). The assemblies of cubic Fe_3O_4 NPs, which were synthesized with the precursor concentration of 0.05 and 0.1 M, display the strongest Fe_3O_4 (400) peaks. However, in the XRD pattern of polyhedral NPs, which were synthesized with the precursor concentration of 0.3 M, both (220) and (440) peaks became considerable compared with (400) peak. The result indicated that both {110} and {100} planes of polyhedral Fe_3O_4 NPs were preferentially parallel to Si substrate, which implied {110} and {100} planes were the major faceted planes of the polyhedral NPs.

Adjusting the precursor injecting rate is another way to control the monomer concentration in reacting solution. Fig.4.11 (a) and (b) show the TEM images of Fe_3O_4 NPs synthesized with the injecting rates of 2.5 mL/h and 20 mL/h, respectively. The injecting rate of 10 mL/h was used in the original synthesis. The slower injecting rate of 2.5 mL/h, which

results in low monomer concentration, leads to smaller but still cubic Fe_3O_4 NPs, while the faster injecting rate of 20 mL/h leads to polyhedral Fe_3O_4 NPs. The changes in size and shape caused by various injecting rate are similar to those caused by adjusting the precursor concentration. Interestingly, when the NP concentration on TEM grid is slightly higher, the polyhedral NPs showed the multilayer ordered superlattices, shown in Fig. 4.11(b), and its corresponding SAED pattern of Fig. 4.11(b) displays the 6-fold symmetric arced-spots which can be indexed as {220}, {311}, {400}, {422}, {511}, and {440}, shown in Fig. 4.11(c). Typically, the 6-fold symmetric SAED pattern usually corresponded to the pattern with {111} zone axis. However, only {220}, {422}, and {440} diffraction spots can be observed on the {111} zone axis. So, the 6-fold symmetric pattern should result from the combination of three diffraction patterns with the identical zone axis of Fe_3O_4 [110], which may be due to the specific packing arrangement of multilayer superlattices. The HRTEM image (Fig. 4.11(d)) reveals that the 2D projection of polyhedral Fe_3O_4 NP is hexagonal when the sample is on the zone axis of Fe_3O_4 [111]. Finally, the XRD patterns, shown in Fig. 4.11(e), also confirm the change in preferential crystallographic orientation caused by the shape of Fe_3O_4 NPs. The Fe_3O_4 (400) peak was strongest in the cubic NPs synthesized with slow injecting rates of 2.5 mL/h, However, the peak intensities of (220) and (440) became even more intensive than that of (400) for the polyhedral NPs synthesized with fast injecting rates of 20 mL/h.

The real shape and the formation mechanism of polyhedral Fe_3O_4 NPs are still unsolved problems in the system. Here we proposed the possible mechanism to explain the shape of these polyhedral Fe_3O_4 NPs, shown in

Scheme 4.3(a). The reported surface energies of {100}, {110}, and{111} planes of spinel structured materials was shown in Table 4.2.[102] The growth rate of {100} planes is slowest due to its lowest surface energy in spinel structure. Hence, when the Fe monomers concentration is low, the limited Fe monomers preferentially grow on other planes with higher surface energy, such as {111} and {110}, leading to the formation of nanocubes with the terminated {100} planes. However, when the monomer concentration became higher, the relative growth rates in distinct planes were changed. The growth along {100} planes caused the surface area of {100} planes shrink leading to the appearance of other planes. The {110} planes which have the second lowest surface energy may become the other major faceted planes. Hence, the polyhedral NPs were principally terminated at {100} and {110} planes, which was also consistent with what we observed in XRD pattern of polyhedral NP assembly. According to the surface energy of each plane and the XRD pattern, it can be presumed that the shape of polyhedral NPs should be rhombicuboctahedron which is an Archimedean solid with 8 triangular and 18 square faces, shown in Fig. 4.12. When Fe_3O_4 NPs were deposited on Si substrates with a slow solvent evaporating rate, the terminated faceted planes are preferentially parallel to the Si substrate inducing the preferential crystallographic orientation. Hence, when the {110} planes became the other major terminated planes, the (110) planes also tend to parallel the Si substrate inducing intensive Fe_3O_4 (220) peak in the XRD pattern, shown in Scheme 4.3(b). The pictorial drawing, development drawing, and perspective views were shown in Fig 4.12. Interestingly, the perspective view from <111> direction shows the hexagonal shape which

coincides with the shape observed from HRTEM image on the {111} zone axis, shown in Fig. 4.11(d).

Herein, by adjusting the precursor concentration and precursor injecting rate, we have demonstrated that adjusting the monomer concentration can further control the shape of Fe_3O_4 NPs. The shape of polyhedral Fe_3O_4 NPs should be rhombicuboctahedral.

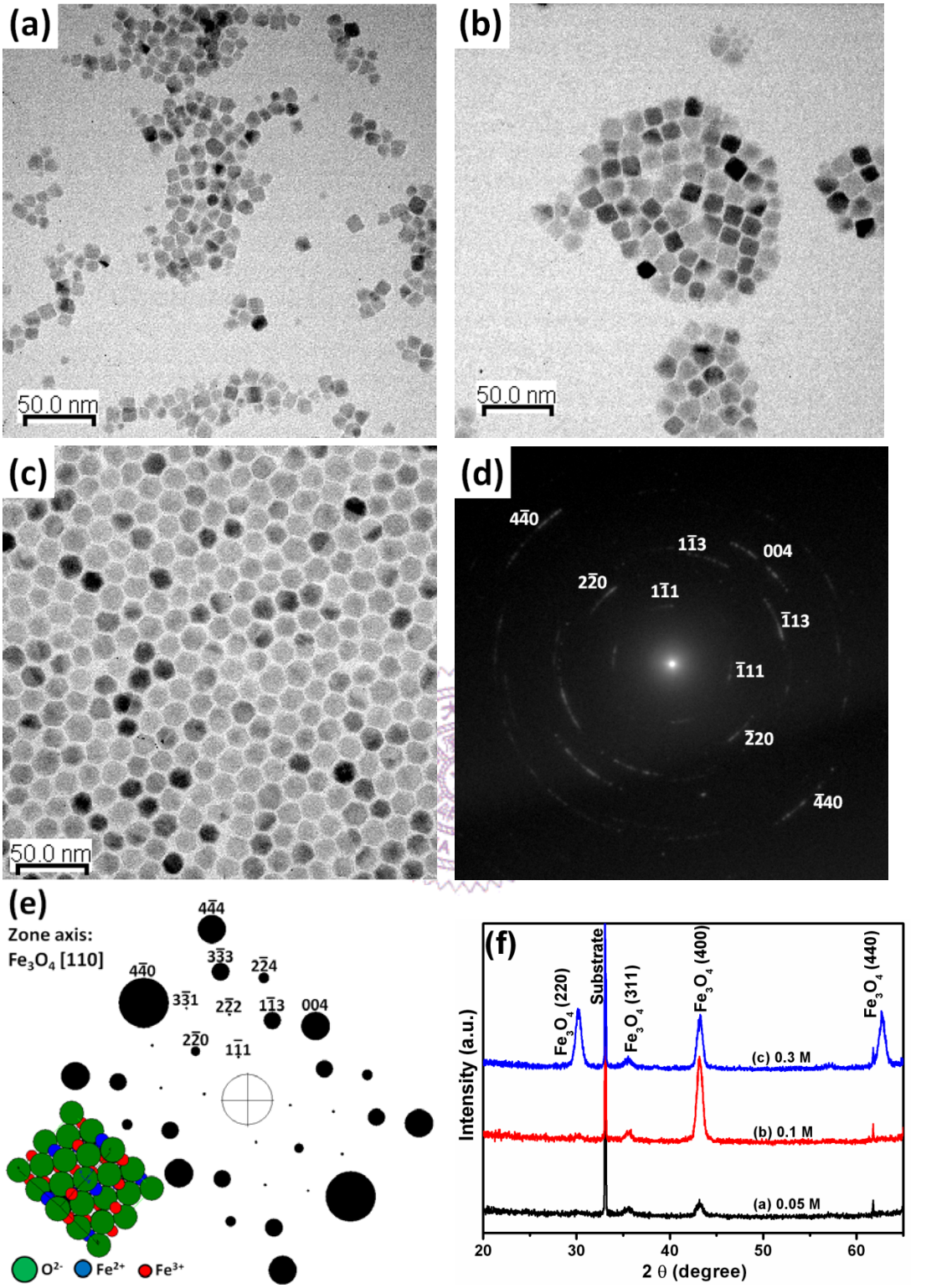

Fig. 4.10 (a), (b) and, (c) show TEM images of Fe_3O_4 NPs synthesized with different precursor concentrations of 0.05 M, 0.1 M, and 0.3 M, respectively. (d) shows the corresponding SAED pattern of (c). (e) displays the diffraction pattern and cell structure of Fe_3O_4 created by CaRIne Crystallography. The zone axis is Fe_3O_4 [110]. The XRD patterns of each sample were shown in (f).

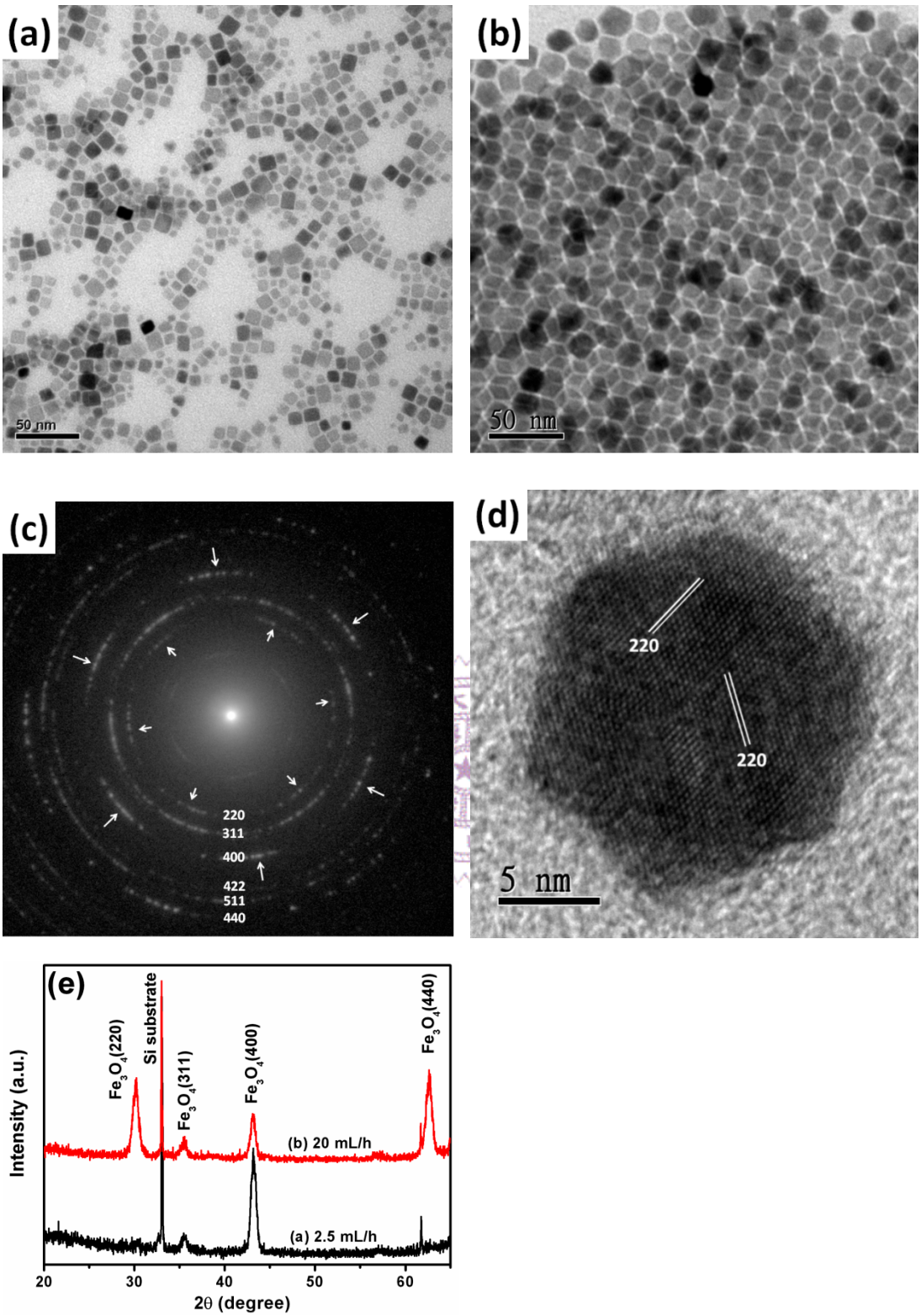

Fig. 4.11 (a) and (b) show TEM images of Fe_3O_4 NPs synthesized with the injecting rate of 2.5 mL/h and 20 mL/h, respectively. (c) is the corresponding SAED pattern of (b). (f) HRTEM image of polyhedral Fe_3O_4 NP on the zone axis of Fe_3O_4 [111] synthesized with the injecting rate of 20 mL/h. (e) shows the corresponding XRD patterns of Fe_3O_4 NPs on Si substrate.

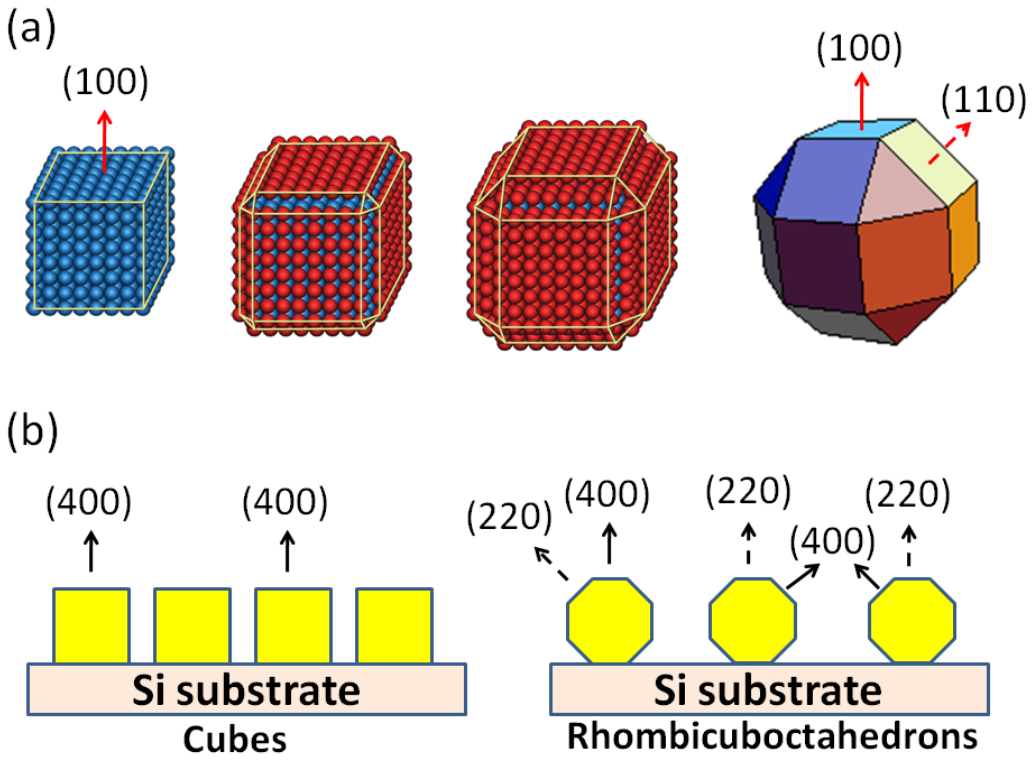

Scheme 4.3 (a) The schema illustrates how shape changes from cubic to rhombicuboctahedral. (b) The schema illustrates how cubic and rhombicuboctahedral nanocrystals create the preferential crystallographic orientation on the Si substrate.

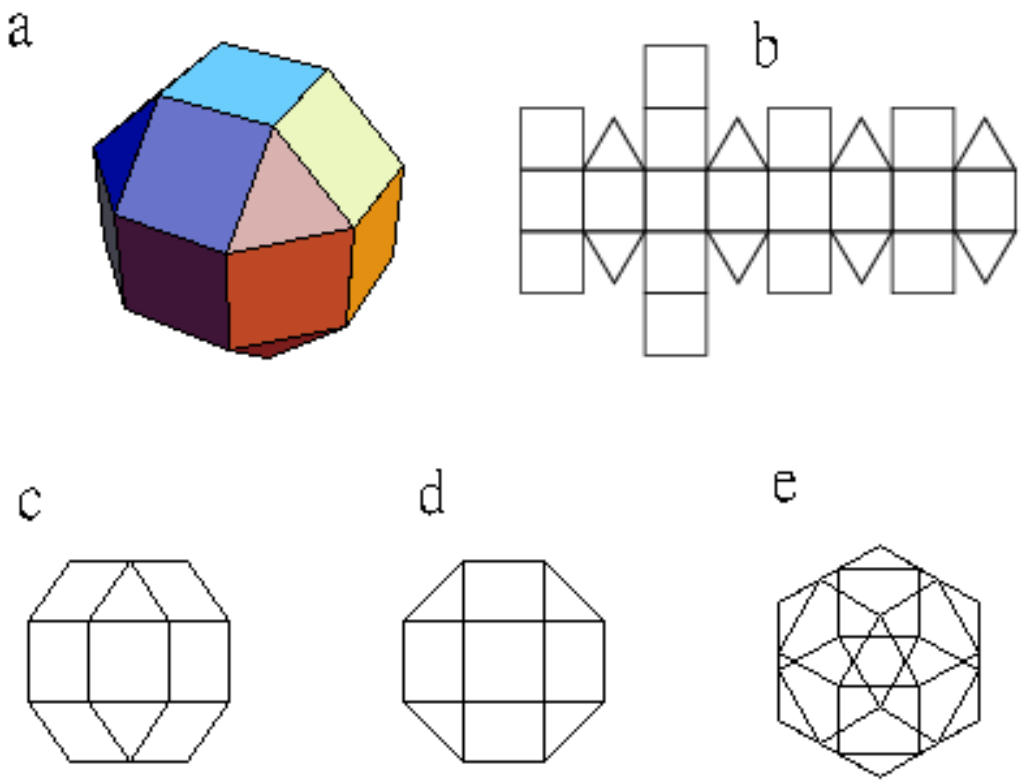

Fig. 4.12 The sketch of rhombicuboctahedron (a) pictorial drawing, (b) development drawing, and perspective views from (c) [110], (d) [100], and (e) [111].

4.3.4 The self-oriented assembly of shaped Fe_3O_4 nanoparticles

Assembling NPs into regular superstructure is the prerequisites for the novel nanodevices, such as high density recording media. The construction of long-range ordered superstructure requires NPs with uniform size and shape. Even though the long-range ordered superstructures have been demonstrated in the assembly of spherical NPs,[27] the formation of crystallographic-oriented superstructure was still a difficult task and was only found in the assembly of shaped NPs.[73-74] In this section, the formation of crystallographic-oriented superstructures on TEM grids and the formation of texture-like assembly on commercial Si substrates were discussed.

The square packing superlattice of Fe_3O_4 nanocubes was demonstrated through TEM image, shown in Fig. 4.2(a). The corresponding SAED pattern displays clear arced-spots instead of rings which indicates the formation of crystallographic orientation-ordered superlattice.[74] It was reported that the formation of square packing superlattice of nanocubes is due to the van der Waals interactions between the neighboring cubic NPs.[73-75] Yamamuro *et al.* had compared the van der Waals attractions between two close-packed arrangements (i.e., a square array and a pseudo-hexagonal array).[75] They found that the square packing array of nanocubes was energetically more stable than the pseudo-hexagonal array. The face-to-face attachment of square packing array not only has the maximum coordination but has the shortest center-to-center distance between the neighboring cubic NPs. The shortest center-to-center distance results in the maximum reduction of the potential energy due to van der Waals attractions. In our results, the Fe_3O_4 nanocubes were also

self-assembled into a square superlattice with face-to-face attachment mode. The crystallographic orientation of nanocube assembly was aligned simultaneously because all the faceted planes of nanocube are Fe_3O_4 {100} planes.

The oriented assembly of rhombicuboctahedral NPs was also observed from the TEM image and the corresponding SAED pattern. Interestingly, the assembly of rhombicuboctahedral NPs shows hexagonal array. It may because the shape of rhombicuboctahedral NPs is more close to spherical, the formation of hexagonal packing array can have more coordination and denser packing density than the square array. In addition, the NP assembly with [110] zone axis was observed, shown in Fig. 4.9 (d). The Fe_3O_4 [110] zone axis pattern was also reported in the assembly of octahedral Fe_3O_4 NPs in which the octahedral NPs also attached with face-to-face mode.[74] However, the formation of [110] zone axis pattern in our system is not clear. It might be because the {110} plane is one of the main faceted planes of rhombicuboctahedral NPs, the {110} planes also tend to be parallel to the surface of TEM grid. Furthermore creating the oriented assembly of rhombicuboctahedral NPs seems more difficult. The pattern of rhombicuboctahedral NPs shows longer arced-spots than that of cubic NPs, which means that the oriented assembly of rhombicuboctahedral NPs has larger deviation in crystallographic orientation. It may be because the rhombicuboctahedral NPs have multiple faceted planes, including {100}, {110}, and {111} planes. No specific plane has obviously shortest center-to-face distance. The center-to-face distance of {100} and {110} planes is only 5 % shorter that of {111} plane. Therefore, to control the attachment of neighboring

polyhedrons with specific plane becomes more difficult. This may explains why the oriented assembly of rhombicuboctahedral NPs has larger deviation in crystallographic orientation.

The TEM diffraction patterns, shown in Fig. 4.2(c) and 4.9(d), reflect the in-plane crystallographic orientation of NP assemblies on TEM grids, while the θ-2θ measurements of X-ray diffraction (XRD) patterns display the out-of-plane crystallographic orientation of nanocrystal assembly on Si substrates. Thus, the XRD patterns were used to verify the structural information as well as the preferential out-of-plane orientation of nanocube assembly on Si substrates. The strongest Fe_3O_4 (400) peak observed in XRD patterns of Fe_3O_4 nanocubes indicates the {100} planes of nanocubes are preferentially parallel to the Si substrates, shown in Fig. 4.5(b). Thus, the formation of regular square-packing superlattice with controlled crystallographic orientation on Si substrates was confirmed. Noteworthily, the rhombicuboctahedral NPs also show preferential orientation on Si substrate. Fig. 4.9 (f) shows the XRD pattern detected from polyhedral Fe_3O_4 nanocrystals. The intensified (220) and (400) peaks indicate that both Fe_3O_4 {110} and {100} planes are preferentially parallel to the Si substrate.

In this section, we have discussed the self-oriented assembly of shaped Fe_3O_4 NPs on TEM grids and the texture-like assembly on commercial Si substrates. The self- assembled superstructure of Fe_3O_4 nanocrystals may perform specific functionalities in biological systems, e.g. bio-mineralization. In addition, the assembly of magnetic NPs into a regular superlattice with an aligned easy-axis is highly favored for the applications of magnetic pattern media.

4.4 Summary

We have demonstrated the hot-injecting method with controlled injecting rate can be successfully used to synthesize the shaped Fe_3O_4 NPs. The cubic Fe_3O_4 NPs with the terminated {100} planes can be synthesized through injecting the Fe precursor at 290 °C with an injecting rate of 10 mL/min. Furthermore, the shape of Fe_3O_4 NPs can be changed from cubic to rhombicuboctahedral when increasing the injecting rate to 20 mL/h or doubling the precursor concentration. The formation of shape Fe_3O_4 NPs should be attributed to the limited and energetic monomers preferentially grew on the planes with high surface energy. Both cubic and rhombicuboctahedral NPs show crystallographic orientation-ordered superlattice on TEM grids and textured assembly on Si substrate.

Chapter V

Synthesis and Characterization of Shaped $FePt@Fe_3O_4$ Core/Shell Nanoparticles

5.1 Introduction

The core/shell structured magnetic NPs have attracted much attention due to their multifunctional properties and applications. The core/shell structure not only makes magnetic NPs possess both intrinsic properties from core and shell but creates extrinsic properties due to the interactions between core and shell.[22, 104-105] The combination of heterogeneous structured NPs and shape-control technique can enable heterogeneous shaped NPs to provide multifunctional properties as well as anisotropic behaviors. However, there are still limited reports on the preparation of shaped and heterogeneous magnetic NPs.[22, 24-25, 30, 106] Most of the studies on syntheses of core/shell nanocubes are focused on single metal core system and the shaped cores are need for epitaxial growth of shell.[107-108] Thus, developing and investigating the shaped and core/shell magnetic NPs are interesting studies but still difficult challenges to overcome.

In this chapter, synthesis and characteristics of $FePt@Fe_3O_4$ core/shell nanocubes are demonstrated and discussed. Even though the preparation of $FePt@Fe_3O_4$ core/shell structure has been developed, the synthesis of shaped $FePt@Fe_3O_4$ NPs has not been reported. In this study, the modified hot-injecting method associated with seed-mediated growth is

utilized to synthesize shaped FePt@Fe_3O_4 NPs. We found that the final shape of FePt@Fe_3O_4 NPs is dominated by the growth condition of Fe_3O_4 shell rather than the shape of FePt core. The HRTEM analysis reveals that the FePt core and Fe_3O_4 shell do not necessarily obey epitaxial relationship. The formation mechanism of shaped FePt@Fe_3O_4 NPs is also proposed in this chapter.

5.2 Experimental section

Shape FePt@Fe_3O_4 NPs were synthesized by combining the modified hot-injection method and seed-mediated growth. Prepared FePt NPs were as seeds to overgrow Fe_3O_4 shell on their surface. The core/shell structure and cubic shape of FePt@Fe_3O_4 nanocubes were demonstrated by electron tomography. Finally, HRTEM images were used to analyze the crystallographic relationship between FePt core and Fe_3O_4 shell.

5.2.1 Synthesis of FePt cores

Synthesis of FePt NPs was carried out by using standard Schlenk line techniques under Ar atmosphere. In a typical synthesis process, $Pt(acac)_3$ (0.25 mmol), $Fe(CO)_5$ (0.75 mmol), 1,2-hexadecanediol (2 mmol), oleic acid (1.2 mmol), and oleylamine (1.2 mmol) were mixed and dissolved in benzyl ether (10 mL). The mixed solution was heated to 290 °C with the heating rate of 5 °C/min. The temperature was kept at 290 °C for 30 min. Then the solution was naturally cooled to room temperature. The NPs were washed by ethanol and redispersed in hexane for several times. The final product was stored in hexane.

5.2.2 Synthesis of shaped FePt@Fe_3O_4 nanoparticles

Synthesis of shaped FePt@Fe_3O_4 core/shell nanocubes involves two steps, such as the synthesis of FePt core and the overgrowth of shaped Fe_3O_4 shell. The prepared FePt NPs mixed with oleic acid (0.3 mmol), oleylamine (0.3 mmol), and 1, 2-tetradecanediol (5 mmol) were dissolved in benzyl ether (15 mL) as the reaction solution. On the other hand,

$Fe(acac)_3$ (1 mmol) was dissolved in benzyl ether (5 mL) as the precursor solution. The reaction solution was dewatered at 120 °C for 1h, followed by being heated to the reflux temperature of 290 °C. Then, the precursor solution was injected into the hot reaction solution at 290 °C with the injecting rate of 10 mL/h. The fluctuation of reaction temperature is less than 5 °C during the injecting process. After the reaction was finished, the NPs were washed by ethanol and redispersed in hexane for several times. The final product was stored in hexane.

5.2.3 Characterization

Transmission electron microscope (TEM) images were obtained by JEOL JEM-1400 operating at 120 kV, while the HRTEM images were obtained by JEOL JEM-2010F operating at 200 kV. NPs were dispersed on the amorphous carbon-coated copper grids for TEM studies. X-ray diffraction (XRD) patterns were detected by Shimadzu XRD6000 using Cu Kα radiation. The XRD samples were prepared by dropping NP dispersion on Si substrate with controlled solvent evaporating rate. After the solvent evaporated, the dried NPs on Si substrate were used to do XRD measurement. Magnetic properties were measured by PMC VSM 3900 at room temperature with a maximum applied field of $\pm$ 18 kOe.

Electron tomography is reconstructed digitally from a tilt series of 2D projections. In our experiments, 121 electron micrographs were acquired by tilting the sample with a range of $\pm 60^{o}$ in 1^{o} increment. The tilt series was precisely aligned by the phase correlation method, and the reconstruction of 3D image was made by standard method of the filtered back projection (FBP).[109-111]

5.3 Results and discussion

5.3.1 Synthesis of FePt nanoparticles

The prepared FePt NPs perform as cores in the synthesis of shaped FePt@Fe_3O_4 NPs. In our experiments, FePt NPs were synthesized by the modified polyol method.[18, 37] TEM image of FePt NPs, shown in Fig. 5.1, shows that the shape of FePt NPs is spherical, and the average diameter is around 4.1 nm. FePt NPs are well dispersed on the TEM grid, and no obvious aggregation was observed. The electron diffraction pattern shown in Fig 5.2 were indexed as {111}, {200}, {220}, and {311} indicating that the as-synthesized FePt NPs are disordered fcc phase.

The composition of FePt NPs strongly affects their magnetic behaviors.[53] The composition of FePt NPs measured by ICP-MS is $Fe_{52}Pt_{48}$ which is close to the equatomic composition. The equatomic FePt NPs can be further annealed, and the disordered fcc phase is transformed to ordered $L1_0$ fct phase, which has a larger magnetocrystal anisotropy. The hysteresis loop shown in Fig. 5.3 reveals that the chemically disordered FePt NPs are superparamagnetic at room temperature.

Finally, in this section, the synthesis of FePt NPs was presented. The as-synthesized FePt NPs are spherical in shape and show superparamagnetic behaviors due to their small size of 4.1 nm. These small and spherical FePt NPs perform as the seeds to synthesize shaped FePt@Fe_3O_4 NPs.

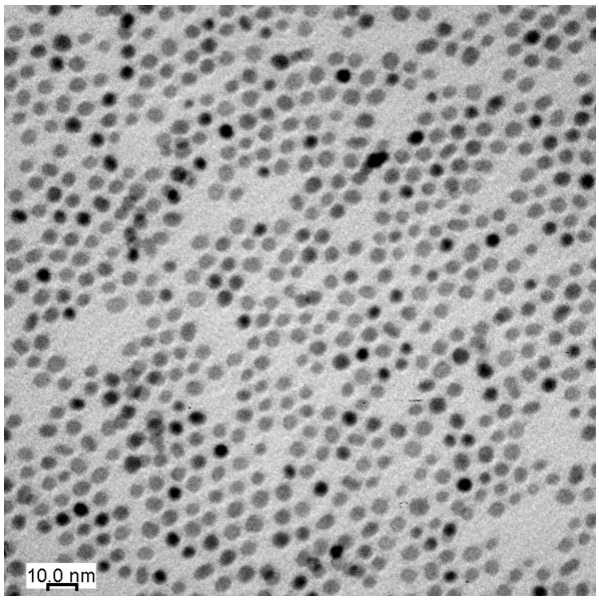

Fig. 5.1 The TEM image of as-synthesized FePt NPs

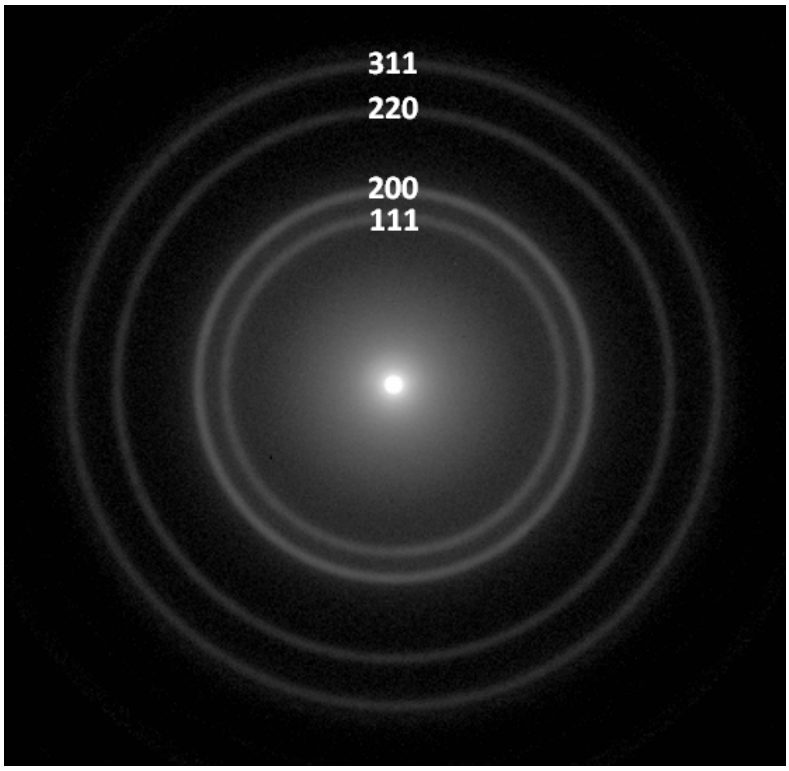

Fig. 5.2 The TEM diffraction pattern of the as-synthesized FePt NPs.

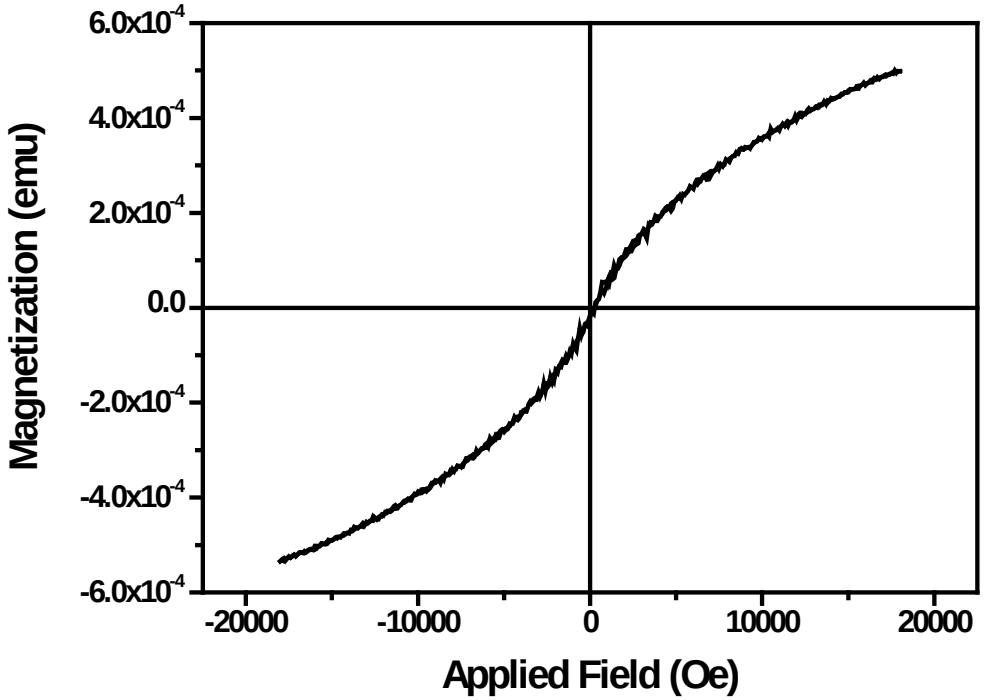

Fig. 5.3 The M-H hysteresis loop of the as-synthesized FePt NPs measured at room temperature. The maximum applied field is ± 18 kOe.

5.3.2 The synthesis and characterization of $FePt@Fe_3O_4$ core/shell nanocubes

The modified hot-injecting method combined with seed-mediated growth was used to synthesize the $FePt@Fe_3O_4$ core/shell nanocubes. Fig. 5.4(a) shows the TEM image of $FePt@Fe_3O_4$ core/shell nanocubes. The spherical FePt cores show darker contrast due to stronger electron scattering and have an average size of 4.1 nm. The average size of the bi-magnetic components is about 14.7 $\pm$ 1.1 nm. The majority of core/shell nanocubes were composed of a single spherical FePt core inside the Fe_3O_4 cubes. The $FePt@Fe_3O_4$ core/shell nanocubes were also self-assembled into square packing superlattice which is similar to the arrangement of Fe_3O_4 nanocubes. The corresponding SAED pattern, shown in Fig. 5.4(b), also displays clear arced-spots instead of rings. The arced-spots with 4-fold symmetry are indexed as {220}, {400}, and {440} which indicate that the electron beam is along the [001] crystallographic orientation of Fe_3O_4.

The size of $FePt@Fe_3O_4$ core/shell nanocubes can be further enlarged by increasing the quantity of injected Fe precursor. The quantity of Fe precursor was increased to 2 and 3 mmol, while keeping the same precursor concentration to avoid the shape change of Fe_3O_4 shell. Fig 5.5(a) and (b) show the TEM images of $FePt@Fe_3O_4$ core/shell nanocubes synthesized with 2 and 3 mmol of precursors, respectively. The average edge length of nanocubes synthesized with 2 and 3 mmol Fe precursors are increased to 21 and 43 nm, respectively.

Since the conventional TEM images only reveal the two-dimensional (2D) projections, they can hardly tell the difference between the FePt core

embedding inside the Fe_3O_4 nanocube from sticking on the Fe_3O_4 surface. To ensure the core/shell structure of cubic FePt@Fe_3O_4 NPs, the electron tomography technique was employed to reconstruct the 3D image of FePt@Fe_3O_4 core/shell nanocubes. The tomography is reconstructed digitally from a tilted series of 2D projections. Fig. 5.6 shows some chosen TEM bright field images of FePt@Fe_3O_4 nanocubes taken with different tilted angles. The tilted series were precisely aligned by the phase correlation method,[111] and the reconstruction were made by standard method of the filtered back projection (FBP).[109-110] Fig. 5.7(b) depicts the reconstructed TEM tomography from three FePt@Fe_3O_4 core/shell nanocubes shown in Fig. 5.7(a). The slight distortion of cubic shape should be due to the effect of "missing wedge", which caused by the insufficient tilted angles in 3D reconstruction.[112] Fig. 5.7(c) is a transparent view that shows the FePt NPs are indeed encapsulated inside the Fe_3O_4 nanocubes instead of sticking outside the surface. The elemental analysis measured by nano-beam EDX spectra, shown in Fig. 5.7(d) and (e), was acquired by positioning nano-electron beams onto two positions marked by a solid circle on the shell and a dashed circle on the core in Fig. 5.7(a), respectively. Although the FePt NP is embedded inside the Fe_3O_4 nanocube, the strong Pt signal only appears in FePt core region, but not appears in Fe_3O_4 shell region. In addition, the peak marked as solid triangle (▲) was suspected as the signal of Si, which might be the contamination during the procedure of sample preparation.

Hence, we have demonstrated that the FePt@Fe_3O_4 core/shell nanocubes can be successfully synthesized by the hot-injection method combined with seed-mediated growth. From the TEM tomography, it can

be clear confirmed that the FePt was indeed embedded inside the Fe_3O_4. The cubic shape of Fe_3O_4 was also confirmed by TEM tomography. The typical size of FePt@Fe_3O_4 nanocubes is about 14.7 nm, and can be enlarged to 21 and 43 nm by increasing the quantity of Fe precursor to 2 and 3 mmol, respectively. The cubic core/shell FePt@Fe_3O_4 nanocrystals also self-assembled into square packing superlattice with oriented crystallographic orientation. Finally, it can be presumed that after the FePt core was covered with Fe_3O_4 shell, the final shape of the core/shell NPs was dominated by the growth condition of Fe_3O_4 shell.

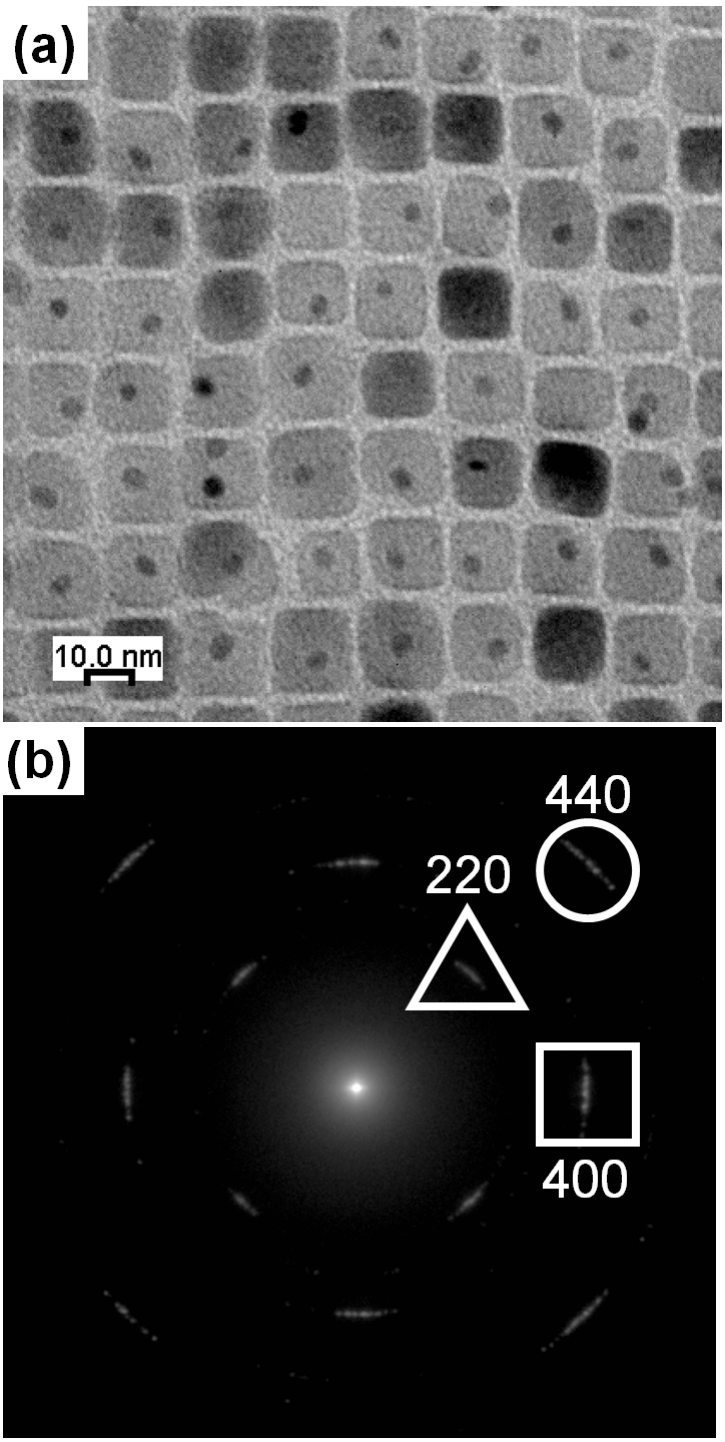

Fig. 5.4 (a) TEM images of FePt@Fe_3O_4 nanocubes, (b) the corresponding SAED pattern of (a).

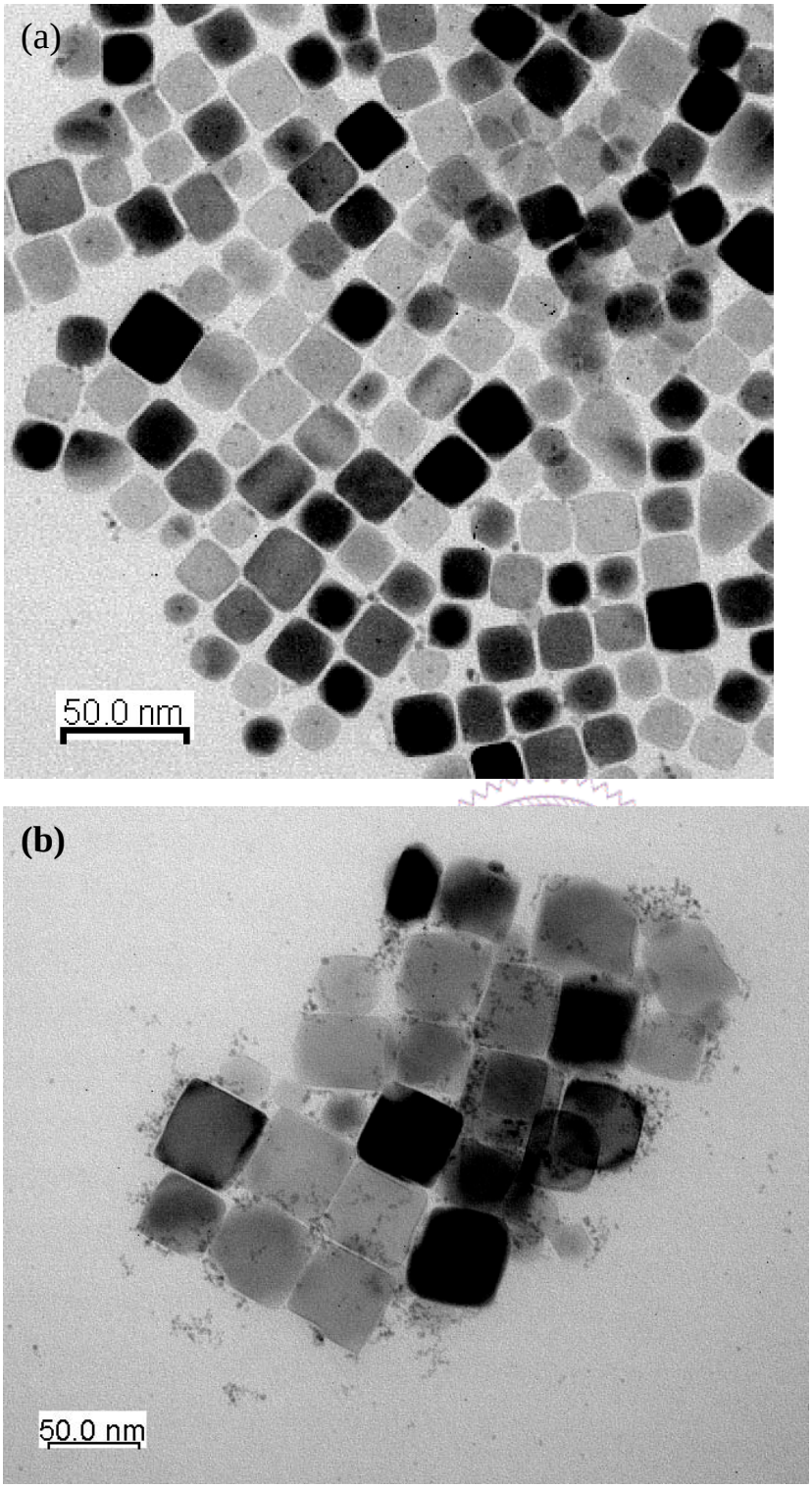

Fig. 5.5 These TEM images shows the larger FePt@Fe_3O_4 nanocubes with the average size of (a) 21 nm and (b) 43 nm

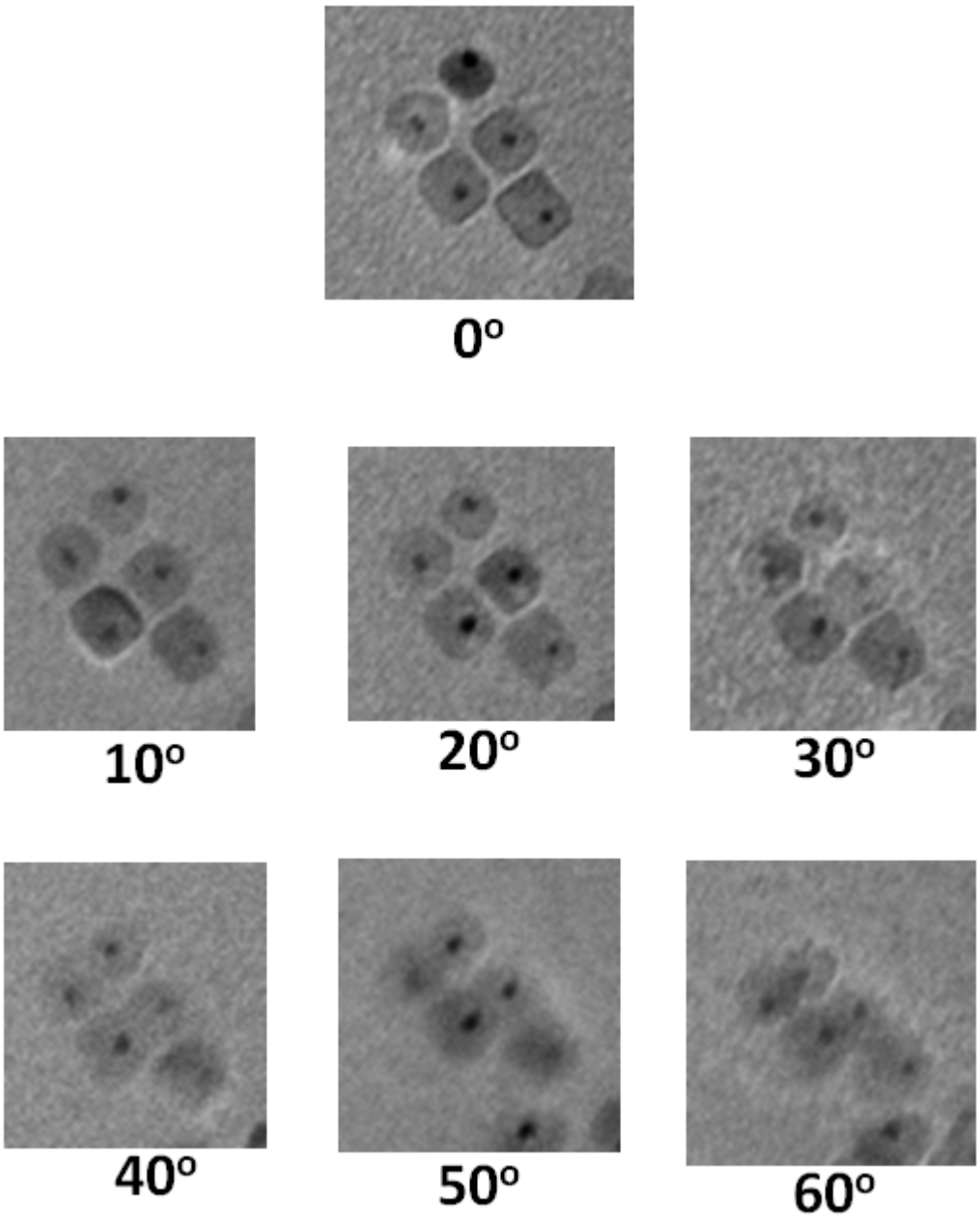

Fig. 5.6 The series of tilted TEM images of FePt@Fe_3O_4 nanocubes. All of tilted TEM images were used to reconstruct the 3D tomography image.

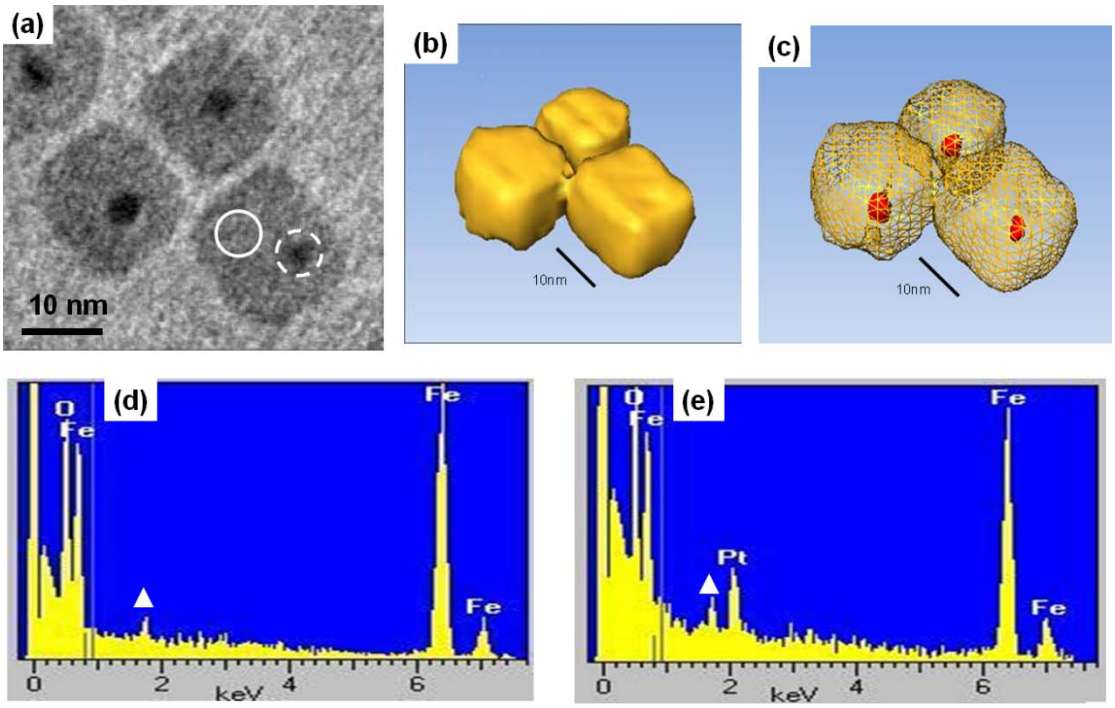

Fig. 5.7 (a) TEM image of FePt@Fe_3O_4 nanocubes, (b) the 3D-reconstrcuted TEM tomography. The 3D image was reconstructed from three nanocubes in (a), (c) the transparent view of (b), (d) EDX spectrum of the solid-circle region in (a), (e) EDX spectrum of the dash-circle region in (a).

5.3.3 The formation mechanism of shaped FePt@Fe_3O_4 nanocrystals and the crystallographic relationship between FePt core and Fe_3O_4 shell

FePt NPs behaved as seeds in the synthesis of FePt@Fe_3O_4 core/shell nanocubes. The formation mechanism of FePt@Fe_3O_4 core/shell nanocubes was proposed in Scheme 5.1. Due to the low injection rate, the concentration of iron oxide monomers was lower than homogeneous nucleation threshold at the initial stage during precursor injection; therefore, iron oxide monomers preferred to heterogeneously nucleate on the existing FePt seeds to form the FePt@Fe_3O_4 core/shell structure. The subsequently grown Fe_3O_4 shell still showed a cubic shape even though the FePt seed had no specific terminated planes and possessed an isotropic spherical shape. It suggested that the presence of FePt seeds just influenced the nucleation stage while the final shape of FePt@Fe_3O_4 nanocrystals was mainly dominated by the growth of Fe_3O_4. After the cubes were formed, each {100} facet of Fe_3O_4 nanocubes had the same growth rate due to their equal surface energy. Thus, further growth mainly increased the nanocube size without changing their shapes.

To further confirm the final shape of FePt@Fe_3O_4 core/shell nanocrystals was dominated by the growth condition of Fe_3O_4 shell not by the shape of FePt core, the identical FePt NPs were used as the seeds to synthesize FePt@Fe_3O_4 nanocrystals under the growth condition of rhombicuboctahedral Fe_3O_4 nanocrystals. The synthesis of FePt@Fe_3O_4 nanocrystals were also combined the seed-mediated growth with the modified hot-injection method. However, the precursor concentration was doubled to increase the monomer concentration, which can change the

shape formation of Fe_3O_4. Fig. 5.8 shows the TEM images of rhombicuboctahedral FePt@Fe_3O_4 nanocrystals. It is clear that the Fe_3O_4 shell is still shaped but not cubic. The size of rhombicuboctahedral FePt@Fe_3O_4 nanocrystals is about 18 nm, which is slightly larger than that of cubic FePt@Fe_3O_4 nanocrystals. A very small number of uncoated FePt NPs was observed, and the uncoated FePt NPs can be further removed by centrifugation. The formation of rhombicuboctahedral FePt@Fe_3O_4 nanocrystals depicts that the final shape of Fe_3O_4 shell was dominated by its growth condition.

The other important concern in synthesizing the heterogeneous shaped nanocrystals is the crystallographic relationship between core and shell. In some reports, it was found that the epitaxial growth on shaped core is vital to create the heterogeneous core/shell nanocrystals. [107] Fan *et al.* has proposed that for the epitaxial layered growth of heterogeneous core/shell nanocrystals, the lattice constants of two materials should be comparable with the lattice mismatch less than 5%.[107] However, the lattice constant of Fe_3O_4 is 8.396 Å, while that of disordered fcc FePt is only 3.877 Å. The lattice mismatch between the lattice constant of Fe_3O_4 and the twice lattice constant of FePt is 8.3 % which is over the allowed maximum lattice mismatch. Hence, the epitaxial growth Fe_3O_4 shell on FePt core is hard to occur.

HRTEM was used to investigate the crystallographic relationship between FePt core and Fe_3O_4 shell. Fig. 5.9(a) shows HRTEM image of FePt@Fe_3O_4 core/shell nanocubes. The lattice fringes correspond to {220} lattice planes of Fe_3O_4 while the facet is {400}. Noteworthily, the lattice image near the FePt core position still exhibits characteristics of Fe_3O_4

rather than that of FePt. The invisible FePt lattice image might be because of the crystallographic orientation of FePt core is not on zone axis. No Morié fringes can be observed which suggests that no definite crystallographic relationship exists between FePt core and Fe_3O_4 shell, unlike in Au@Pd system, in which the epitaxial growth of Pd shell on Au cores leads to the Morié fringes parallel to each other in the core area.[107] The electron diffraction (ED) pattern can be used to investigate the crystallographic relationship between two contacting components by analyzing the diffraction spots of these two materials. However, in our experiments, the size of Fe_3O_4 shell is relatively larger than that of FePt core. Therefore, the diffraction spots of Fe_3O_4 shell are overwhelmingly brighter than the spots contributed by FePt core. The diffraction spots of FePt core easily become invisible. To overcome the contrast problem caused by the significant difference in volume, the nano-beam diffraction was used to enhance the brightness of FePt diffraction spots. Fig. 5.9(b) shows a nano-beam diffraction (NBD) pattern recorded by positioning a nano-electron beam with the beam size of about 2 nm on the white circle in Fig. 5.9(a). No periodic diffraction spots from FePt core observed in Fig. 5.9(b) indicates that the FePt core and Fe_3O_4 shell do not obey epitaxial relationship.

Because FePt core and Fe_3O_4 shell do not necessarily obey epitaxial relationship, it means that when Fe_3O_4 shell is on zone axis, the FePt core might be off zone axis, and vice verse, shown in Fig. 5.10. The on-zone-axis image shows 2D lattice fringe, while the off-zone-axis image just shows 1D lattice fringe or none. Hence, it is reasonable that the FePt core can become on zone axis by tilting the sample, while the

Fe_3O_4 shell becomes off zone axis. Fig. 5.11 shows the HRTEM image of FePt@Fe_3O_4 core/shell nanocubes with the FePt core on zone axis. It is clear that the FePt core shows 2D lattice fringe with atomic resolution, while the Fe_3O_4 shell only show 1D lattice fringe. Hence, it is clear evident that the FePt core and Fe_3O_4 shell did not necessarily have epitaxial crystallographic relationship.

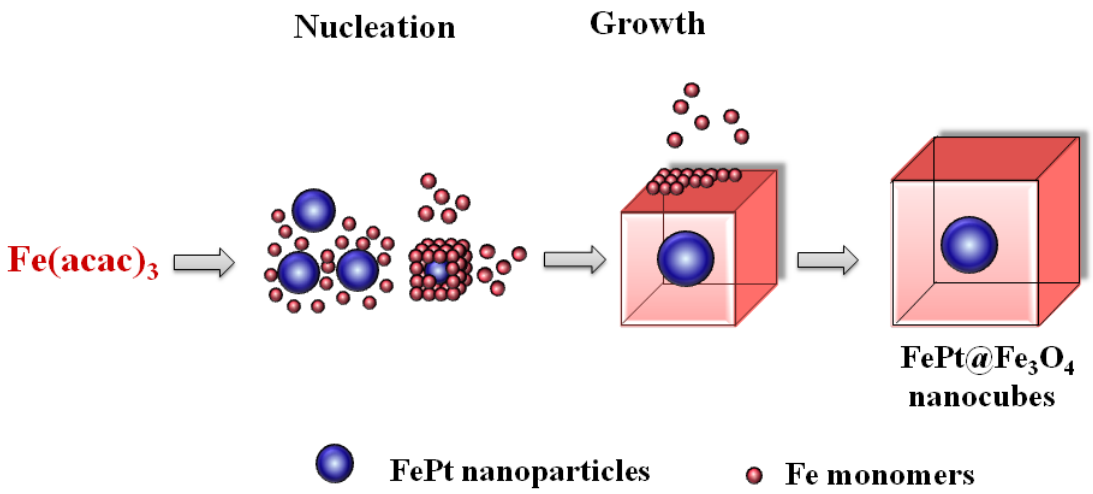

Scheme 5.1 The scheme illustrates the formation mechanism of FePt@Fe_3O_4 nanocubes.

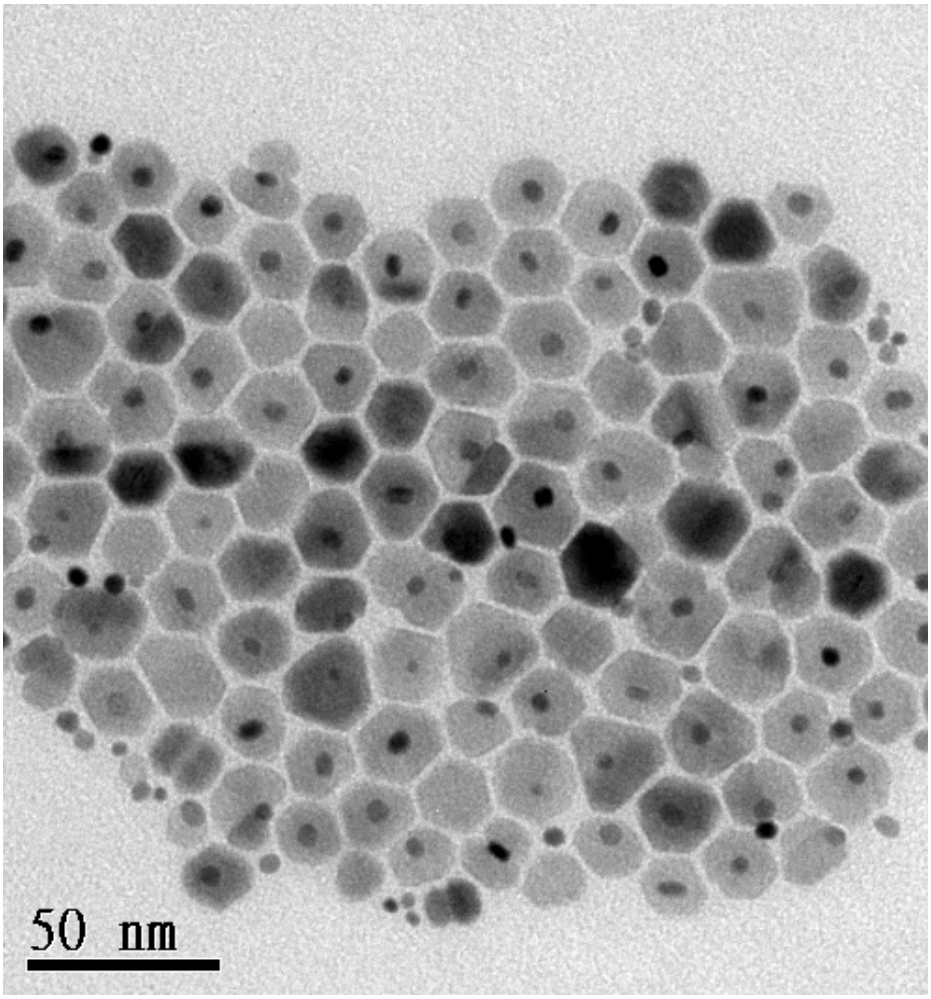

Fig. 5.8 TEM images of polyhedral FePt@Fe_3O_4 core/shell nanocrystals.

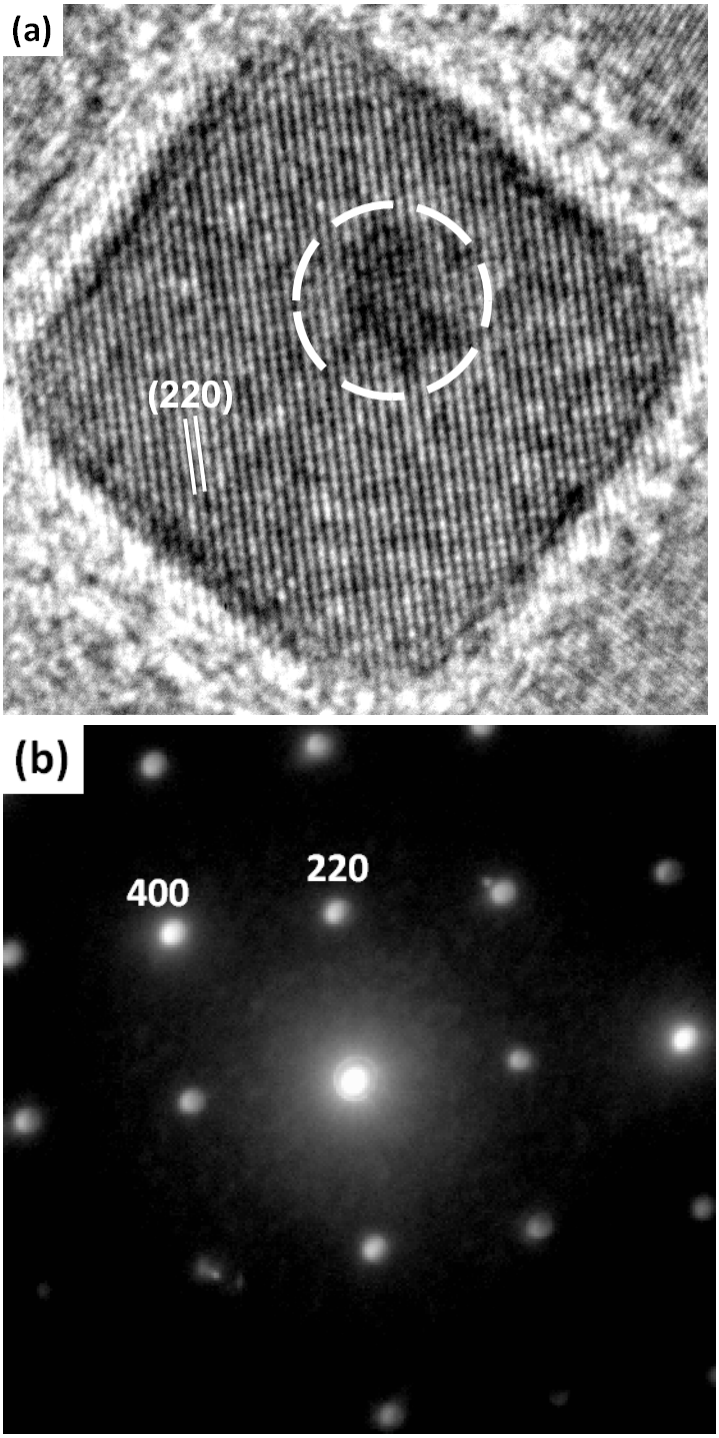

Fig. 5.9 (a) The HRTEM image of FePt@Fe_3O_4 core/shell nanocubes. The dashed circle indicates the position of FePt core. (b) The nano-beam diffraction pattern corresponds to the area within the white circle in (a)

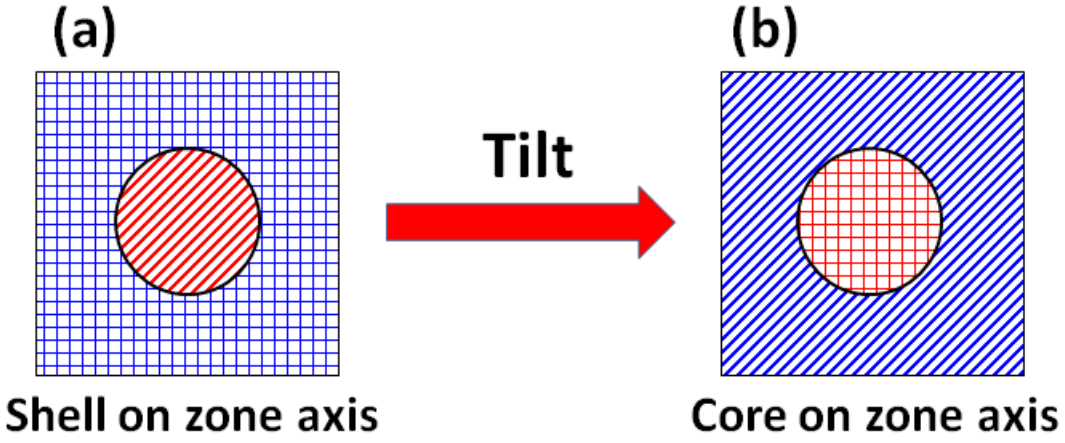

Fig. 5.10 The schema of HRTEM images when (a) shell is on zone axis and (b) core is on zone axis. Here we proposed that core and shell did not have epitaxial relationship.

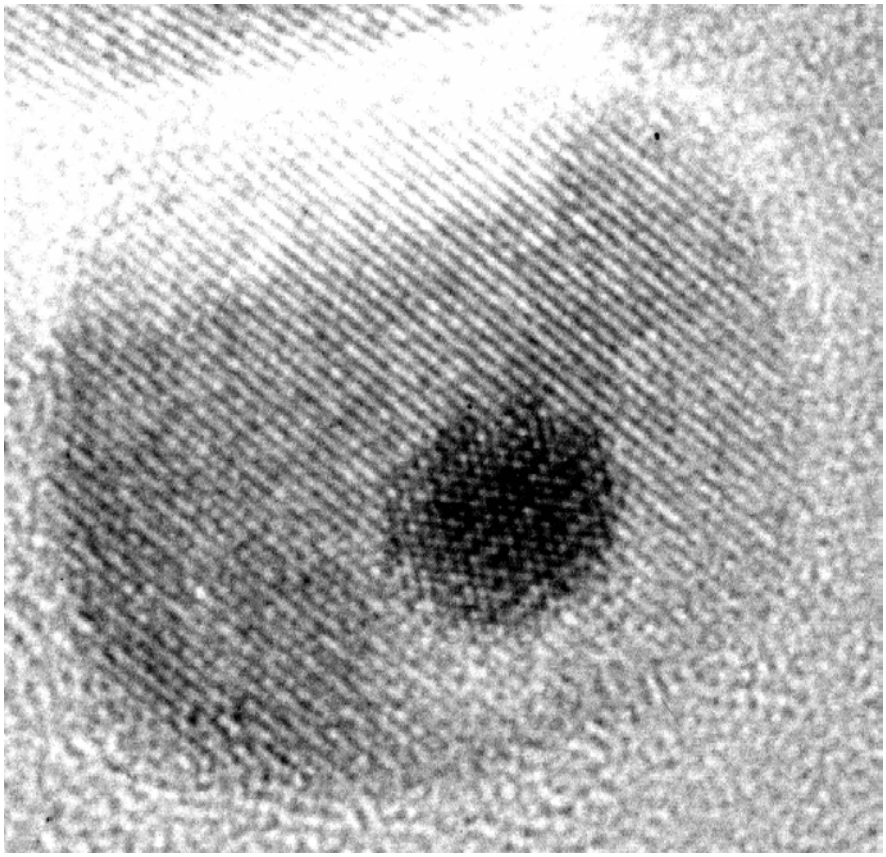

Fig. 5.11 The HRTEM image of FePt@Fe_3O_4 nanocrystals. The 2D lattice fringe of core indicated the FePt is on zone axis, while the 1D fringe of shell indicated the Fe_3O_4 is off-zone axis.

5.4 Summary

In this chapter, we have successfully synthesized the FePt@Fe_3O_4 core/shell nanocubes by using the hot-injection method combined with seed-mediated growth. The final shape of FePt@Fe_3O_4 nanocrystals was primarily dominated by the growth condition of Fe_3O_4 shell but not the shape of core. The TEM tomography confirmed that the FePt was embedded inside the cubic Fe_3O_4 shell. HRTEM images were further verified that FePt core and Fe_3O_4 shell did not necessarily have epitaxial relationship, which indicates the core materials do not need to have similar lattice constant with Fe_3O_4. So, the fewer requirements in shape and lattice constant of core materials make the hot-injection method be reasonably suitable for the synthesis of core/Fe_3O_4 shell nanocubes with various and desired core materials.

Chapter VI

The Special Features and Potential Applications of Shaped Fe_3O_4 and FePt@Fe_3O_4 Nanoparticles

6.1 Introduction

The shaped NPs have been extensively studied in recent years because the shape of NCs plays important roles in tailoring the electric, photonic, magnetic, and catalytic properties.[67-68, 113] Fe_3O_4 has been used as the catalyst for the high-temperature water gas shift reaction which is an essential process to adjust the CO/H_2 ratio in the industrial production of hydrogen.[76] Interestingly, on the Fe_3O_4{001} planes, water tends to dissociate in oxygen vacancies on the defective site and partially dissociate on the nondefective surface.[77] However, on the Fe_3O_4{111} planes, water tends to fully dissociate. It is believed the catalytic ability of Fe_3O_4 is related to the presence of both ferrous (Fe^{2+}) and ferric (Fe^{3+}) ions in its inverse spinel structure.[77] Interestingly, our cubic Fe_3O_4 NPs are terminated at {100} planes, while rhombicuboctahedral Fe_3O_4 NPs are principally terminated at {100} and {110} planes. Therefore, investigating the cation site occupancies of shaped Fe_3O_4 NPs may be helpful to study the catalytic ability of Fe_3O_4.

The other important application of Fe_3O_4 NPs is as the MRI T_2 contrast agent, in which the high saturation magnetization is required to

significantly reduce the T_2 transverse relaxation time. It has been demonstrated that embedding the high-magnetic-moment core inside iron oxide shell can improve the r_2 relaxivity.[114-117] FePt also has higher saturation magnetization than Fe_3O_4, and FePt NPs have been widely studied in biomedical application.[19-20, 118] It was reported that the uncoated FePt NPs have no significant toxicity on bEnd3 cells during 24 hours.[21] Consequently integrating FePt core into Fe_3O_4 nanocubes can combine the good bio-compatibility of Fe_3O_4 with the relatively high M_S of FePt. Recently, heterogeneous FePt-Fe_3O_4 NPs were also demonstrated for MRI application.[24-25] However, the preparation of non-spherical FePt-Fe_3O_4 dimmers and their MRI applications have not been reported yet.

In this chapter, the x-ray magnetic circular dichroism (XMCD) was used to measure the cation site occupancies of shaped Fe_3O_4 and FePt@Fe_3O_4 NPs. The shape-dependent XMCD spectra were observed, which indicated the cation site occupancies of Fe_3O_4 NPs may be affected by the terminated planes or by the surface-to-volume ratio. The MRI measurements of Fe_3O_4 and FePt@Fe_3O_4 nanocubes were also demonstrated. FePt@Fe_3O_4 nanocubes show better r_2 enhancement than the Fe_3O_4 nanocubes and the commercial MRI T_2 agent, which indicates that the FePt@Fe_3O_4 nanocubes can be the potential candidate as the MRI T_2 agent.

6.2 Results and discussion

6.2.1 The XMCD measurements of cation site occupancies of shaped Fe_3O_4 and FePt@Fe_3O_4 nanoparticles

Fe_3O_4 has an inverse spinel structure with the formula of $(Fe^{3+})_A(Fe^{2+}Fe^{3+})_BO_4$. Tetrahedral sites (A site, T_d) were occupied by Fe^{3+} ions, while octahedral sites (B site, O_h) were occupied by equal numbers of Fe^{2+} and Fe^{3+} ions. The Fe $L_{2,3}$-edge XMCD spectrum of Fe_3O_4 can show features of three different chemical environments, namely Fe^{3+}_{Td}, Fe^{2+}_{Oh}, and Fe^{3+}_{Oh}, resulting in two large negative peaks with a positive peaks in between, shown Fig. 6.1.[49] It was reported that XMCD is a powerful tools to determine the cation site occupancies of ferrite spinel materials.[49, 119-120] The relative peak intensities can reflect the cation site occupancies of Fe_3O_4. In our experiments, the Fe $L_{2,3}$-edge X-ray absorption spectroscopy (XAS) and XMCD measurements have been performed in total electron yield (TEY) mode at NSRRC in Taiwan with an applied magnetic field of 1T to fully saturate these NPs.

Fig 6.2(a) shows the XMCD spectra of Fe_3O_4 and FePt@Fe_3O_4 nanocubes to investigate the core/shell effect in cation site occupancies. Both samples show almost identical spectra indicating that the core/shell structure does not affect cation site occupancies. No metallic Fe peaks contributed by the FePt core were found. It is because the probing depth of XMCD is only about 1~2 nm, which is thinner than the thickness of Fe_3O_4 shell. Noteworthily, even the Fe_3O_4 and FePt@Fe_3O_4 nanocubes show identical XMCD spectra, both spectra are different from the theoretical and experimental spectra of bulk Fe_3O_4, shown in Fig. 6.1. In

typical XMCD spectrum of bulk Fe_3O_4, the negative peak contributed by Fe^{2+}_{Oh} is stronger than the other negative peak contributed by Fe^{3+}_{Oh}. However, in both XMCD spectra of Fe_3O_4 and FePt@Fe_3O_4 nanocubes, the Fe^{3+}_{Oh} peaks are stronger than the Fe^{2+}_{Oh} peaks.

Even the core/shell FePt@Fe_3O_4 nanocubes did not show different XMCD spectra, the shape dependent XMCD spectra were observed in the cubic and rhombicuboctahedral Fe_3O_4 NPs. Fig. 6.2(b) shows the normalized XMCD spectra of cubic Fe_3O_4 NPs and rhombicuboctahedral ones. For the cubic NPs, the maximum peak was contributed by Fe^{3+}_{Oh}, while this peak was reduced in the spectrum of rhombicuboctahedral NPs. It seems that the XMCD spectrum of rhombicuboctahedral Fe_3O_4 NPs is more close to that of bulk Fe_3O_4. The shape-dependent XMCD spectra were also found in the cubic and rhombicuboctahedral FePt@Fe_3O_4 NPs, shown in Fig. 6.2(c). These results indicated that more ferric ion, Fe^{3+}, occupied at the octahedral sites than ferrous ion, Fe^{2+}, when the shapes of Fe_3O_4 and FePt@Fe_3O_4 NPs become cubic.

Noteworthily, the maximum Fe^{3+}_{Oh} peak in the Fe $L_{2,3}$-edge XMCD spectrum was commonly observed in γ-Fe_2O_3. Therefore, it is important to identify if the particular XMCD spectra of Fe_3O_4 and FePt@Fe_3O_4 nanocubes were contributed from the shape effect or from the existence of γ-Fe_2O_3. Further characterization to distinguish Fe_3O_4 from γ-Fe_2O_3 was conducted by using X-ray photoelectron spectroscopy (XPS). Fig. 6.3(a) and (b) show the XPS spectra of Fe_3O_4 and FePt@Fe_3O_4 nanocubes, respectively. No satellite peak between the peaks of Fe $2p_{3/2}$ and Fe $2p_{1/2}$ was observed, indicating that these nanocubes were consistent with Fe_3O_4 component. Hence, it can be concluded that the

particular XMCD spectrum of cubic Fe_3O_4 NPs is not attributed to the existence of γ-Fe_2O_3. The Fe_3O_4 XMCD spectra with the strongest Fe^{3+}_{Oh} peak were also found by Park *et al.*.[121] When the size of Fe_3O_4 NPs was smaller than 9 nm, the intensity of Fe^{3+}_{Oh} peak became comparable to that of Fe^{2+}_{Oh}. Pérez *et al.* also found the strongest Fe^{3+}_{Oh} peak in the XMCD spectrum of 5 nm Fe_3O_4 NPs.[122] Noteworthily, both cubic and smaller Fe_3O_4 NPs have larger portion of surface atoms (ions) than rhombicuboctahedral and larger NPs, respectively. Therefore, it can be presumed that the higher surface-to-volume ratio of Fe_3O_4 NPs increases the occupancies of ferric ions, Fe^{3+}, at octahedral sites. On the other hand, the terminated planes of NPs may be the other reason why the XMCD spectra show the strongest Fe^{3+}_{Oh} peak. The $(\sqrt{2}\times\sqrt{2})R45°$ reconstruction on $Fe_3O_4(100)$ surface has been observed,[78] in which the terminated planes are composed of octahedral iron ($Fe_{Oh}^{2+,\,3+}$) and oxygen, shown in Fig. 2.31. It was also reported that Fe_3O_4 (100) surface has a higher Fe^{3+}/Fe^{2+} ratio than bulk.[123] So, the maximum Fe^{3+}_{Oh} peak in the XMCD spectrum of cubic Fe_3O_4 NPs may be attributed to their terminated {100} planes.

In this section, the shape dependent XMCD spectra of Fe_3O_4 and FePt@Fe_3O_4 NPs have been demonstrated. For cubic NPs, more ferric ions, Fe^{3+}, occupy the octahedral site of the spinel structure. However, for rhombicuboctahedral NPs, the cation site occupancies are more close to the bulk Fe_3O_4. The particular XMCD spectra may be due to the high surface-to-volume ratio of cubic NPs. The {100} terminated planes of cubic NPs may be the other reason causing the particular XMCD spectra.

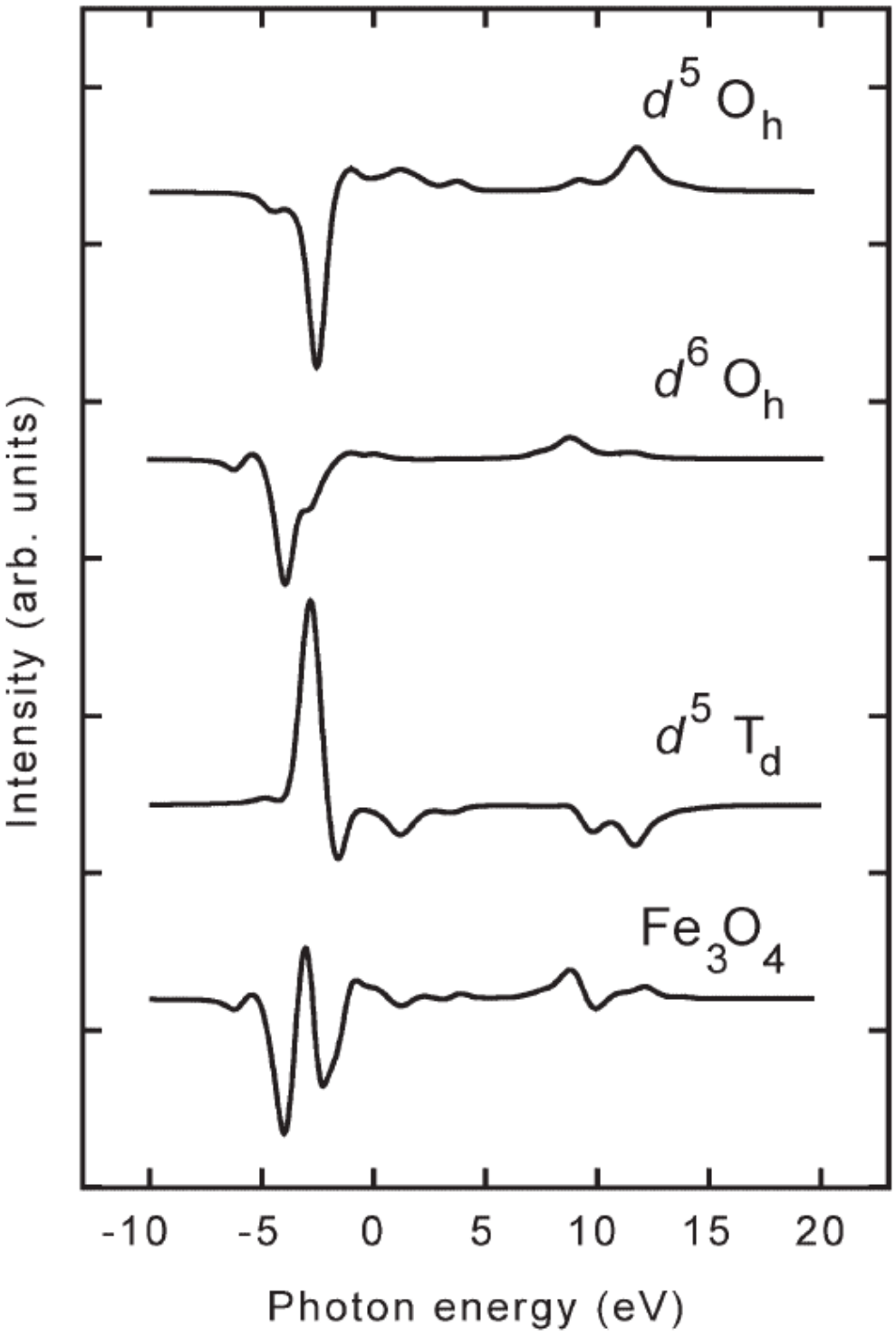

Fig. 6.1 The calculated d^5 O_h($Fe^{3+}{}_{Oh}$), d^6 O_h ($Fe^{2+}{}_{Oh}$) , d^5 T_d ($Fe^{3+}{}_{Td}$) components of the XMCD spectrum and the resulting summed calculated spectrum of Fe_3O_4.[49]

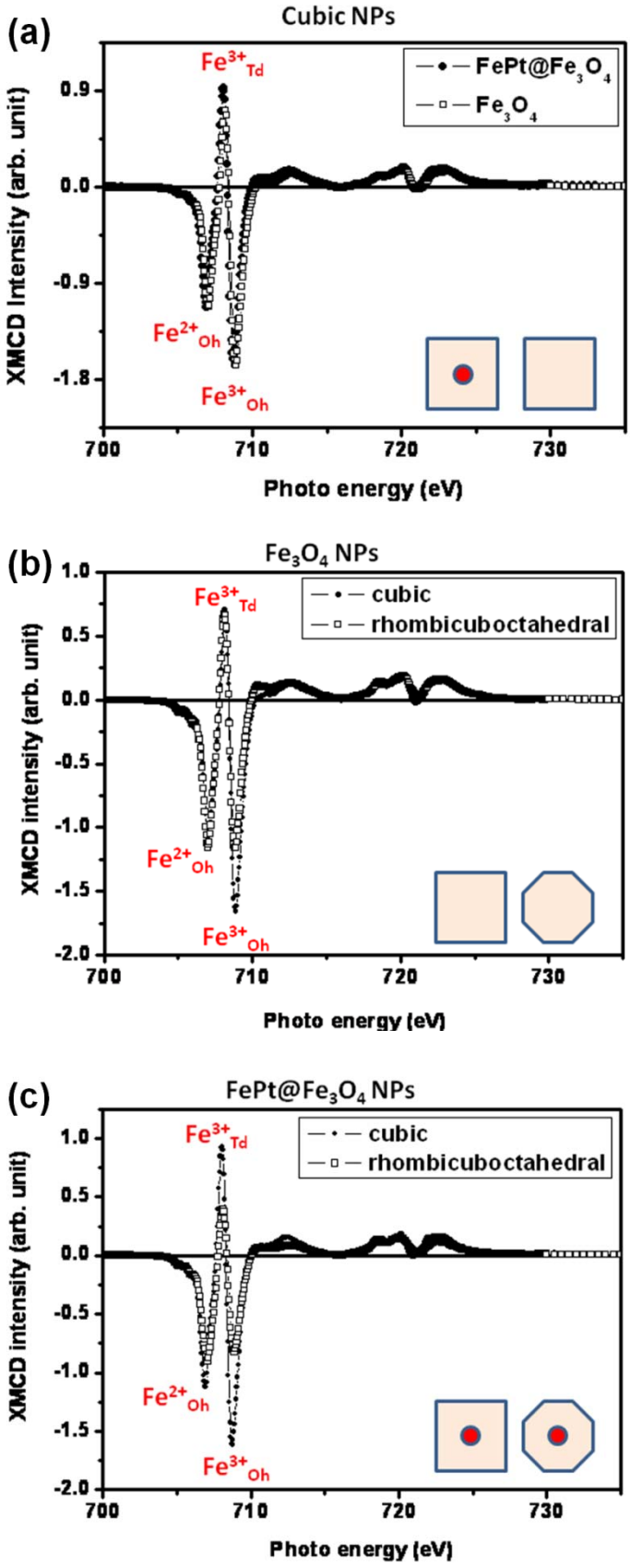

Fig. 6.2 The XMCD spectra of (a) cubic Fe_3O_4 and FePt@Fe_3O_4 NPs, (b) cubic and polyhedral Fe_3O_4 NPs, and (c) cubic and polyhedral FePt@Fe_3O_4 NPs

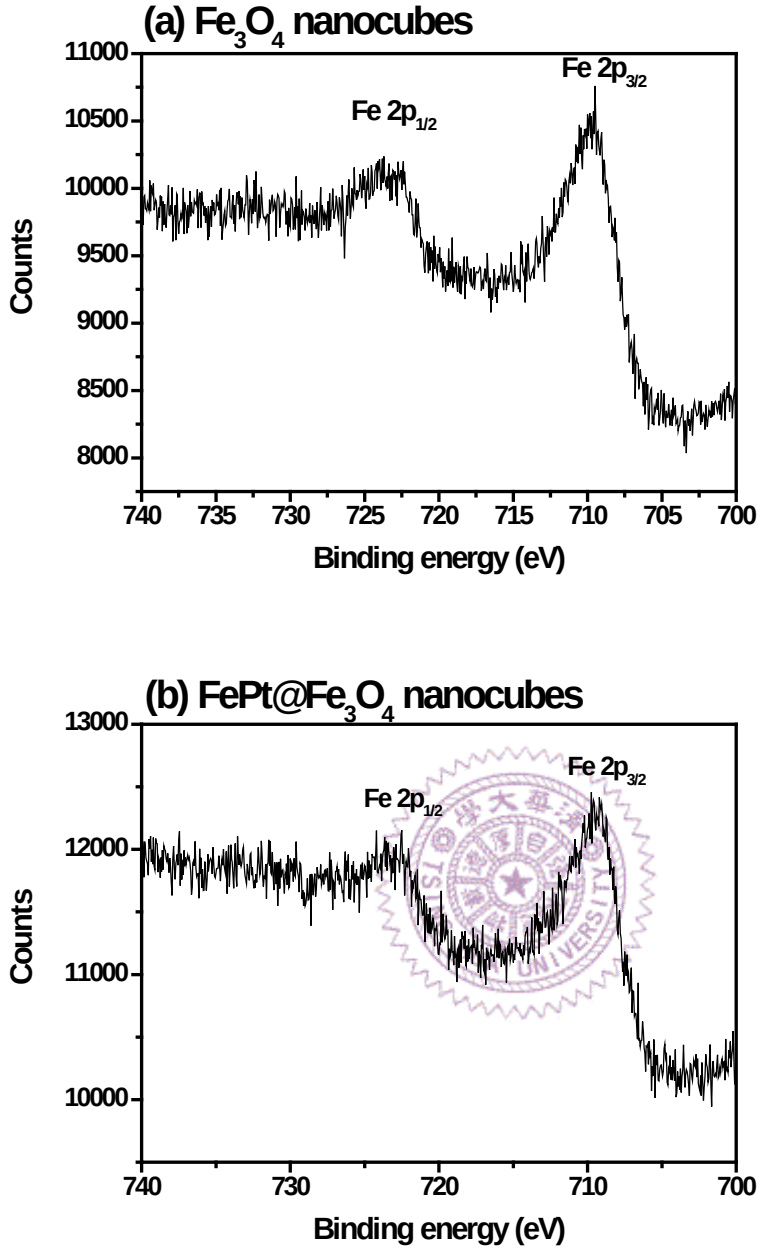

Fig. 6.3 X-ray photoelectron spectrum (XPS) of (a) Fe_3O_4 nanocubes and (b) FePt@Fe_3O_4 nanocubes

6.2.2 The MRI application of Fe_3O_4 and FePt@Fe_3O_4 nanocubes

Magnetic NPs provide many attractive possibilities in biomedicine applications, such as the MRI contrast enhancement, magnetic separation, drug delivery, and hyperthermia. For MRI application, the magnetic NPs can significantly shorten the transverse relaxation time (T_2) of protons due to the dipolar interaction between the magnetic NPs and the surrounding solvent. Superparamagnetic NPs have been extensively investigated and used as T_2 contrast agents. Even though there are many commercial available T_2 contrast agents, such as Resovist® and Feridex®, the development of highly sensitive agents to enhance local tissue contrast for noninvasively early diagnosis by MRI is still a crucial challenge.

One of the important properties, which affect the MRI contrast enhancement, is the saturation magnetization of magnetic NPs. Because the interaction between magnetic NPs and the surrounding solvent is through magnetic dipolar interaction, the larger saturation magnetization leads to stronger dipolar interaction. So, the transverse relaxation rate (R_2, which is equal to $1/T_2$) for the contrast agents can be significantly enhanced with higher saturation magnetization. The specific saturation magnetizations of bulk Fe_3O_4 and FePt are 471 emu/cc and 1140 emu/cc, respectively. Hence, it was reasonably presumed that FePt@Fe_3O_4 NPs should have better MRI contrast enhancement than Fe_3O_4 NPs due to the embedding of FePt core, which has higher magnetization. On the other hand, single phase Fe_3O_4 NPs have been largely found from magnetosome in magnetotactic bacteria in nature. Noteworthily, most of those naturally made NPs are cubic or cuboctahedral. However, there is

still no report to compare the shape effect in MRI contrast enhancement. So, in this section, the MRI contrast enhancement of Fe_3O_4 and FePt@Fe_3O_4 nanocubes are discussed.

16.1 nm Fe_3O_4 and 14.7 nm FePt@Fe_3O_4 nanocubes were used in the MRI measurements, and their syntheses and characterizations were presented in the previous chapters. The size of FePt core in FePt@Fe_3O_4 nanocubes is 4.1 nm. Both Fe_3O_4 and FePt@Fe_3O_4 nanocubes are superparamagnetic, whose hysteresis loops at room temperature are shown in Fig. 6.4. Before the MRI measurements, the hydrophobic NPs should be transferred to hydrophilic by being modified with CTAB (Cetyl trimethylammonium bromide). Only FePt@Fe_3O_4 nanocubes showed a high r_2 relaxivity of 360 $mM^{-1}s^{-1}$ at 4.7 T with Biospec spectrometer, while the r_2 relaxivities of Resovist® (commercial available MRI contrast agent) and Fe_3O_4 nanocube are 194 and 129 $mM^{-1}s^{-1}$, respectively, shown in Fig. 6.5. The relaxivity of FePt@Fe_3O_4 nanocube is about 2.7 and 2 times higher than those of Fe_3O_4 nanocube and Resovist®, respectively. In vitro T_2-weighted MR images taken with 4.7 T biospec spectrometer are shown in Fig. 6.5. FePt@Fe_3O_4 nanocubes showed the significantly darkened images than those of Fe_3O_4 nanocubes and Resovist® at the corresponding concentrations. It indicates that FePt@Fe_3O_4 nanocube is a better T_2 contrast agent than Fe_3O_4 only NPs. The r_2 relaxivity is strongly related to the magnetic moment and particle size.[5, 108] Because the sizes of Fe_3O_4 and FePt@Fe_3O_4 nanocubes are similar, the size effect in MRI enhancement can be excluded. However, the FePt@Fe_3O_4 nanocubes have larger saturation magnetization than Fe_3O_4 nanocubes due to the high magnetic moment FePt cores. The improvement of r_2 relaxivity by

embedding high magnetic moment core inside iron oxide shell has also been demonstrated, such as iron-iron oxide core/shell NPs.[114-117] Noteworthily, the simple FePt NPs with the size of 4.1 nm did not show effective r_2 enhancement, shown in Table 6.1. This result might arise from the low effective magnetic moment of small FePt NPs caused by the high percentage of magnetically dead surface layer. However, the coating of Fe_3O_4 shell on FePt core can effectively reduce the magnetically dead layer of FePt NPs due to the interfacial coupling between FePt and Fe_3O_4. Hence, the high MRI contrast enhancement of FePt@Fe_3O_4 nanocubes is mainly attributed to the embedded FePt core which increases the magnetization of core/shell NPs. Finally, we also compare the shape effects on MRI r_2 enhancement. The Fe_3O_4 nanocubes did not show significantly enhanced MRI r_2 relaxivity compared to the spherical NPs, shown in Table 6.1. The shape-independent r_2 relaxivity could be reasonably explained by the fact that the saturation magnetization of NPs was not affected by their shapes.[68]

Recently, a micro-engineered magnetic double-disk structure was fabricated by using a top-down approach and was demonstrated for its capability of high-sensitivity multiplex MRI.[124] The resolvable resonance frequency shift of water inside the structure could be tuned by adjusting the disk size and the distance between the double disks, which changed the magnitude of the generated homogeneous magnetic field. The bottom-up self-assembled nanocubes with well aligned crystalline orientations on Si substrates we present here can potentially achieve the similar functions. The frequency shift of water can be tuned by adjusting the nanocube size, materials of core/shell and interparticle

distance through the chemical approach. It was also reported that the magnetic flux configuration could be manipulated by the arrangement of magnetic nanocubes.[125] A homogeneous magnetic field generated between two neighboring magnetic nanocubes was clearly demonstrated by using electron holography. Therefore, our uniform magnetic nanocube superlattices on Si substrates may have a great opportunity for multispectral MRI. One of the remaining challenges is to form the large area self-assembled superlattice to produce high signal.

In this section, we have demonstrated that embedding the high-magnetic-moment FePt core inside the Fe_3O_4 shell can effectively enhance the MRI r_2 relaxivity which is about 2.7 and 2 times higher than those of Fe_3O_4 nanocube and Resovist®, respectively. In addition, adjusting the self-assembly of FePt@Fe_3O_4 nanocubes may have the opportunity to provide the extra frequency shift of water, which can let the FePt@Fe_3O_4 nanocubes become multispectral.

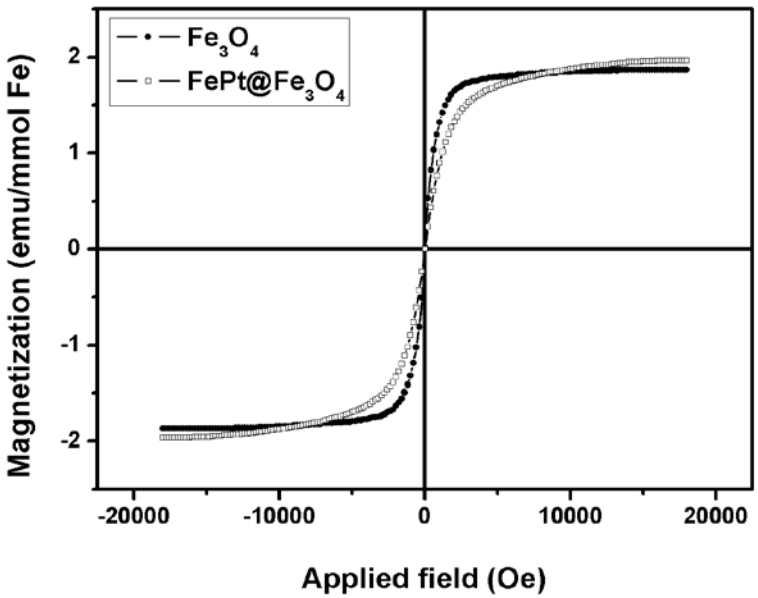

Fig. 6.4 M-H hysteresis loops of Fe_3O_4 and FePt@Fe_3O_4 nanocubes measured at room temperature.

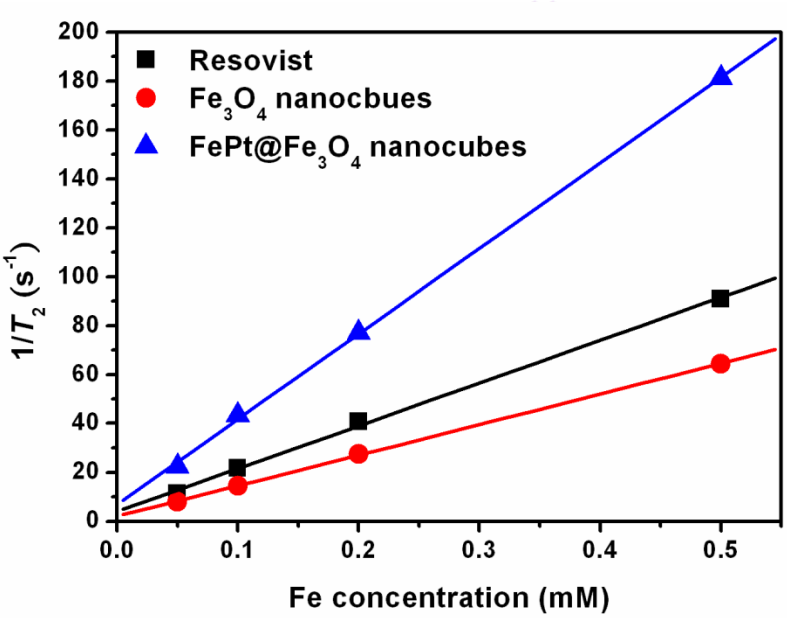

Fig. 6.5 The variation of $1/T_2$ with Fe concentration of Resovist®, Fe_3O_4 nanocubes and FePt@Fe_3O_4 nanocubes measured at 4.7 T. The r_2 relaxivities ($mM^{-1}s^{-1}$) were obtained from the fitting slope of each sample.

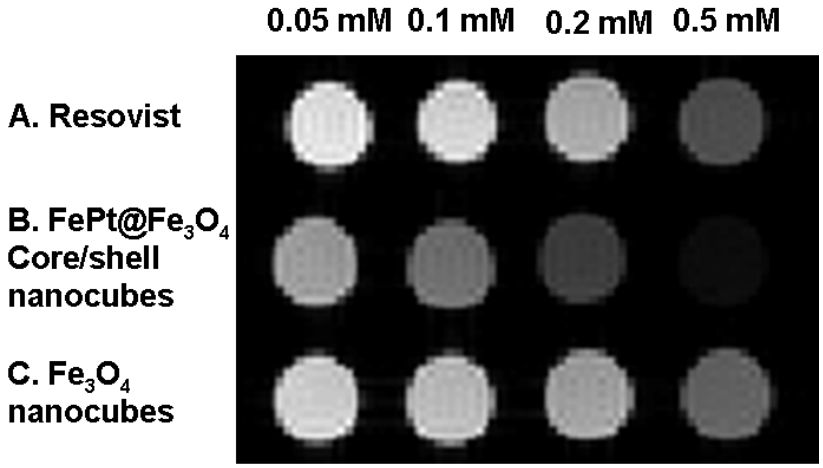

Fig. 6.5 T_2-weighted images of (a) Resovist®, (b) FePt@Fe_3O_4 core/shell nanocubes, and (c) Fe_3O_4 nanocubes with the same Fe concentration measured at 4.7T.

	FePt	Cubic Fe_3O_4	Spherical Fe_3O_4
Average size (nm)	**4.1 ± 0.3**	**16.1 ± 0.9**	**14.8 ± 1.2**
r_2 ($mM^{-1}s^{-1}$)	**2.8**	**100**	**82**

Table 6.1 The average sizes and r_2 relaxivities of FePt, cubic Fe_3O_4, and spherical Fe_3O_4 nanoparticles. The relixities are measured by 0.47 T biospec MR instrument.

6.3 Summary

In this chapter, we demonstrate that the cation site occupancies of Fe_3O_4 nanocrystals were strongly related to their shape rather than the core/shell structure. For the cubic Fe_3O_4 NPs, more ferric ions, Fe^{3+}, occupied the octahedral sites. However, for the rhombicuboctahedral Fe_3O_4 NPs, the cation site occupancies are closer to the bulk Fe_3O_4. The cation site occupancies may be affected by the surface-to-volume ratio of NPs or by their terminated planes. The cation site occupancies detected by XMCD can be helpful to realize the catalytic ability of Fe_3O_4 NPs.

We also demonstrate that superparamagnetic FePt@Fe_3O_4 nanocubes show a high r_2 relaxivity and significantly enhanced MRI contrast, which is attributable to the high magnetization of the FePt core. In addition, the self-assembly of FePt@Fe_3O_4 nanocubes may become the potential multispectral MRI agent.

Chapter VII

Conclusions

In this dissertation, we have presented the study about the formation mechanism and unique features of shaped Fe_3O_4 and FePt@Fe_3O_4 NPs. Several important results are summarized here.

1. A modified hot-injecting method has been successfully developed to synthesize the shaped Fe_3O_4 NPs, in which the precursor was injected into the hot reaction solution at a controlled slow injecting rate. The shape of Fe_3O_4 NPs can be changed from cubic to rhombicuboctahedral when increasing the monomer concentration in solution. The shape formation mechanism is related to the surface energy and the relative growth rate of each plane. In addition, by changing the monomer concentration, it can be concluded that the formation of shaped Fe_3O_4 NPs is mainly attributed to the modified hot-injecting method instead of the surfactant effect.

2. The cubic Fe_3O_4 NPs were terminated at {100} planes and are self-assembled into square packing superlattice on TEM grids. The (100) texture-like assembly on a Si substrate was also observed in XRD pattern. On the other hand, the rhombicuboctahedral Fe_3O_4 NPs were mainly terminated at {110} and {100} planes and self-assembled into quasi-hexagonal superlattice with [110] zone-axis on TEM grids.

The rhombicuboctahedral NP array on a Si substrate also showed textured structure with {110} and {100} planes preferentially parallel to the substrate.

3. The modified hot-injecting method can be further employed to synthesize the shaped FePt@Fe_3O_4 core/shell NPs. The final shape of FePt@Fe_3O_4 NPs was dominated by the growth condition of Fe_3O_4 shell but not the shape of FePt core. In addition, the epitaxial relationship between spherical core and shaped shell is not necessary. The loose requirements for shape and lattice constant of core materials make the modified hot-injecting method be reasonably suitable for the synthesis of core/Fe_3O_4 shell nanocubes with various and desired core materials.

4. The shape-dependent cation site occupancies of Fe_3O_4 nanocrystals were observed. More ferric ions, Fe^{3+}, occupy the octahedral sites when the shape of Fe_3O_4 and FePt@Fe_3O_4 NPs becomes cubic, which results in particular XMCD spectrum. However, the XMCD spectra of rhombicuboctahedral NPs are closer to the bulk Fe_3O_4. The maximum $Fe^{3+}{}_{Oh}$ peak in the XMCD spectra of cubic NPs may be due to their higher surface-to-volume ratio comparing to rhombicuboctahedral NPs or due to the terminated {100} planes of cubic NPs.

5. The r_2 relaxivity of FePt@Fe_3O_4 nanocubes is 2.7 and 2 times higher than those of Fe_3O_4 nanocube and Resovist®, respectively. The large r_2 relaxivity is attributable to the high magnetization of the FePt core.

$FePt@Fe_3O_4$ nanocubes are demonstrated as potential MRI contrast agents.

Suggestion for future works

1. Investigating the shape-dependent properties of NPs has been an important issue. However, for many materials, the shape control is still a challenge. The modified hot-injection method should be able to control the shape of other spinel oxide NPs, such as Mn_3O_4, $ZnFe_2O_4$, $CoFe_2O_4$…*etc.*, Their shape-dependent properties can be investigated. In addition, various core-shell structured and shaped NPs can be reasonably synthesized by this method, and show multifunctional properties.

2. The shape-induced NP assembly reveals preferential crystallographic orientation, which could show anisotropic properties. These NP assemblies should have potential applications in many fields, such as high density recording media, biomineralization, or tissue engineering. In addition, the configuration of magnetic flux between these NP superlattices can be investigated by the TEM holography.

3. In this study, we have found that the cation site occupancies of Fe_3O_4 NPs are determined by the shape and the terminated planes. The shaped Fe_3O_4 NPs can be further used as the catalyst for the high-temperature water gas shift reaction. The shape-dependent catalyst ability of Fe_3O_4 NPs can be investigated.

Chapter VIII

References

[1] A. H. Lu, E. L. Salabas, F. Schuth, Angew. Chem. Int. Edit. 2007, 46, 1222.

[2] R. H. Kodama, J. Magn. Magn. Mater. 1999, 200, 359.

[3] R. H. Kodama, S. A. Makhlouf, A. E. Berkowitz, Phys. Rev. Lett. 1997, 79, 1393.

[4] X. Batlle, A. Labarta, J. Phys. D-Appl. Phys. 2002, 35, R15.

[5] Y. W. Jun, Y. M. Huh, J. S. Choi, J. H. Lee, H. T. Song, S. Kim, S. Yoon, K. S. Kim, J. S. Shin, J. S. Suh, J. Cheon, J. Am. Chem. Soc. 2005, 127, 5732.

[6] W. S. Seo, H. H. Jo, K. Lee, B. Kim, S. J. Oh, J. T. Park, Angew. Chem. Int. Edit. 2004, 43, 1115.

[7] M. Chen, J. P. Liu, S. H. Sun, J. Am. Chem. Soc. 2004, 126, 8394.

[8] Q. Chen, Z. J. Zhang, Appl. Phys. Lett. 1998, 73, 3156.

[9] R. E. Dunin-Borkowski, M. R. McCartney, R. B. Frankel, D. A. Bazylinski, M. Posfai, P. R. Buseck, Science 1998, 282, 1868.

[10] S. Mann, R. B. Frankel, R. P. Blakemore, Nature 1984, 310, 405.

[11] C. Y. Hsu, C. W. Li, Science 1994, 265, 95.

[12] A. K. Gupta, M. Gupta, Biomaterials 2005, 26, 3995.

[13] C. Corot, P. Robert, J. M. Idee, M. Port, Adv. Drug Deliv. Rev. 2006, 58, 1471.

[14] A. Bjornerud, L. Johansson, NMR Biomed. 2004, 17, 465.

[15] M. V. Kovalenko, M. I. Bodnarchuk, R. T. Lechner, G. Hesser, F. Schaffler, W. Heiss, J. Am. Chem. Soc. 2007, 129, 6352.

[16] H. T. Yang, T. Ogawa, D. Hasegawa, M. Takahashi, J. Appl. phys. 2008, 103, 07D526.

[17] D. Kim, N. Lee, M. Park, B. H. Kim, K. An, T. Hyeon, J. Am. Chem. Soc. 2009, 131, 454.

[18] S. H. Sun, C. B. Murray, D. Weller, L. Folks, A. Moser, Science 2000, 287, 1989.

[19] S. Maenosono, S. Saita, IEEE Trans. Magn. 2006, 42, 1638.

[20] S. Maenosono, T. Suzuki, S. Saita, J. Magn. Magn. Mater. 2008, 320, L79.

[21] D. K. Kim, D. Kan, T. Veres, F. Normadin, J. K. Liao, H. H. Kim, S. H. Lee, M. Zahn, M. Muhammed, J. Appl. Phys. 2005, 97, 3.

[22] H. Zeng, S. H. Sun, J. Li, Z. L. Wang, J. P. Liu, Appl. Phys. Lett. 2004, 85, 792.

[23] V. Nandwana, G. S. Chaubey, K. Yano, C. B. Rong, J. P. Liu, J. Appl. Phys. 2009, 105, 5.
[24] C. W. Lai, Y. H. Wang, B. P. Uttam, Y. C. Chen, J. K. Hsiao, C. L. Liu, H. M. Liu, C. Y. Chen, P. T. Chou, Chem. Commun. 2008, 5342.
[25] A. Figuerola, A. Fiore, R. Di Corato, A. Falqui, C. Giannini, E. Micotti, A. Lascialfari, M. Corti, R. Cingolani, T. Pellegrino, P. D. Cozzoli, L. Manna, J. Am. Chem. Soc. 2008, 130, 1477.
[26] E. Baeuerlein, *Biomineralization: from bilogy to biotechnology and medical application*, Wiley-VCH, Cambridge 2000.
[27] T. Z. Yang, C. M. Shen, Z. Li, H. R. Zhang, C. W. Xiao, S. T. Chen, Z. C. Xu, D. X. Shi, J. Q. Li, H. J. Gao, J. Phys. Chem. B 2005, 109, 23233.
[28] A. Ahniyaz, Y. Sakamoto, L. Bergstrom, Proc. Natl. Acad. Sci. U. S. A. 2007, 104, 17570.
[29] S. F. Xie, X. Zhou, X. G. Han, Q. Kuang, M. S. Jin, Y. Q. Jiang, Z. X. Xie, L. S. Zheng, J. Phys. Chem. C 2009, 113, 19107.
[30] H. Zeng, J. Li, Z. L. Wang, J. P. Liu, S. H. Sun, Nano Lett. 2004, 4, 187.
[31] K. Ohe, Y. Tagai, S. Nakamura, T. Oshima, Y. Baba, J. Chem. Eng. Jpn. 2005, 38, 671.
[32] H. Katsumata, S. Kaneco, K. Inomata, K. Itoh, K. Funasaka, K. Masuyama, T. Suzuki, K. Ohta, J. Environ. Manage. 2003, 69, 187.
[33] T. Kendelewicz, P. Liu, C. S. Doyle, G. E. Brown, E. J. Nelson, S. A. Chambers, Surf. Sci. 2000, 453, 32.
[34] B. D. Terris, T. Thomson, J. Phys. D-Appl. Phys. 2005, 38, R199.
[35] S. Mornet, S. Vasseur, F. Grasset, E. Duguet, J. Mater. Chem. 2004, 14, 2161.
[36] A. Ito, M. Shinkai, H. Honda, T. Kobayashi, J. Biosci. Bioeng. 2005, 100, 1.
[37] S. H. Sun, Adv. Mater. 2006, 18, 393.
[38] D. L. Huber, Small 2005, 1, 482.
[39] U. Jeong, X. W. Teng, Y. Wang, H. Yang, Y. N. Xia, Adv. Mater. 2007, 19, 33.
[40] R. F. C. Farrow, D. Weller, R. F. Marks, M. F. Toney, A. Cebollada, G. R. Harp, J. Appl. Phys. 1996, 79, 5967.
[41] B. D. Cullity, *Introduction to Magnetic Materials*, Addison-Wesley, London 1972.
[42] G. C. Hadjipanayis, J. Magn. Magn. Mater. 1999, 200, 373.
[43] Y. Labaye, O. Crisan, L. Berger, J. M. Greneche, J. M. D. Coey, J. Appl. Phys. 2002, 91, 8715.
[44] H. Yang, D. Hasegawa, M. Takahashi, T. Ogawa, IEEE Trans. Magn. 2008, 44, 3895.
[45] M. Iizumi, T. F. Koetzle, G. Shirane, S. Chikazumi, M. Matsui, S. Todo, Acta

Crystallogr. Sect. B-Struct. Commun. 1982, 38, 2121.
[46] G. F. Goya, T. S. Berquo, F. C. Fonseca, M. P. Morales, J. Appl. Phys. 2003, 94, 3520.
[47] L. Bickford, Jr., J. Brownlow, F. R. Penoyer, Proc. IEEE 1957, 104, 238.
[48] C. Medrano, M. Schlenker, J. Baruchel, J. Espeso, Y. Miyamoto, Phys. Rev. B 1999, 59, 1185.
[49] C. I. Pearce, C. M. B. Henderson, R. A. D. Pattrick, G. Van der Laan, D. J. Vaughan, Am. Miner. 2006, 91, 880.
[50] Y. S. Kang, S. Risbud, J. F. Rabolt, P. Stroeve, Chem. Mat. 1996, 8, 2209.
[51] S. H. Sun, H. Zeng, J. Am. Chem. Soc. 2002, 124, 8204.
[52] S. H. Sun, H. Zeng, D. B. Robinson, S. Raoux, P. M. Rice, S. X. Wang, G. X. Li, Journal of the American Chemical Society 2004, 126, 273.
[53] S. H. Sun, E. E. Fullerton, D. Weller, C. B. Murray, IEEE Trans. Magn. 2001, 37, 1239.
[54] K. E. Elkins, T. S. Vedantam, J. P. Liu, H. Zeng, S. H. Sun, Y. Ding, Z. L. Wang, Nano Lett. 2003, 3, 1647.
[55] P. Gibot, E. Tronc, C. Chaneac, J. P. Jolivet, D. Fiorani, A. M. Testa, J. Magn. Magn. Mater. 2005, 290, 555.
[56] X. C. Sun, S. S. Kang, J. W. Harrell, D. E. Nikles, Z. R. Dai, J. Li, Z. L. Wang, J. Appl. Phys. 2003, 93, 7337.
[57] S. S. Kang, Z. Y. Jia, D. E. Nikles, J. W. Harrell, IEEE Trans. Magn. 2003, 39, 2753.
[58] F. Iskandar, H. M. Lee, T. Toda, T. Iwaki, K. Okuyama, J. Magn. Magn. Mater. 2006, 305, 514.
[59] M. Chen, D. E. Nikles, Nano Lett. 2002, 2, 211.
[60] S. S. Kang, Z. Y. Jia, D. E. Nikles, J. W. Harrell, J. Appl. Phys. 2004, 95, 6744.
[61] C. H. Lai, C. H. Ho, J. Appl. Phys. 2005, 97.
[62] Q. Y. Yan, T. Kim, A. Purkayastha, P. G. Ganesan, M. Shima, G. Ramanath, Adv. Mater. 2005, 17, 2233.
[63] K. Elkins, D. Li, N. Poudyal, V. Nandwana, Z. Q. Jin, K. H. Chen, J. P. Liu, J. Phys. D-Appl. Phys. 2005, 38, 2306.
[64] D. R. Li, N. Poudyal, V. Nandwana, Z. Q. Jin, K. Elkins, J. P. Liu, J. Appl. Phys. 2006, 99.
[65] H. Zeng, J. Li, J. P. Liu, Z. L. Wang, S. H. Sun, Nature 2002, 420, 395.
[66] N. Tian, Z. Y. Zhou, S. G. Sun, Y. Ding, Z. L. Wang, Science 2007, 316, 732.
[67] X. G. Peng, L. Manna, W. D. Yang, J. Wickham, E. Scher, A. Kadavanich, A. P. Alivisatos, Nature 2000, 404, 59.
[68] G. Salazar-Alvarez, J. Qin, V. Sepelak, I. Bergmann, M. Vasilakaki, K. N.

Trohidou, J. D. Ardisson, W. A. A. Macedo, M. Mikhaylova, M. Muhammed, M. D. Baro, J. Nogues, J. Am. Chem. Soc. 2008, 130, 13234.
[69] A. R. Tao, S. Habas, P. D. Yang, Small 2008, 4, 310.
[70] Y. J. Xiong, Y. N. Xia, Adv. Mater. 2007, 19, 3385.
[71] S. M. Lee, S. N. Cho, J. Cheon, Adv. Mater. 2003, 15, 441.
[72] Y. W. Jun, J. S. Choi, J. Cheon, Angew. Chem. Int. Edit. 2006, 45, 3414.
[73] H. Zeng, P. M. Rice, S. X. Wang, S. H. Sun, J. Am. Chem. Soc. 2004, 126, 11458.
[74] Q. Song, Y. Ding, Z. L. Wang, Z. J. Zhang, J. Phys. Chem. B 2006, 110, 25547.
[75] S. Yamamuro, K. Sumiyama, Chem. Phys. Lett. 2006, 418, 166.
[76] C. Martos, J. Dufour, A. Ruiz, Int. J. Hydrog. Energy 2009, 34, 4475.
[77] N. Mulakaluri, R. Pentcheva, M. Wieland, W. Moritz, M. Scheffler, Phys. Rev. Lett. 2009, 103.
[78] R. Pentcheva, F. Wendler, H. L. Meyerheim, W. Moritz, N. Jedrecy, M. Scheffler, Phys. Rev. Lett. 2005, 94.
[79] Q. A. Pankhurst, J. Connolly, S. K. Jones, J. Dobson, J. Phys. D-Appl. Phys. 2003, 36, R167.
[80] Y. W. Jun, J. H. Lee, J. Cheon, Angew. Chem. Int. Edit. 2008, 47, 5122.
[81] J. T. Jang, H. Nah, J. H. Lee, S. H. Moon, M. G. Kim, J. Cheon, Angew. Chem. Int. Edit. 2009, 48, 1234.
[82] S. Foner, Rev. Sci. Instrum. 1956, 27, 548.
[83] C. Nordling, E. Sokolowski, K. Siegbahn, Physical Review 1957, 105, 1676.
[84] E. Sokolowski, C. Nordling, K. Siegbahn, Arkiv for Fysik 1957, 12, 301.
[85] J. L. Erskine, E. A. Stern, Phys. Rev. B 1975, 12, 5016.
[86] G. Schutz, W. Wagner, W. Wilhelm, P. Kienle, R. Zeller, R. Frahm, G. Materlik, Phys. Rev. Lett. 1987, 58, 737.
[87] J. Stohr, J. Magn. Magn. Mater. 1999, 200, 470.
[88] J. Stohr, Y. Wu, B. D. Hermsmeier, M. G. Samant, G. R. Harp, S. Koranda, D. Dunham, B. P. Tonner, Science 1993, 259, 658.
[89] L. H. Tjeng, Y. U. Idzerda, P. Rudolf, F. Sette, C. T. Chen, J. Magn. Magn. Mater. 1992, 109, 288.
[90] J. Stohr, *Research with Third-Generation Soft X-ray Synchrotron Radiation Source*, Kluwer Academic Publishers, Netherlands 1994.
[91] J. Stohr, J. Electron Spectrosc. Relat. Phenom. 1995, 75, 253.
[92] B. T. Thole, P. Carra, F. Sette, G. Vanderlaan, Phys. Rev. Lett. 1992, 68, 1943.
[93] P. Carra, B. T. Thole, M. Altarelli, X. D. Wang, Phys. Rev. Lett. 1993, 70, 694.
[94] S. H. Sun, S. Anders, T. Thomson, J. E. E. Baglin, M. F. Toney, H. F. Hamann, C. B. Murray, B. D. Terris, J. Phys. Chem. B 2003, 107, 5419.

[95] R. K. Zheng, H. W. Gu, B. Xu, K. K. Fung, X. X. Zhang, S. P. Ringer, Adv. Mater. 2006, 18, 2418.
[96] C. B. Murray, D. J. Norris, M. G. Bawendi, J. Am. Chem. Soc. 1993, 115, 8706.
[97] P. D. Cozzoli, L. Manna, M. L. Curri, S. Kudera, C. Giannini, M. Striccoli, A. Agostiano, Chem. Mat. 2005, 17, 1296.
[98] V. K. Lamer, R. H. Dinegar, J. Am. Chem. Soc. 1950, 72, 4847.
[99] Y. Xia, Y. J. Xiong, B. Lim, S. E. Skrabalak, Angew. Chem. Int. Edit. 2009, 48, 60.
[100] C. D. Donega, P. Liljeroth, D. Vanmaekelbergh, Small 2005, 1, 1152.
[101] O. Song, Z. J. Zhang, J. Am. Chem. Soc. 2004, 126, 6164.
[102] C. M. Fang, S. C. Parker, G. de With, J. Am. Ceram. Soc. 2000, 83, 2082.
[103] A. Shavel, L. M. Liz-Marzan, Phys. Chem. Chem. Phys. 2009, 11, 3762.
[104] O. Iglesias, X. Batlle, A. Labarta, Phys. Rev. B 2005, 72, 4.
[105] D. W. Kavich, J. H. Dickerson, S. V. Mahajan, S. A. Hasan, J. H. Park, Phys. Rev. B 2008, 78, 6.
[106] K. E. Kim, M. K. Lee, Y. M. Sung, T. G. Kim, Appl. Phys. Lett. 2007, 90, 173117.
[107] F. R. Fan, D. Y. Liu, Y. F. Wu, S. Duan, Z. X. Xie, Z. Y. Jiang, Z. Q. Tian, J. Am. Chem. Soc. 2008, 130, 6949.
[108] S. E. Habas, H. Lee, V. Radmilovic, G. A. Somorjai, P. Yang, Nat. Mater. 2007, 6, 692.
[109] R. A. Crowther, D. J. Derosier, A. Klug, Proceedings of the Royal Society of London Series a-Mathematical and Physical Sciences 1970, 317, 319.
[110] P. F. C. Gilbert, Proc. R. Soc. Lond. Ser. B-Biol. Sci. 1972, 182, 89.
[111] J. S. Tsai, J. J. Kai, L. Chang, F. R. Chen, J. Electron Microsc. 2004, 53, 371.
[112] N. Kawase, M. Kato, H. Nishioka, H. Jinnai, Ultramicroscopy 2007, 107, 8.
[113] Y. G. Sun, Y. N. Xia, Science 2002, 298, 2176.
[114] O. Bomati-Miguel, M. P. Morales, P. Tartaj, J. Ruiz-Cabello, P. Bonville, M. Santos, X. Q. Zhao, S. Veintemillas-Verdaguer, Biomaterials 2005, 26, 5695.
[115] H. Khurshid, S. Balakrishnan, L. Colak, M. J. Bonder, G. C. Hadjipanayis, IEEE Trans. Magn. 2009, 45, 4877.
[116] O. B. Miguel, Y. Gossuin, M. P. Morales, P. Gillis, R. N. Muller, S. Veintemillas-Verdaguer, Magn. Reson. Imaging 2007, 25, 1437.
[117] Y. Qiang, J. Antony, A. Sharma, J. Nutting, D. Sikes, D. Meyer, J. Nanopart. Res. 2006, 8, 489.
[118] H. W. Gu, P. L. Ho, K. W. T. Tsang, L. Wang, B. Xu, J. Am. Chem. Soc. 2003, 125, 15702.
[119] R. A. D. Pattrick, G. Van der Laan, C. M. B. Henderson, P. Kuiper, E. Dudzik, D.

J. Vaughan, Eur. J. Mineral. 2002, 14, 1095.
[120] P. Morrall, F. Schedin, G. S. Case, M. F. Thomas, E. Dudzik, G. van der Laan, G. Thornton, Phys. Rev. B 2003, 67.
[121] J. Park, K. J. An, Y. S. Hwang, J. G. Park, H. J. Noh, J. Y. Kim, J. H. Park, N. M. Hwang, T. Hyeon, Nat. Mater. 2004, 3, 891.
[122] N. Perez, F. Bartolome, L. M. Garcia, J. Bartolome, M. P. Morales, C. J. Serna, A. Labarta, X. Batlle, Appl. Phys. Lett. 2009, 94, 093108.
[123] S. A. Chambers, S. A. Joyce, Surf. Sci. 1999, 420, 111.
[124] G. Zabow, S. Dodd, J. Moreland, A. Koretsky, Nature 2008, 453, 1058.
[125] E. Snoeck, C. Gatel, L. M. Lacroix, T. Blon, S. Lachaize, J. Carrey, M. Respaud, B. Chaudret, Nano Lett. 2008, 8, 4293.